NAT'L INST. OF STAND & TECH R.I.C.
A11104 256873

NATIONAL INSTITUTE OF STANDARDS &
TECHNOLOGY
Research Information Center
Gaithersburg, MD 20899

IR 3974

UNAVAILABLE FOR BINDING

NISTIR 3975

MAGNETIC MEASUREMENTS FOR HIGH ENERGY PHYSICS APPLICATIONS

Final Report

R. B. Goldfarb, Editor

United States Department of Commerce
National Institute of Standards and Technology

NISTIR 3975

MAGNETIC MEASUREMENTS FOR HIGH ENERGY PHYSICS APPLICATIONS

Final Report

R. B. Goldfarb, Editor

Electromagnetic Technology Division
Electronics and Electrical Engineering Laboratory
National Institute of Standards and Technology
Boulder, Colorado 80303

August 1991

Prepared for:
U.S. Department of Energy
Division of High Energy Physics
Washington, DC 20545

U.S. DEPARTMENT OF COMMERCE, Robert A. Mosbacher, Secretary
NATIONAL INSTITUTE OF STANDARDS AND TECHNOLOGY, John W. Lyons, Director

Magnetic Measurements for High Energy Physics Applications

Final Report

R. B. Goldfarb, Editor

Electromagnetic Technology Division
Electronics and Electrical Engineering Laboratory
National Institute of Standards and Technology
Boulder, Colorado 80303

Abstract

This report is a collection of papers describing magnetic measurements on multifilamentary Nb-Ti superconductor wires and cables as a function of magnetic field and time at liquid-helium temperatures. The papers deal with ac losses and interfilament coupling by proximity effect and eddy currents. Flux creep was investigated under different experimental conditions. A Hall-probe magnetometer, which was used to measure magnetization and flux creep in the presence of a transport current, is described. A method for increasing the critical current of superconducting cable by controlling twist pitch is demonstrated. A critical-state model for the magnetization of superconductors was developed for samples with field-dependent critical current density and rectangular cross section.

Key words: ac losses; critical current; critical state; eddy currents; flux creep; Hall sensors; hysteresis; magnetization; magnetometry; multipole fields; niobium-titanium; proximity effect; Superconducting Super Collider; superconductors.

Magnetic Measurements for High Energy Physics Applications

Final Report

Executive Summary

This report includes work done for the U. S. Department of Energy, Division of High Energy Physics, during the period 15 June 1988 – 14 June 1991, under interagency agreement No. DE-AI05-85ER40240. The topics investigated are summarized below.

• "Magnetic Characteristics and Measurements of Filamentary Nb-Ti Wire for the Superconducting Super Collider" – This paper discusses time-independent and time-dependent ac losses that may be detected with magnetic instrumentation. Different forms of magnetometry are reviewed. AC susceptibility measurements demonstrate coupling in prototype SSC wires and cables containing Mn.

• "Hall Probe Magnetometer for SSC Magnet Cables: Effect of Transport Current on Magnetization and Flux Creep" – This simple magnetometer can be used to measure hysteresis loops and flux creep in superconductor wires and cables carrying transport current. The presence of a transport current, on the order of 20% of the critical current, did not greatly affect the magnetization or rate of flux creep.

• "Transport Current Effects on Flux Creep and Magnetization in Nb-Ti Multifilamentary Cable Strands" – Flux creep measurements were made on an SSC cable strand carrying a transport current equal to about 70% of the critical current. There was a factor of four increase in the magnetization decay over a sample with no transport current, and substantial decreases in the magnetization and full-penetration field.

• "Enhanced Flux Creep in Nb-Ti Superconductors after an Increase in Temperature" – An inadvertent increase in temperature in the operation of SSC magnets could increase their rate of field decay. Measurements were made on short cable samples. Magnetic relaxation measurements at 3.5 and 4.0 K, after field cycling, showed a decay of 2.8% in 50 min. Relaxation measured after the critical state was established at 3.5 K, followed by a temperature increase to 4.0 K, was 4.8% in 50 min. A 0.1-K rise in temperature caused a magnetization decay of 3.2% in 50 min.

• "Investigation of Possible Causes for the Multipole Drift in Superconducting Dipole Magnets" – Two experiments are described which address the problem of multipole-field decay in dipole magnets: exposure of the cable to field gradients, and the presence of solder joints. A sample cable's magnetization decay was not affected by either condition.

• "Effect of Mechanical Deformation on Nb-Ti Filament Proximity-Effect Coupling at the Edges of SSC Cables" – Proximity-effect coupling in multifilament wires may be induced by cabling. The rate of flux creep at low field is the same for coupled and uncoupled filaments, which suggests that the proximity coupled matrix is not a significant source of flux creep.

• "AC Loss Measurements of Two Multifilamentary NbTi Composite Strands" – This paper discusses magnetic hysteresis losses in two very different multifilamentary Nb-Ti wires. One wire, a prototype SSC conductor, exhibited interfilament coupling and high losses. The other, containing widely spaced filaments in a resistive Cu-Ni matrix, had no coupling and lower losses. However, both wires have similar figures of merit when the critical current density of the wires were included in the analysis.

• "Effect of Cable and Strand Twist-Pitch Coincidence on the Critical Current of Flat, Coreless Superconductor Cables" – The current-carrying capacity of a Rutherford-type cable may be increased by about 10% simply by matching the cable twist pitch to the strand twist pitch. Current transfer among filaments is minimized and the voltage-current characteristic is improved.

• "Kim Model for Magnetization of Type-II Superconductors" – This paper develops magnetization equations for hard superconductors using the Kim model for critical current density as a function of internal magnetic field. The equations are for an infinite sample with rectangular cross section in longitudinal field. In certain limits, the equations are exact for cylinders and slabs. In other limits, the equations reduce to those of the well known Bean model.

CONTENTS

MAGNETIC CHARACTERISTICS AND MEASUREMENTS OF FILAMENTARY Nb-Ti WIRE FOR THE SUPERCONDUCTING SUPER COLLIDER

R. B. Goldfarb and R. L. Spomer

Electromagnetic Technology Division
National Institute of Standards and Technology
Boulder, Colorado 80303

ABSTRACT

In synchrotron accelerator applications, such as the Superconducting Super Collider (SSC), superconducting magnets are cycled in magnetic field. Desirable properties of the magnets include field uniformity, field stability with time, small residual field, and fairly small energy losses upon cycling. This paper discusses potential sources of problems in achieving these goals, describes important magnetic characteristics to be considered, and reviews measurement techniques for magnetic evaluation of candidate SSC wires. Instrumentation that might be practical for use in a wire-fabrication environment is described. We report on magnetic measurements of prototype SSC wires and cables and speculate on causes for instability in multipole fields of dipole magnets constructed with such cables.

INTRODUCTION

A typical field cycle for the proposed Superconducting Super Collider (SSC) consists of an initial charge to a full field of 6.6 T, reduction of field to 50 mT, increase to 0.33 T for proton injection, and a slow increase of field to 6.6 T as the proton beam is accelerated.[1] The multifilamentary Nb-Ti cables used in the construction of the superconducting dipole magnets are themselves exposed to the field of adjacent windings, usually approximated as a transverse field. Electromagnetic characteristics of the wires and cables are potential sources of difficulty in meeting magnet specifications. Thus, requirements for the magnet imply design and performance specifications for the wires and cables. In this paper we discuss magnetic parameters useful for evaluating multifilar Nb-Ti superconductor wire and cable for the SSC.

MAGNETIC CHARACTERISTICS

Superconductors under steady-state conditions are lossless except for losses associated with thermally activated flux creep. With transient or ac currents and fields, there are several sources of energy dissipation. These ac losses may be classified according to their mechanism and localization within a wire composed of fine superconducting filaments in a normal-metal matrix.

Advances in Cryogenic Engineering (Materials), Vol. 36
Edited by R. P. Reed and F. R. Fickett
Plenum Press, New York, 1990

In this section we describe ac loss effects that may be detected with magnetic instrumentation. We discuss both time-independent and time-dependent phenomena for the wire and cable, not the dipole magnets made with these elements. Ideally, all of these ac losses should be minimized, subject to the often conflicting requirements of high critical current and stability against propagation of a normal zone (quench).

Time-Independent Effects

Hysteresis. Magnetic hysteresis upon field cycling is a major loss mechanism. Hysteresis loss per field cycle is frequency independent. It arises in type-II superconductors from irreversibility of the penetration of flux vortices and shielding currents resulting from flux pinning in the filament volume and at the filament surface. The energy dissipation *per se* might be viewed as a trivial problem in applications where field is only occasionally cycled. However, large hysteresis leads to large remanent magnetization from trapped flux in the filaments as the applied field is reduced to zero. This remanent magnetization is the source of residual field in a superconducting magnet. Even at low fields, such as the 0.33-T SSC injection field, trapped flux acts as an offset to the field expected from the magnet current. When it is predictable, the residual field may be compensated. Field uniformity is usually achieved by strategic magnet design. However, remanent magnetization due to trapped flux in the superconductor wires makes it difficult to obtain uniform fields at low currents.

Because the ability of a superconductor to pin flux is an essential requirement for high critical current, both small remanent magnetization and small hysteresis may be achieved, not by reducing flux pinning, but by reducing filament diameter, as predicted by the critical state model.[2] Hysteresis loss is generally higher for wire carrying transport current than for an open-circuited sample, with the extra energy provided by the current source, not the field.[3] Hysteresis loss is determined as the enclosed area in a plot of magnetization vs. field. Measurements often are made with field cycled from positive to negative values. The SSC cycle is such that fields are always positive. In typical multifilamentary wires measured in transverse field, positive-field hysteresis loops, with maximum applied fields of 1 T, have about 45% of the loss associated with complete hysteresis loops.

Self-field of transport current. When transport current changes, moving self-field lines dissipate energy.[4] The use of small-diameter wires reduces these virtually hysteretic losses. In fine-filament wires, the self-field loss may be greater than the magnetic hysteresis loss. In accelerator applications, cabling with fully transposed strands reduces self-field loss; simple twisted strands would still have a large self-field. Three methods of transposition are twisted rope, woven braid, and flattened twisted cable. The last is planned for the SSC, but it results in mechanical damage to the cable corners with a local reduction in critical current.[5]

Coupling between filaments. There are two time-independent sources of filament coupling. One is simply interfilament contact arising from metallurgical problems in processing. Coupled filaments act as a single filament of large diameter, with its associated problems. The second is interfilamentary coupling by the proximity effect when filament spacing is on the order of the coherence length. This type of coupling is important for wires with closely spaced fine filaments. The addition of impurities, such as Ni or Mn, to the matrix material is often effective in reducing the coupling.[6] In any event, proximity-effect coupling is disrupted when magnetic fields approach the effective critical field of the coupling medium. The losses associated with time-independent filament coupling are hysteretic.

Time-Dependent Effects

Coupling between filaments. An important coupling arises from eddy currents driven by voltages induced by a changing applied field. Coupling loss is caused by the transfer of current between filaments and dissipation within the matrix. This relaxation phenomenon leads to time-varying magnetization and field instability of the magnet. It may be reduced by transposing the filaments, approximated by twisting the wire, during manufacture.[7] This decreases the longitudinal distance over which the transverse coupling currents can flow. Other ways to reduce coupling are by increasing the resistivity of the Cu matrix and by increasing the distance between filaments. The former strategy is consistent with other wire requirements provided the stability of the conductor is not impaired.

Flux creep. Flux creep consists of thermally activated jumps of bundles of flux vortices between pinning sites at constant field. Flux creep causes slow changes in magnetization and, in a superconducting magnet, changes in magnet field. Flux creep is often ignored in strong-pinning superconducting materials. In particular, the critical state model assumes that there is no flux creep.[2] However, flux creep has been found to be a problem in accelerator dipole magnets.[8-10] The activation energy for flux creep is reduced by the Lorentz force of the applied field on vortex currents.[11] Flux flow results as a limiting case when flux vortices are no longer pinned at high fields.

Flux jumps. Flux jumps are sudden unpinning of flux vortices in response to instabilities, temperature increases, and breakdown in shielding currents as the applied field is changed. In wires with insufficient Cu or Cu-alloy stabilizer, flux jumps could lead to a quench. Flux jumps result in sudden drops in magnetization and could result in small changes in the field of a magnet.

Eddy currents. Eddy currents arise in the normal matrix material in response to a field change according to the classical mechanism dependent on the skin depth. The time constant of the eddy currents, a function of resistivity, is short. These eddy currents are differentiated from those that couple filaments, discussed above.

MAGNETIC MEASUREMENTS

The magnetic parameters of interest in evaluating multifilar Nb-Ti wire for the SSC may be obtained from measurements of magnetization as a function of field, time, and transport current. Ideally, measurements on cable samples should be also obtained. For a useful analysis, it is necessary to know the critical current density of the wire at several fields. In addition, the wire should be characterized by filament diameter, filament spacing, filament twist pitch, number of filaments, sample volume, and matrix-to-superconductor volume ratio. Magnetization values are usually reported per unit volume of superconductor or of total composite.

Magnetization in filamentary superconductors is the signal from superconductor shielding currents and other matrix currents discussed above. The magnetization-field cycle, or hysteresis loop, should have a variable cycle time, up to several hours, to extract time-dependent coupling information. The field should be transverse to the wire axis and cycle from zero to positive value. Additional information may be obtained from longitudinal-field measurements. Transport current could be controlled independently of the applied field, though in actual SSC operation the current would be approximately proportional to the field.

Total magnetic loss is the area enclosed by the loop in the magnetization-field plane. In the limit where coupling currents have decayed, the remaining area represents the magnetic hysteresis. The width of the loop at relatively high fields may be used to compute an "effective" filament diameter,[12] according to the Bean model,[13] if the critical current density is known. If coupling currents have not decayed or if filaments are coupled by the proximity effect, a large loop area will result.

Magnetization vs. Field

Several methods of magnetometry might be used for the magnetization measurements: integrated-flux, vibrating-sample (VSM), vibrating-coil (VCM), SQUID, and Hall-probe. We will discuss their advantages and disadvantages. To our knowledge, VCM and Hall-probe magnetometers have not been used for magnetic measurements of superconductors. They may be well suited for this task in a wire-fabrication environment.

Integrated-flux. This method[14,15] is good for measurements on wires carrying transport current. It detects flux jumps and frequency dependence. It requires large samples to increase the signal-to-noise ratio. Integration instrumentation limits the measurement to relatively fast field cycles.

VSM. Vibrating-sample magnetometer measurements are made with the vibration axis longitudinal[16] or transverse[17] to the field. This method is sensitive to small samples. It is a dc measurement when the field is stepped and the signal is allowed to stabilize. However, if synchronous detection is used or if the pick-up coils are well matched, data may be taken while sweeping the field. It is difficult to vibrate samples with current leads attached. We calibrate the pick-up coils with Ni wires, plates, cylinders, or spheres in the same configuration as the superconductor samples.

VCM. A vibrating-coil magnetometer[18,19] would be good for measurements on samples carrying transport current because the sample remains stationary. As with a VSM, the VCM may be used in stepped or swept fields. A wire sample could be formed into a coil, noninductively wound to avoid a magnetic signal from the transport current in the sample. As with a VSM, the field is supplied by an external magnet. The applied field should be uniform to avoid field-induced signals. Calibration would be similar as for a VSM.

SQUID. This method[20,21] is extremely sensitive and precise, suited to small samples. Any current to the sample would disrupt the SQUID circuitry. Field cycles are extremely slow.

Hall-probe. Two calibrated, cryogenic probes are used, one to measure the applied field, the other to measure the flux density at the sample surface.[22-24] The difference is the sample magnetization (after correcting for demagnetizing field, if necessary). The Hall probe could be positioned so the Hall element is parallel to the azimuthal magnetic field from the current, but perpendicular to the magnetic field and the magnetic moment from the superconducting shielding currents. This method would be appropriate for cable samples. Calibration may be achieved as for a VSM.

AC Susceptibility vs. Temperature

AC susceptibility is usually measured as a function of temperature in constant ac field, with or without a dc bias field. Measurements are made with a coaxial mutual-inductance system consisting of a primary excitation field coil, a secondary pick-up coil, and a secondary compensation coil.[25,26] Susceptibility is an excellent tool for determining critical temperatures and proximity-effect coupling in fine-filament superconductors.[27] Low frequencies are used to avoid eddy currents in the normal-metal matrix.

STUDY OF PROTOTYPE SSC WIRES AND CABLES

A disconcerting problem in accelerator magnets is field change over several hours at constant magnet current. This is often expressed as instability in multipole fields.[1,8,9] Possible mechanisms are flux creep and eddy-current coupling between filaments. If the mechanism is flux creep, there are two possibilities. One is flux creep intrinsic to the Nb-Ti superconductor filaments or their surface. The other is flux creep in the proximity-coupled matrix. (The proximity coupling itself is not time dependent.) The presence of proximity-effect coupling in filamentary superconducting wire may be deduced from measurements of magnetization vs. field or magnetic susceptibility vs. temperature.

Proximity-Effect Coupling

In hysteresis loops of magnetization vs. field, proximity coupling causes a magnetization peak centered near zero field.[28,29] (The exact position depends on a demagnetization correction of the field axis.) This peak is different from the peak in the second and fourth quadrants which is seen experimentally and predicted by the Kim model for critical current density.[30] The coupling peak arises from a large effective filament diameter when filaments are coupled at low field. The proximity coupling is destroyed at fields greater than about 0.2 T.

In ac susceptibility measurements, a large coupling peak in the imaginary part may be seen as a function of temperature. This peak represents hysteresis loss when the lower critical field of the proximity-coupled matrix becomes on the order of the measuring field as temperature increases. Thus, the peak temperature is a strong function of measuring field amplitude. We have used this technique to study intergranular coupling in high-temperature superconductors.[31]

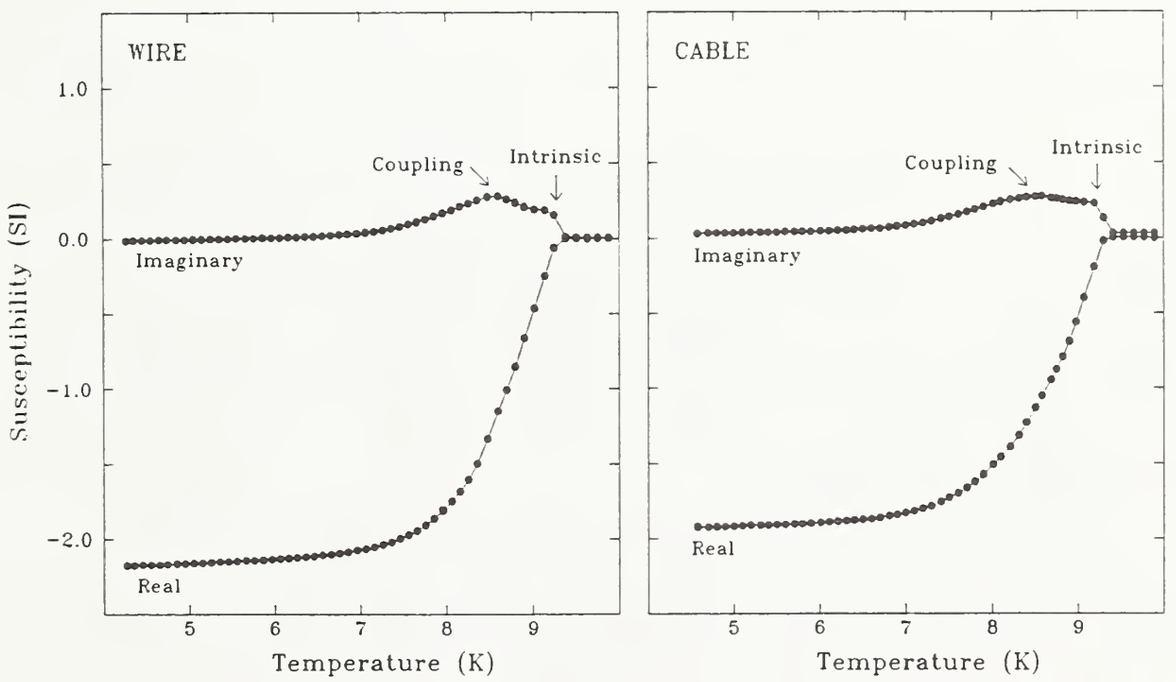

Fig. 1. AC susceptibility (uncorrected for demagnetization factor) vs. temperature measured at 0.1 mT rms at 10 Hz for wire and cable samples. The imaginary part shows intrinsic and coupling loss peaks. The real part shows a broad transition which includes intrinsic and coupling transitions.

Figure 1 shows the real and imaginary parts of external (not corrected for demagnetization factor) ac susceptibility as functions of temperature for samples consisting of small, sawed segments of prototype SSC wire and cable with 0.5% Mn in the Cu matrix. The filament diameter is 5.3 μm and the filament spacing is 0.53 μm. The susceptibility is plotted per unit volume of Nb-Ti. The measuring field was 0.1 mT rms at 10 Hz applied perpendicular to the wire and cable axes. The cable was the type used in the fabrication of the inner layer of dipole magnet D-15A-6 in Ref. 1.

Intrinsic and coupling loss peaks (partially overlapping) appear in the imaginary part of susceptibility. Correction for demagnetization factor would change the apparent shapes of the peaks. For a measuring field of 0.01 mT, the coupling peaks move to higher temperature. For a 1-mT field, the peaks are well separated as the coupling peaks move to lower temperature. Much less pronounced susceptibility peaks were seen for fields applied parallel to the wire and cable axes. But similar coupling peaks in the imaginary part were seen for wire and cable used for the outer layer of dipole magnet D-15A-6. The filaments are coupled at low temperature for low fields despite the Mn doping of the matrix. As expected, magnetization vs. field at 4 K showed characteristic coupling peaks near zero field.

Multipole-field instability occurs at the relatively high fields that would destroy proximity-effect coupling. However, there are portions of a dipole magnet which are exposed to very small fields where coupling is presumably intact. In multifilamentary wires that are proximity coupled, flux creep *may* occur in the interfilamentary matrix. We recently proposed this mechanism to explain subtle intergranular frequency effects in the ac susceptibility of high-temperature superconductors.[32] To inhibit low-field proximity coupling, more Mn could be added to the matrix, or a resistive Cu-Ni matrix could be used.

Intrinsic Flux Creep

In addition to the possibility of flux creep in the proximity-coupled matrix, there may be intrinsic flux creep in the superconducting filaments. Flux creep[10] has been observed in Tevatron cable made with wire containing presumably decoupled filaments separated by approximately 3 μm.

We measured positive-field VSM hysteresis loops for a small segment of D-15A-6 outer-layer cable, filament diameter 4.3 μm and filament spacing 0.43 μm, to see if there were time effects. The maximum field was 1 T, high enough to uncouple the filaments, perpendicular to the cable axis and parallel to the wide side. The field was stepped in units of 50 mT. For one cycle, magnetization was recorded after waiting 30 seconds after a field change. The wait time was 3 minutes for the other cycle. There was no significant difference in the hysteresis loops. This suggests an absence of intrinsic flux creep *on the time scale of these measurements*.

Eddy-Current Filament Coupling

If multipole-field instability arises from eddy-current filament coupling, more twist per unit length would help alleviate it. However, because the coupling currents decay quickly in the resistive matrix,[33] they should not be a factor for the drift of multipole fields over a period of hours.

To check for this time-dependent effect, we measured hysteresis loops, using the two field cycles described above, for two coiled samples of D-15A-6 wire used in the inner- and outer-layer cables. The field was applied along the axis of the coils, approximately transverse to the wire axis. These particular samples had 0.5 and 1.5 twists per centimeter, respectively,

verified by etching in nitric acid the matrix of companion samples. Unlike the short cable segment described above, the length of wire for each coil sample was about 25 cm, long enough to contain many twists. There were no differences between long and short field cycles for the two coils. The result suggests that 0.5 twist per centimeter is adequate to inhibit eddy-current filament coupling for these wait times.

CONCLUSIONS

We have discussed several magnetic parameters to be considered in testing multifilar Nb-Ti superconductor for the SSC, with the goal of minimizing field nonuniformity, field instability, large residual fields, and large energy losses. These parameters may be extracted from measurements of magnetization vs. field. Several measurement methods, each with certain advantages, were described.

Measurements of ac susceptibility of candidate SSC wires and cables demonstrate proximity-effect coupling. Flux creep in the proximity-coupled matrix may be a source of time variations of multipole fields in prototype SSC magnets. Intrinsic flux creep was not observed over a period of minutes. Wires used for the inner and outer layers of the D-15A-6 prototype SSC dipole magnet did not show serious eddy-current filament coupling for these sample twist pitches.

ACKNOWLEDGMENTS

We had helpful discussions with C. E. Taylor, R. M. Scanlan, W. S. Gilbert, E. W. Collings, and D. C. Larbalestier. R. J. Loughran assisted with the VSM measurements. Sample wires and cables were generously provided by R. M. Scanlan. This work was supported by the Department of Energy, Division of High Energy Physics.

REFERENCES

1. W. S. Gilbert, R. F. Althaus, P. J. Barale, R. W. Benjegerdes, M. A. Green, M. I. Green, and R. M. Scanlan, Magnetic field decay in model SSC dipoles, *IEEE Trans. Magn.* 25:1459 (1989).
2. Y. B. Kim, C. F. Hempstead, and A. R. Strnad, Magnetization and critical supercurrents, *Phys. Rev.* 129:528 (1963).
3. M. N. Wilson, "Superconducting Magnets," Oxford University Press, Oxford, U.K. (1983), pp. 171-174.
4. *Ibid.*, pp. 139-140, pp. 194-197, p. 308.
5. L. F. Goodrich and S. L. Bray, Current capacity degradation in superconducting cable strands, *IEEE Trans. Magn.* 25:1949 (1989).
6. E. W. Collings, Stabilizer design considerations in fine-filament Cu/NbTi composites, *Adv. Cryo. Engr. (Materials)* 34:867 (1988).
7. G. H. Morgan, Theoretical behavior of twisted muticore superconducting wire in a time-varying uniform magnetic field, *J. Appl. Phys.* 41:3673 (1970).
8. D. A. Herrup, M. J. Syphers, D. E. Johnson, R. P. Johnson, A. V. Tollestrup, R. W. Hanft, B. C. Brown, M. J. Lamm, M. Kuchnir, and A. D. McInturff, Time variations of fields in superconducting magnets and their effects on accelerators, IEEE Trans. Magn. 25:1643.
9. R. W. Hanft, B. C. Brown, D. A. Herrup, M. J. Lamm, A. D. McInturff, and M. J. Syphers, Studies of time dependence of fields in Tevatron superconducting dipole magnets, *IEEE Trans. Magn.* 25:1647.
10. M. Kuchnir and A. V. Tollestrup, Flux creep in a Tevatron cable, *IEEE Trans. Magn.* 25:1839.

11. P. W. Anderson and Y. B. Kim, Hard superconductivity: Theory of the motion of Abrikosov flux lines, *Rev. Mod. Phys.* 36:39 (1964).
12. S. S. Shen, Magnetic properties of multifilamentary Nb_3Sn composites, *in:* "Filamentary A15 Superconductors," M. Suenaga and A. F. Clark, eds., Plenum, New York (1980), pp. 309-320.
13. C. P. Bean, Magnetization of high-field superconductors, *Rev. Mod. Phys.* 36:31 (1964).
14. W. A. Fietz, Electronic integration technique for measuring magnetization of hysteretic superconducting materials, *Rev. Sci. Instrum.* 36:1621 (1965).
15. M. N. Wilson, *op. cit.*, pp. 243-245.
16. P. J. Flanders, Instrumentation for magnetic moment and hysteresis curve measurements, *in:* "Conference on Magnetism and Magnetic Materials," American Institute of Electrical Engineers, New York (1957), T-91, pp. 315-317.
17. S. Foner, Versatile and sensitive vibrating-sample magnetometer, *Rev. Sci. Instrum.* 30:548 (1959).
18. D. O. Smith, Development of a vibrating-coil magnetometer, *Rev. Sci. Instrum.* 27:261 (1956).
19. K. Dwight, N. Menyuk, and D. Smith, Further development of the vibrating-coil magnetometer, *J. Appl. Phys.* 29:491 (1958).
20. E. J. Cukauskas, D. A. Vincent, and B. S. Deaver Jr., Magnetic susceptibility measurements using a superconducting magnetometer, *Rev. Sci. Instrum.* 45:1 (1974).
21. J. A. Good, A variable temperature high sensitivity SQUID magnetometer, *in:* "SQUID: Superconducting Quantum Interference Devices and their Applications," H. D. Hahlbohm and H. Lübbig, eds., Walter de Gruyter, Berlin (1977), pp. 225-238.
22. D. A. Berkowitz and M. A. Schippert, Hall effect B-H loop recorder for thin magnetic films, *J. Sci. Instrum.* 43:56 (1966).
23. D. J. Craik, The measurement of magnetization using Hall probes, *J. Phys. E: Sci. Instrum.* 1:1193 (1968).
24. P. J. Flanders, A Hall sensing magnetometer for measuring magnetization, anisotropy, rotational loss and time effects, *IEEE Trans. Magn.* 21:1584 (1985).
25. W. R. Abel, A. C. Anderson, and J. C. Wheatley, Temperature measurements using small quantities of cerium magnesium nitrate, *Rev. Sci. Instrum.* 35:444 (1964).
26. R. B. Goldfarb and J. V. Minervini, Calibration of ac susceptometer for cylindrical specimens, *Rev. Sci. Instrum.* 55:761 (1984).
27. J. R. Cave, A. Février, H. G. Ky, and Y. Laumond, Calculation of ac losses in ultra fine filamentary NbTi wires, *IEEE Trans. Magn.* 23:1732 (1987).
28. A. K. Ghosh, W. B. Sampson, E. Gregory, and T. S. Kreilick, Anomalous low field magnetization in fine filament NbTi conductors, *IEEE Trans. Magn.* 23:1724 (1987).
29. E. W. Collings, K. R. Marken Jr., M. D. Sumption, R. B. Goldfarb, and R. J. Loughran, AC loss measurements of two multifilamentary NbTi composite strands, paper AY-05, this conference.
30. D.-X. Chen and R. B. Goldfarb, Kim model for magnetization of type-II superconductors, *J. Appl. Phys.* 66:2510 (1989).
31. R. B. Goldfarb, A. F. Clark, A. I. Braginski, and A. J. Panson, Evidence for two superconducting components in oxygen-annealed single-phase Y-Ba-Cu-O, *Cryogenics* 27:475 (1987).
32. M. Nikolo and R. B. Goldfarb, Flux creep and activation energies at the grain boundaries of Y-Ba-Cu-O superconductors, *Phys. Rev. B* 39:6615 (1989).
33. M. N. Wilson, *op. cit.*, pp. 176-181.

Contribution of the National Institute of Standards and Technology, not subject to copyright.

Hall Probe Magnetometer for SSC Magnet Cables: Effect of Transport Current on Magnetization and Flux Creep

R. W. Cross and R. B. Goldfarb
Electromagnetic Technology Division
National Institute of Standards and Technology
Boulder, Colorado 80303

Abstract

We constructed a Hall probe magnetometer to measure the magnetization hysteresis loops of Superconducting Super Collider magnet cables. The instrument uses two Hall-effect field sensors to measure the applied field H and the magnetic induction B. Magnetization M is calculated from the difference of the two quantities. The Hall probes are centered coaxially in the bore of a superconducting solenoid with the B probe against the sample's broad surface. An alternative probe arrangement, in which M is measured directly, aligns the sample probe parallel to the field. We measured M as a function of H and field cycle rate both with and without a dc transport current. Flux creep as a function of current was measured from the dependence of ac loss on the cycling rate and from the decay of magnetization with time. Transport currents up to 20% of the critical current have minimal effect on magnetization and flux creep.

Introduction

A consideration in the design of Superconducting Super Collider (SSC) magnet cables is ac losses in the superconductor. These ac losses may be either time-dependent or time-independent [1]. Normally, ac loss measurements are made on open-circuited samples. In actual use, however, the superconductor carries a transport current which can influence the ac loss of the sample [2–4]. Another concern in SSC cable design is magnetic relaxation in the filaments. Measurements of large field decays in accelerator magnets, attributed to flux creep, have been reported [5–8]. However, the observed field decay in the magnets is much larger than the relaxation measured in small open-circuited samples.

The objective of this study was to examine the effect of transport current on the magnetization and the magnetic relaxation in an SSC cable carrying transport current. We describe a Hall probe magnetometer that can measure magnetization, ac losses, and flux creep, with and without transport current [9]. The magnetometer uses two Hall-effect field sensors. One measures the applied field H and the other measures the magnetic induction B or the magnetization M. Hall probe magnetometers have been used to study ferromagnetic materials, ferrites, anisotropy fields, superconducting tubes, and field profiles [10–13].

Experiment

A schematic diagram of the Hall probe magnetometer is shown in Fig. 1. The applied field is supplied by a superconducting solenoid, 21 cm in length, 7.6 cm bore, with a maximum field of 7 T. Two cryogenic Hall-effect field sensors are used; one measures the applied field H and the other measures the magnetic induction B. Both probes are aligned perpendicular to the applied field and centered coaxially in the bore of the solenoid. Their vertical separation is 4 cm. The sample is mounted so that its broad face is perpendicular to the field with the B probe mounted firmly against it. The self field from the transport current is parallel to the B probe and, ideally, is not detected. Any self field actually sensed by the B probe appears simply as a dc offset in the hysteresis loops.

The fields H and B are measured with two commercial gaussmeters. Their analog outputs are low-pass filtered and input to a differential amplifier, which subtracts the signals, and sent to a computer, which calculates M. Magnetization can be calculated using the expression $M = (B/\mu_0 - H)/(1-D)$, where D is the demagnetizing factor, approximately equal to 0.5 for the transverse field orientation.

A U-shaped sample is used so that the current contacts can be soldered to the cable far enough from the Hall probe sensing area to not affect the measurement. To obtain repeatable results, the sample must be positioned accurately, with the face of the sample firmly against probe B and properly centered. This is achieved with three guide tubes and a Be-Cu-spring-loaded mount for probe B. The insert is shown in Fig. 2. (Only two guide tubes are shown for clarity.) Samples are mounted to the sample plate using clamps at both ends of the sample. The sample plate is 6.1 cm in diameter, which allows for samples approximately 5.3 cm in length to be mounted. The guide tubes are used for support and for sample positioning. The tubes are symmetrically spaced so that the circular sample plate can slide firmly between them. The sample rod can easily be removed and loaded while the probes and the solenoid remain immersed in liquid helium.

The instrument may be calibrated with a Ni standard the same size as the sample or with a superconductor transfer standard which has been measured on a conventional magneto-

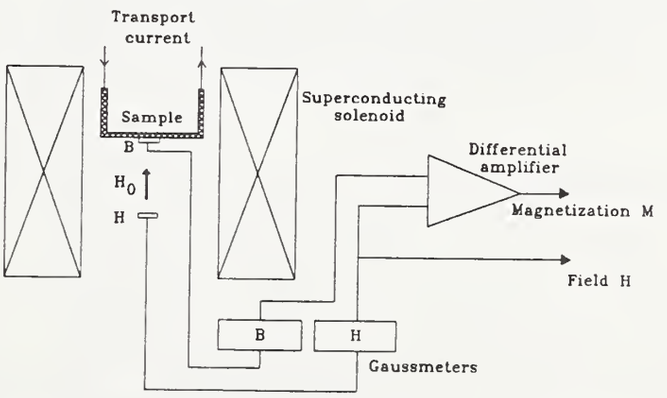

Figure 1. Schematic diagram of the Hall probe magnetometer. The magnetic field H_0 is supplied by a superconducting solenoid. The sample is bent into a U-shape so that the solder contacts can be made away from the Hall probe sensing area.

Contribution of the National Institute of Standards and Technology, not subject to copyright.
Manuscript received September 24, 1990.

U.S. Government work not protected by U.S. Copyright.

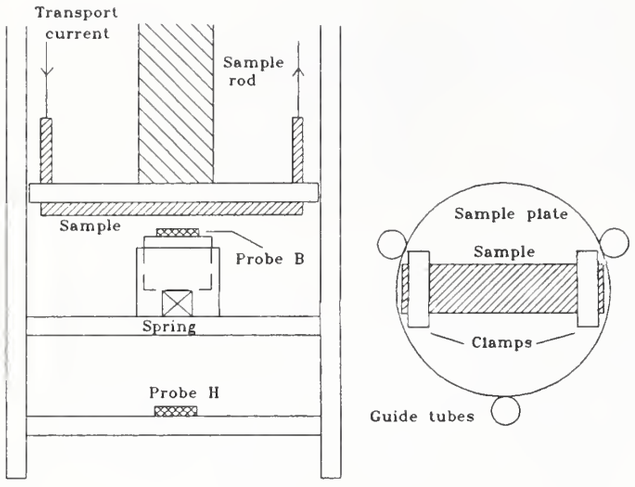

Figure 2. Mechanical diagram of the Hall probe magnetometer showing the sample mounting assembly. Probe *B* is in a spring-loaded holder which assures contact to the sample. The guide tubes support the probes and direct the sample plate to probe *B*.

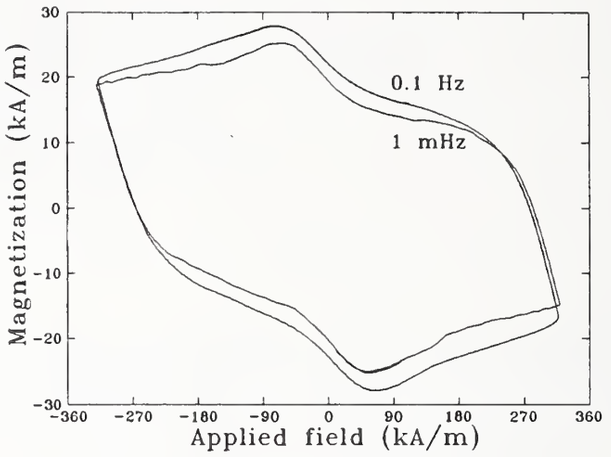

Figure 3. Plot of magnetization versus field at 0.1 Hz and 1 mHz. The difference in loss between the two curves is the result of eddy current coupling of the filaments at the higher frequency.

meter. The Hall-effect sensors must be calibrated before the measurements. This is done by removing the sample, setting the field to a known value, and adjusting the gain of the meters until each gaussmeter displays the correct field value. A disadvantage of Hall effect field sensors is their nonlinearity above 3 T, typically 0.2%. For small values of *M* in large fields, the nonlinearity can lead to distortion in *M*. The problem can be mitigated if values of the background signal as a function of field are subtracted from the sample data during data processing.

An alternative Hall probe arrangement increases the sensitivity of the *M* measurement. In this arrangement, the sample probe is aligned so that its sensing plane is *parallel* rather than perpendicular to the applied field and *M* is measured directly. We call this the "*M* configuration," as distinct from the usual "*B* configuration." A disadvantage of this technique is that the alignment of the *M* probe must be precise to avoid sensing the applied field.

The sample used for the measurements was a Nb–Ti multifilamentary SSC magnet cable with 23 strands. Each strand had approximately several thousand filaments, 4.2 μm in diameter. Only three of the 23 strands were used in the transport current measurements so that the applied current, limited by the power supply, would be closer to the critical current of the sample. All measurements were made at 4.0 K.

Results

Magnetization versus Field

A direct measure of magnetic hysteresis loss can be obtained from magnetization-versus-field loops. Time dependent losses, such as flux creep and eddy current coupling, can be measured if the applied field is swept at different cycling rates [1]. Figure 3 shows a typical plot of magnetization versus field for two field cycle rates. The sample was a short section of cable with no applied transport current. The response of the Hall probes is fast enough to measure the higher frequencies with excellent resolution. As seen in Fig. 3, the area of the hysteresis loop is greater for the 0.1 Hz field cycle rate than for 1 mHz. At 0.1 Hz, the eddy currents generated in the copper matrix have not yet decayed and still couple the filaments, which leads to larger ac loss. At very low frequencies, other time-dependent effects, such as flux creep, can be measured as a small decrease in hysteresis as the field cycle rate decreases. For example, we observed an average 2.5% reduction in magnetization on comparing curves at 5 and 0.5 mHz (not shown).

The effect of transport current on the magnetization curves is presented in Fig. 4. The sample consisted of three strands of wire. Curves are shown for 0 and 200 A of transport current. The critical current for the three strands is estimated to be 1 kA at zero field. The effect of the applied current is seen as a small decrease in magnetization at high fields as the critical current is reduced. This effect would be more pronounced at higher fields or currents [14].

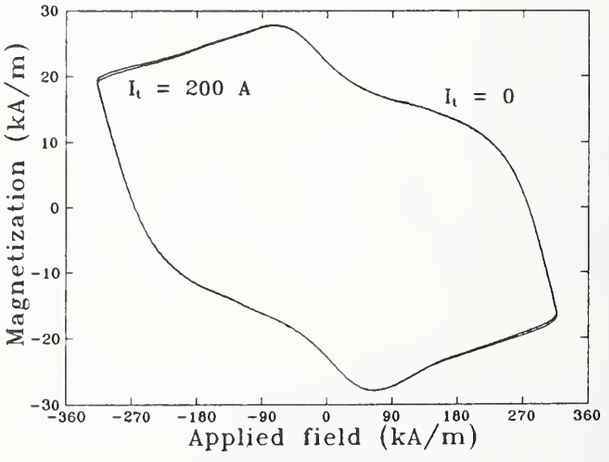

Figure 4. Plot of magnetization versus field for 0 and 200 A of transport current. The effect of the applied current is small, showing a decrease in hysteresis only at the higher field values due to the reduction in critical current.

Flux Creep and Transport Current Effects

There should be an effect of transport current on flux creep, considering the increase of the Lorentz force acting on the pinned flux vortices. The Hall probe magnetometer is well suited for flux creep measurements with and without transport current because it does not require sample motion for signal detection. Unexpected variations in field in other dc methods can give erroneous results in hysteretic materials. For example, VSM and SQUID magnets might have enough field inhomogeneity to cause minor hysteresis loops to be traversed during sample motion.

The decay in magnetization as a function of time for 0 and 200 A of transport current are shown in Fig. 5. The measurements were made on three strands in the M configuration at a field of 0.3 T, after a field cycle of 0 to 6 T, 6 to 0 T, and 0 to 0.3 T. The dc current was applied at the start of the field cycle. After switching the magnet into persistent mode, magnetization was measured as a function of time. The field decay of the solenoid during the measurement was negligible as monitored at the H probe.

The data in Fig. 5 include the fast decay resulting from the dissipation of eddy currents. The fast decay is large and nearly complete in less than 100 sec. After that, there is a slow decay of only a few percent of the initial magnetization that continues beyond our measuring time. As seen from the graph, the effect of transport current is minimal. Field-decay effects observed in accelerator magnets occur at low current levels, usually less than 20% of the critical current. From these results, it seems that the effect of transport current on flux creep is not large enough to explain the field decay in SSC magnets.

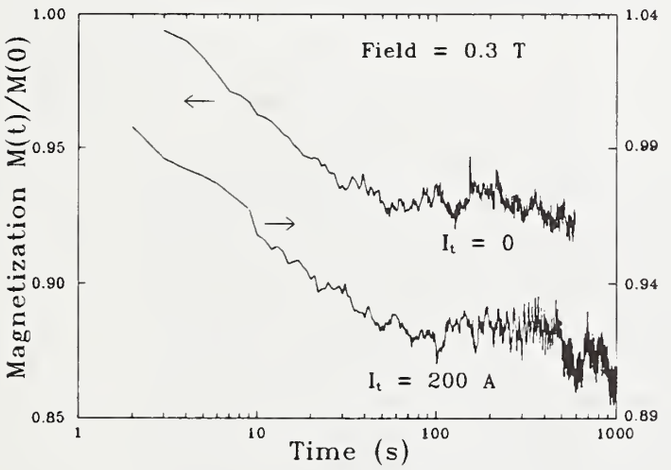

Figure 5. Plot of magnetization versus time at 0.3 T for 0 and 200 A of transport current I_t. The left scale is for zero transport current; the right scale is for 200 A. There is slight increase in decay rate with transport current.

Conclusion

A Hall probe magnetometer was constructed to measure the effect of transport current on magnetization and flux creep in SSC magnet cables. The Hall probe measurement is static; it does not require sample motion or field change to induce a signal. The speed at which the field can be cycled is limited only by the magnet inductance and the power supply compliance voltage. However, the calibration of M is not direct. The instrument sensitivity in the B configuration is less than that of other magnetometers and very small samples cannot be measured.

Transport current causes a decrease in magnetization at high fields and current. The current has a small effect on flux creep, although not enough to explain the large decay observed in SSC magnets. In the case of actual SSC dipole magnets, however, the different current levels, field cycles, and field gradients to which the cable is exposed is more complicated than in our experiments.

Acknowledgment

This work was supported by the U.S. Department of Energy, Division of High Energy Physics.

References

[1] R. B. Goldfarb and R. L. Spomer, *Adv. Cryo. Eng. (Materials)* **36**, 215 (1990).
[2] K. Kanbara, *Cryogenics* **27**, 612 (1987).
[3] W. J. Carr, Jr., M. S. Walker, and J. H. Murphy, *J. Appl. Phys.* **46**, 4048 (1975).
[4] S. S. Shen and R. E. Schwall, *IEEE Trans. Magn.* **15**, 232 (1979).
[5] D. A. Herrup, M. J. Syphers, D. E. Johnson, R. P. Johnson, A. V. Tollestrup, R. W. Hanft, B. C. Brown, M. J. Lamm, M. Kuchnir, and A. D. McInturff, *IEEE Trans. Magn.* **25**, 1643 (1989).
[6] R. W. Hanft, B. C. Brown, D. A. Herrup, M. J. Lamm, A. D. McInturff, and M. J. Syphers, *IEEE Trans. Magn.* **25**, 1647 (1989).
[7] M. Kuchnir and A. V. Tollestrup, *IEEE Trans. Magn.* **25**, 1839 (1989).
[8] W. S. Gilbert, R. F. Althaus, P. J. Barale, R. W. Benjegerdes, M. A. Green, M. I. Green, and R. M. Scanlan, *Adv. Cryo. Eng. (Materials)* **36**, 223 (1990).
[9] R. W. Cross and R. B. Goldfarb, *Department of Energy Topical Workshop on Magnetic Effects of Persistent Currents in Superconductors*, 5–7 March 1990, Batavia, Illinois.
[10] P. J. Flanders, *IEEE Trans. Magn.* **21**, 1584 (1985).
[11] D. J. Craik, *J. Phys. E: Sci. Instrum.* **1**, 1193 (1968).
[12] M. R. Cimberle, C. Ferdeghini, and A. S. Siri, *Cryogenics* **29**, 69 (1989).
[13] D. D. Roshon, Jr., *Rev. Sci. Instrum.* **33**, 201 (1962).
[14] M. N. Wilson, *Superconducting Magnets*, Clarendon Press, Oxford, U.K. (1983), pp. 171–174.

To be published in:
Advances in Cryogenic Engineering (Materials), Vol. 38
Edited by F. R. Fickett and R. P. Reed
Plenum Press, New York, 1992

TRANSPORT CURRENT EFFECTS ON FLUX CREEP AND MAGNETIZATION IN Nb–Ti MULTIFILAMENTARY CABLE STRANDS

R. W. Cross

Electromagnetic Technology Division
National Institute of Standards and Technology
Boulder, Colorado 80303

ABSTRACT

We used a Hall-probe magnetometer to measure the effect of transport current on magnetization and flux creep in Nb-Ti multifilamentary cable strands. Large transport currents, up to 70% of the critical current I_c, were applied to the sample. The external field was applied transverse to the current and sample length. When the applied current approached the critical current of the strand, the magnetization decreased and the Lorentz-force interaction between the field and the transport current dominated the creep. Both the short-time and long-time decay of magnetization increased. The increase in the short-time decay was too large to be explained by eddy current decay. The long-time decay was enhanced by a factor of 4 with a transport current of approximately $0.7I_c$.

INTRODUCTION

Previously, we reported experimental effects of transport current on magnetization in Superconducting Super Collider (SSC) cables at current and field values which simulated dipole magnet operation at the injection field.[1] In actual use, the superconducting cables carry a transport current which can affect the ac losses of the sample.[2-4] We found that applied currents up to 20% of the critical current I_c at the injection field only sightly affected the magnetization. The current reduced the magnetic hysteresis by less than 5%, which was seen only at high fields. In addition, the magnetic relaxation of the shielding currents in the filaments was measured with and without a transport current at the injection field value of 0.3 T. We performed the experiment to determine whether the presence of a transport current would increase the decay due to the Lorentz-force interaction and to see if it could explain the large field decay observed in the model dipole magnets. Others reported that flux creep in the filaments may be causing the enhanced field decay,[5-8] but the observed decay measured in open-circuited samples was too small to explain the field drift in the magnets. We found that a current of approximately $0.2I_c$ at the injection field could not account for the field drift in the magnets, although the current did slightly increase the decay.

In this study, we investigate the effect of transport current on flux creep and magnetization in Nb-Ti magnet cable strands at higher currents where the Lorentz-force interaction between the current and flux vortices starts to dominate the creep. In model SSC dipole magnets, the different currents, field cycles, and field gradients to which the cable is exposed are very complicated. In operation the field is cycled from 0 to 6 T, where the applied current is close to the critical current of the cable, back to 0 T, and then finally to the injection field of 0.3 T. The objective of this study is to measure magnetization and relaxation in the presence of a large transport current to determine whether a large current causes a major increase in the decay.

EXPERIMENT

To measure the magnetic relaxation in SSC cables with a transport current, we developed a Hall probe magnetometer, described in Ref. 1. For this experiment, we use a Hall-effect field sensor to measure the applied field H and another to measure the magnetization M, as shown in Fig. 1. A U-shaped sample is used so that the current contacts can be soldered to the wire far from the Hall probe's sensing area. This way, any current redistribution at the contacts will not be detected. The sample is a single strand of Nb-Ti multifilamentary SSC magnet cable with approximately 4000 filaments, each 4.2 μm in diameter. We supply up to 200 A of transport current to the sample, close to the critical current of the strand. The applied field is provided by a 7.6-cm bore, superconducting solenoid with a maximum field of 7 T. All the measurements were made in liquid He at 4.0 K.

Direct measurement of the magnetization M is much more sensitive than measuring the magnetic induction B and subtracting the magnetic field H to obtain M.[9] This is especially true for superconductors, where H and B can be very large and M may be small. However, to measure M directly, it is necessary to accurately align probe M parallel to the field, so it does not sense H. The "M configuration" reduces the effect of nonlinear responses in the Hall-effect devices because the M field stays small compared to B and H, and only one probe is used to measure M.

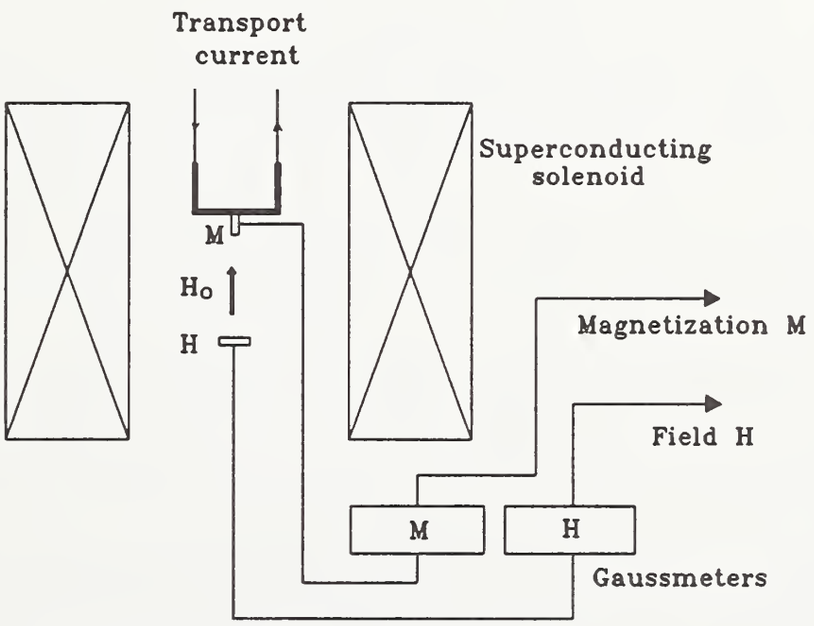

Figure 1. Schematic diagram of Hall probe magnetometer. The magnetic field H is supplied by the superconducting solenoid. The M probe is aligned parallel to the applied field near the U-shaped sample.

RESULTS AND DISCUSSION

Magnetization

To understand the effect of an applied current on magnetic hysteresis, we need to consider the interaction of the current and field and its effect on the field profile in the sample. For simplicity, we consider a superconducting slab carrying an applied current I_t and magnetic shielding currents

I_m. The transport current is maintained at a constant level so the only effect of the changing field is to alter the magnetization currents.[10] The field penetration profile, based on the critical-state model, is shown in Fig. 2. In Fig. 2(a) the sample is exposed to a field and a current. The current shifts the profile to one side, because on one side of the sample the applied current and the shielding currents add, and on the other side of the sample the currents subtract. As the field is reversed [Fig. 2(b)-(d)], the magnetic shielding currents penetrate in the opposite direction to a full-penetration field H_p [Fig. 2(c)], where the field change penetrates the entire slab, and then finally to the maximum reverse field H_m [Fig. 2(d)]. Wilson[10] showed that full penetration occurs at a lower field amplitude than the case with zero applied current. The penetration field H_p is reduced by a factor of $(1 - i)$, where i is the ratio of transport current to critical current I_t/I_c. The magnetization is reduced in the presence of a transport current by a factor of $(1 - i^2)$. In summary, the effect of a transport current is to shift the field profile, which causes a reduction of the penetration field H_p and a reduction of the magnetization M.

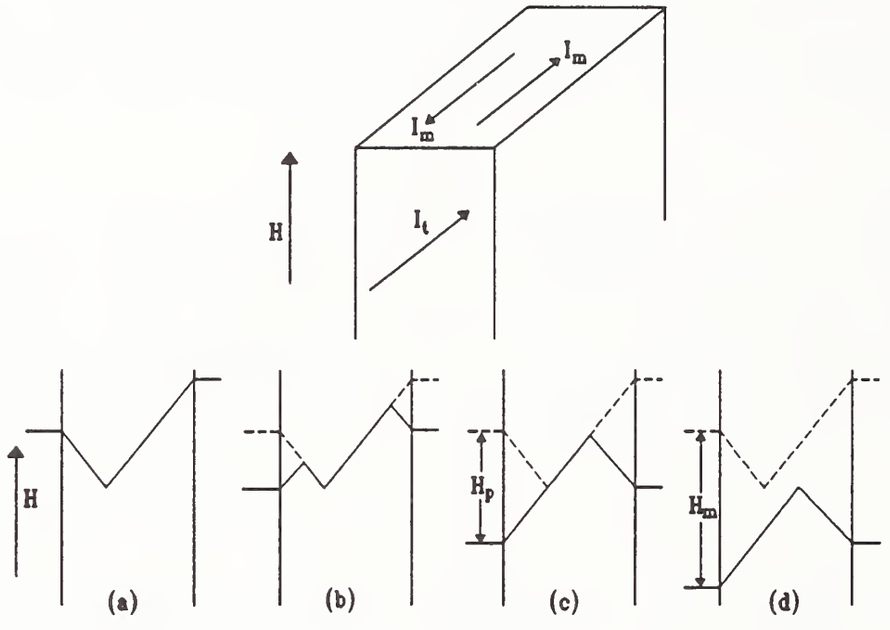

Figure 2. (a) Field profile for a superconducting slab carrying a dc transport current in an external field; (b) as the field is reduced; (c) when the field penetrates the entire slab; (d) when the field reaches its opposite maximum value. After Wilson.[10]

In Fig. 3, we show a plot of magnetization versus applied field for the SSC cable strand at different applied currents. We show only the positive-field portion of the curve for clarity, though the field was cycled between ± 0.5 T. A complete field cycle is traversed after the current is applied so that a critical-state profile can be established. There are two notable effects of the transport current: (1) As the transport current is increased from 0 to 120 A (approximately $0.4I_c$), the width of the magnetization curve ΔM decreases, especially at higher fields. This may be understood from the $(1 - i^2)$ dependence of magnetization with current; as I_t increases, i approaches 1 and M goes to 0. The reduction of ΔM is proportionally larger at higher fields because of the dependence of critical current on field; as H increases, I_c decreases and i approaches 1. (2) The field value for the minimum magnetization decreases with increasing applied current (see inset). This results from the shift in the full penetration field H_p, which is reduced by $(1 - i)$.

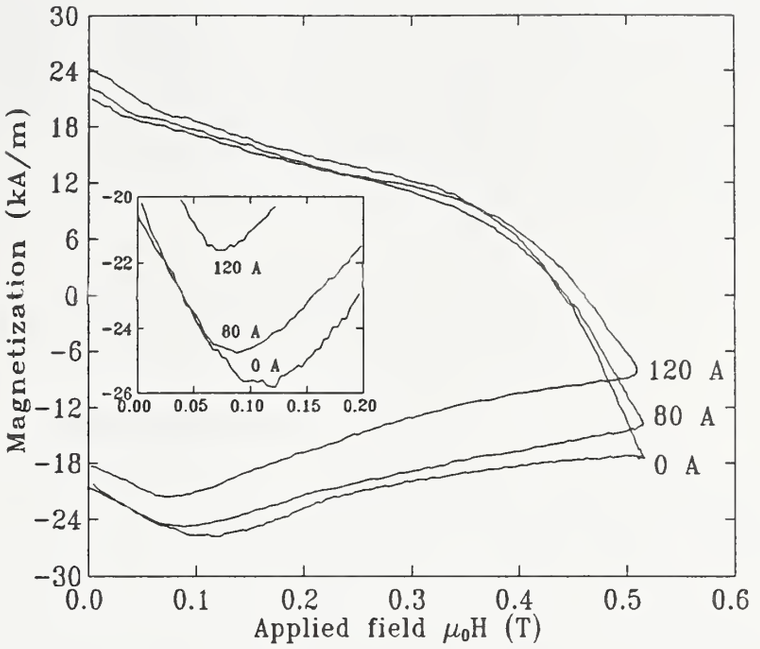

Figure 3. Plot of magnetization versus field for 0, 80, and 120 A of transport current. The current causes the hysteresis width to decrease, especially at higher fields. The field value for minimum magnetization also decreases with increasing current (inset).

Flux creep

At temperature $T = 0$ K, vortices are pinned by material inhomogeneities and will not move under action of a Lorentz force density $J \times B$ if the net current density $J = \nabla \times B/\mu_0$ is less than the critical current density J_c. At $T > 0$, some of the vortices are unpinned by thermal activation. If the spatial dependence of the pinning potential is tilted by a flux-density gradient, the thermally activated vortices may develop a drift velocity, causing dissipation. This process is called flux creep. If a transport current is present, the increase in the Lorentz-force interaction between the current J (which includes both the transport and shielding currents) and the vortices can increase the rate of relaxation. If the transport current approaches the critical current of the sample, the interaction of the applied current and field can dominate the flux creep, leading to a large magnetic relaxation.

The decay in magnetization as a function of time for 0 and 200 A of transport current is shown in Fig. 4. The measurements were made on the single SSC cable strand at a field of 0.3 T, after a field cycle of 0 to 6 T, 6 to 0 T, and 0 to 0.3 T. The dc transport current was supplied at the start of the field cycle. Magnetization was measured as a function of time after the magnet was switched into persistent mode. The magnetization $M(t) = \Delta M(t)/2$ is normalized to $M(t)$ at time $t = 0$, where ΔM is the width of the hysteresis loop at a constant field (for a fully penetrated state). Time $t = 0$ is defined as the time of the first measured value of $M(t)$, which was taken immediately after field stability. The field decay of the solenoid magnet was negligible over the course of the experiment.

The data in Fig. 4 show how a large transport current can influence flux creep. The decay in magnetization with time has two distinct features. The first is the large decay observed in the first 10 to 20 s. For the 0-A data, this decay can be ascribed to the relaxation of eddy currents in the

copper matrix, which is related to the resistivity of the copper. However, for the 200-A data, the decay is much larger than can be attributed to eddy current decay, although the time constant is roughly the same.[1] The applied current may be causing a redistribution of the magnetic shielding and eddy currents, which results in a fast decay. The second feature is the enhancement of the long-time decay. The relaxation for the 200-A data is much larger than for the 0-A data, decaying approximately 13% in 500 s (not including the fast decay in the first 10 s) compared to the 3% decay for $I_t = 0$ A. Therefore, an application of a transport current of approximately $0.7I_c$ causes the long-time decay to increase by a factor of 4.

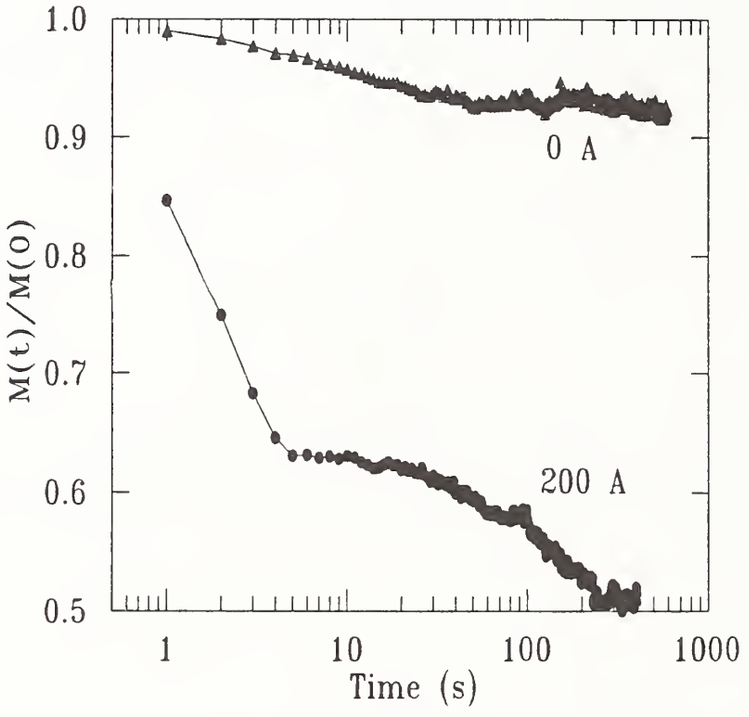

Figure 4. Plot of magnetization vs. time at 0.3 T for 0 and 200 A of transport current I_t. The transport current increases the long-time decay by a factor of 4. The short-time decay in the first 5 s of the 200-A data is much larger than the eddy-current decay seen in the 0-A data.

CONCLUSION

We used a Hall-probe magnetometer in the *M* configuration to measure the effect of a 200-A transport current on magnetization and flux creep in SSC magnet-cable strands. This configuration is more sensitive than measuring *B* and reduces the effect of nonlinear responses in the Hall-effect devices. However, alignment of probe *M* in the field produced by the solenoid is difficult.

A transport current that is large with respect to the critical current of the wire reduced the magnetization, especially at higher fields where the critical current is smaller. There is a qualitative agreement with the $(1 - i^2)$ dependence on current. The field value for minimum magnetization decreased with current and was in qualitative agreement with the $(1 - i)$ dependence. For flux creep measurements, the applied current caused an enhancement in both the short-time and long-time decay. A current of approximately $0.7I_c$ caused the decay to increase by a factor of 4. As the applied current approaches the critical current, the Lorentz force acting on the vortices starts to

exceeded the pinning force, which leads to a large decay. In the limit $I_t \rightarrow I_c$, the Lorentz force completely exceeds the pinning force, flux begins to flow, and the magnetization decays to 0. The field decay observed in the dipole magnets may be due to the complicated field and current cycle, which actually traverses large fields and currents. As we noted in Ref. 1, the field-decay effects in accelerator magnets occur at low transport currents.

ACKNOWLEDGMENTS

R. B. Goldfarb provided helpful discussions and suggestions. This work was supported by the U.S. Department of Energy, Division of High Energy Physics.

REFERENCES

1. R. W. Cross and R. B. Goldfarb, Hall probe magnetometer for SSC magnet cables: Effects of transport current on magnetization and flux creep, *IEEE Trans. Magn.* **27**, 1796 (1991).
2. K. Kanbara, Hysteresis loss of a round superconductor carrying a dc transport current in an alternating transverse field, *Cryogenics* **27**, 621 (1987).
3. W. J. Carr, Jr., M. S. Walker, and J. H. Murphy, Alternating field loss in a multifilament superconductor wire for weak ac fields superposed on a constant bias, *J. Appl. Phys.* **46**, 4048 (1975).
4. S. S. Shen and R. E. Schwall, Interaction of transport current and transient external field in composite conductors, *IEEE Trans. Magn.* **15**, 232 (1979).
5. W. S. Gilbert, R. F. Althaus, P. J. Barale, R. W. Benjegerdes, M. A. Green, M. I. Green, and R. M. Scanlan, The effect of flux creep on the magnetization field in the SSC dipole magnets, *Adv. Cryo. Engr. (Materials)* **36**, 223 (1990).
6. D. A. Herrup, M. J. Syphers, D. E. Johnson, R. P. Johnson, A. V. Tollestrup, R. W. Hanft, B. C. Brown, M. J. Lamm, M. Kuchnir, and A. D. McInturff, Time variations of fields in superconducting magnets and their effects on accelerators, *IEEE Trans. Magn.* **25**, 1643 (1989).
7. R. W. Hanft, B. C. Brown, D. A. Herrup, M. J. Lamm, A. D. McInturff, and M. J. Syphers, Studies of time dependence of fields in Tevatron superconducting dipole magnets, *IEEE Trans. Magn.* **25**, 1647 (1989).
8. M. Kuchnir and A. V. Tollestrup, Flux creep in a Tevatron cable, *IEEE Trans. Magn.* **25**, 1839 (1989).
9. P. J. Flanders, A Hall sensing magnetometer for measuring magnetization, anisotropy, rotational loss and time effects, *IEEE Trans. Magn.* **21**, 1584 (1985).
10. M. N. Wilson, "Superconducting Magnets," Clarendon Press, Oxford, U.K. (1983), pp. 171-174.

Enhanced flux creep in Nb-Ti superconductors after an increase in temperature

R. W. Cross and R. B. Goldfarb
Electromagnetic Technology Division, National Institute of Standards and Technology, Boulder, Colorado 80303

(Received 25 July 1990; accepted for publication 29 October 1990)

The magnetic fields of Superconducting Super Collider (SSC) dipole magnets change with time when the magnets are operated at constant current. The decay of the field is thought to be a consequence of flux creep in the Nb-Ti filaments in the superconducting cables. However, measured magnetic relaxation of small samples of SSC cable as a function of time is unlike the large decays that are observed in the fields of the actual magnets. We have made relaxation measurements on sample SSC conductors at 3.5 and 4.0 K after field cycling. The decay at both temperatures was 2.8% in 50 min. However, the relaxation measured after a temperature increase from 3.5 to 4.0 K was 4.8% in 50 min. A likely reason for the greater magnetization decay is that, after an increase in temperature, the Nb-Ti is in a supercritical state, with shielding currents flowing at a density greater than the new critical current density. This causes enhanced flux creep. We suggest that a small temperature rise during the operation of SSC magnets may contribute to the unexpectedly large magnetic field decay.

Synchrotron accelerators, such as the Tevatron and the proposed Superconducting Super Collider (SSC), use magnets made of cables of multifilamentary Nb-Ti superconductor wires. The magnetization of the Nb-Ti filaments contributes to the magnetic field of the accelerator magnets. Flux creep, that is, thermally activated jumps of bundles of flux vortices, produces a decay in the magnetization of superconductors with time,[1,2] and flux creep has been presumed to cause a troublesome slow decay in the field, often measured as a multipole field, of accelerator dipole magnets over a period of hours.[3–6] Magnetometer measurements of flux creep on samples of multifilamentary superconductor wire and cable used in the construction of these magnets show some flux creep.[7,8] However, after an initial rapid decay of magnetization, the flux creep is about one order of magnitude smaller than the field decay in the actual superconductor magnets.

Recently, Sun *et al.*[9] showed that flux creep in superconductors could be reduced or even eliminated by operating in a subcritical state achieved by lowering the conductor's temperature after the critical state is achieved. Clem has suggested that such a scheme, applied to accelerator magnets, might lessen the field-decay problem.[10] In this letter, we consider the inverse theorem that the enhanced flux creep seen in accelerator magnets may be a consequence of an increase in operating temperature, which forces the conductor into a supercritical state. We find that an increase in sample temperature of 0.5 K, after a typical SSC field cycle, almost doubles the rate of magnetization decay.

The sextupole fields of model SSC dipole magnets change with time when the magnets are operated at constant current under conditions similar to SSC accelerator use. Large field decays have been observed,[6,11] and such decays can result in beam loss during the SSC injection period of several hours. The logarithmic time dependence of field decay and the temperature dependence of relaxation in different dipole magnets suggest a flux creep mechanism. For example, the reported rate at 1.8 K was less than at 4.2 K.[6] However, the measured relaxation of samples of cable is generally less than the field relaxation reported for the magnets.

To examine the magnetic decay process, we made a series of three relaxation measurements at 3.5 and 4.0 K. The measurements were made with a superconducting quantum interference device magnetometer using a scan length of 2 cm, which corresponds to a field variation of $<0.01\%$. The field from a superconducting solenoid was applied perpendicular to the flat side of a 0.7 cm sample of multifilamentary Nb-Ti superconductor cable. The sample had 23 strands, each with approximately 10 000 4.2-μm-diam filaments. To simulate the original SSC field cycle, for comparison with existing field-decay data, all measurements were made after the following field cycle: 0–5 T, 2 min pause; 5–0 T, 2 min pause; 0–0.3 T, 2 min pause. The final 2 min pause was included to avoid the fast decay resulting from eddy-current coupling and to establish a reproducible initial starting time, $t=0$. The pauses ensured field stability before the measurements were taken and were in addition to the time required to ramp to each field and to switch into persistent mode.

Curves (a) and (b) in Fig. 1 for 3.5 and 4.0 K show magnetization $M(t)$ as a function of time scaled by the magnetization $M(0)$ at $t=0$. The decay rates due to thermal activation are nearly the same, about 2.8% after 3000 s, but the value of $M(0)$ is approximately 10% less at 4.0 K. The rate of decay, $R \equiv [\Delta M(t)/M(0)]/\Delta \ln t$, for the decade of time 300–3000 s, is 0.008, in good agreement with measurements by Ghosh on SSC wires.[8] It is about one-third to one-tenth the sextupole-field decay rate observed in SSC model magnets after a similar field cycle.[8]

Magnetization decay was then measured after a temperature step from 3.5 to 4.0 K. The field cycle was the same, but after stabilizing at 0.3 T at 3.5 K, the tempera-

 0003-6951/91/040415-02$02.00 © 1991 American Institute of Physics

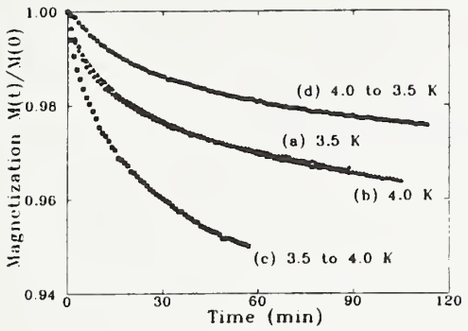

FIG. 1. Decay of magnetization as a function of time measured with a SQUID magnetometer at (a) 3.5 K, (b) 4.0 K, (c) 4.0 K after an increase in temperature from 3.5 K, and (d) 3.5 K after a decrease in temperature from 4.0 K.

ture was increased to 4.0 K. During the temperature stabilization, which took 2 min, the magnetization decayed by about 10%. After temperature stabilization, magnetization versus time was measured using the same routine as before, beginning at $t = 0$. The results are shown as curve (c) in Fig. 1. The decay is 4.8% in 3000 s, $R = 0.014$, significantly greater than for curves (a) and (b). The decay rate was also measured after a *decrease* in temperature from 4.0 to 3.5 K using the same protocol. As expected, the decay rate was less, 1.8% in 3000 s, $R = 0.006$, shown as curve (d). Similar measurements were made for smaller temperature steps. After a 0.1 K increase from 3.9 K, the magnetization decayed by 3.2% in 3000 s, $R = 0.010$. Measurements on samples from other SSC cables showed similar trends.

The enhancement in magnetic relaxation after an increase in temperature may be related to the temperature dependence of the critical current density J_c. Sun *et al.*[9] showed that flux creep in high-temperature superconductors could be reduced by a decrease in temperature. A sample initially in the critical state has magnetic shielding currents equal to the critical current density. Upon decreasing the temperature, J_c increases and the sample is in what we call a subcritical state, with shielding currents less than the critical current density. This reduces flux creep.

We expect that an increase in temperature would increase flux creep. After the magnetic field is cycled, the sample is initially in the critical state. When the sample is warmed, J_c decreases and the sample is in what we call a supercritical state, with shielding currents greater than the critical current density. To restore equilibrium, the shielding currents and associated pinned flux must redistribute, leading to enhanced flux creep. Considering the operating conditions for SSC magnets, we suggest that a temperature increase may contribute to the measured sextupole-field decay with time.

We thank R. M. Scanlan, Lawrence Berkeley Laboratory, for helpful discussions. This work was supported by the U. S. Department of Energy, Division of High Energy Physics.

[1] P. W. Anderson and Y. B. Kim, Rev. Mod. Phys. **36**, 39 (1964).
[2] M. R. Beasley, R. Labusch, and W. W. Webb, Phys. Rev. **181**, 682 (1969).
[3] D. A. Herrup, M. J. Syphers, D. E. Johnson, R. P. Johnson, A. V. Tollestrup, R. W. Hanft, B. C. Brown, M. J. Lamm, M. Kuchnir, and A. D. McInturff, IEEE Trans. Magn. **25**, 1643 (1989).
[4] R. W. Hanft, B. C. Brown, D. A. Herrup, M. J. Lamm, A. D. McInturff, and M. J. Syphers, IEEE Trans. Magn. **25**, 1647 (1989).
[5] M. Kuchnir and A. V. Tollestrup, IEEE Trans. Magn. **25**, 1839 (1989).
[6] W. S. Gilbert, R. F. Althaus, P. J. Barale, R. W. Benjegerdes, M. A. Green, M. I. Green, and R. M. Scanlan, Adv. Cryo. Engr. (Materials) **36**, 223 (1990).
[7] E. W. Collings, A. J. Markworth, K. R. Marken, M. D. Sumption, and R. M. Scanlan, Department of Energy Topical Workshop on Magnetic Effects of Persistent Currents in Superconductors, 5–7 March 1990, Batavia, Illinois.
[8] A. K. Ghosh, Department of Energy Topical Workshop on Magnetic Effects of Persistent Currents in Superconductors, 5–7 March 1990, Batavia, Illinois.
[9] J. Z. Sun, B. Lairson, C. B. Eom, J. Bravman, and T. H. Geballe, Science **247**, 307 (1990); M. R. Beasley, R. Labusch, and W. W. Webb, Phys. Rev. **181**, 682 (1969).
[10] J. R. Clem, Department of Energy Topical Workshop on Magnetic Effects of Persistent Currents in Superconductors, 5–7 March 1990, Batavia, Illinois.
[11] W. S. Gilbert, R. F. Althaus, P. J. Barale, R. W. Benjegerdes, M. A. Green, M. I. Green, and R. M. Scanlan, IEEE Trans. Magn. **25**, 1459 (1989).

Investigation of Possible Causes for the Multipole Drift in Superconducting Dipole Magnets

R. M. Scanlan
Lawrence Berkeley Laboratory
Berkeley, California 94720

R. W. Cross and R. B. Goldfarb
National Institute of Standards and Technology
Boulder, Colorado 80303

Introduction

A time-dependent drift or relaxation of the higher order multipoles has been observed at low fields in many superconducting dipole magnets. These include dipoles used in the Tevatron at Fermi National Accelerator Laboratory (FNAL),[1] the Hadron Electron Ring Accelerator (HERA) at *Deutsches Elektronen-Synchrotron* (DESY),[2] and prototype magnets built for the Superconducting Super Collider (SSC) project.[3] These results were reviewed recently at a workshop,[4] and a number of possible explanations were discussed. Among these is the decay of magnetization due to flux creep.

Although measurements which show flux creep occurring in superconducting wires and cables were presented, the magnitude of the creep was a factor of five or 10 lower than the multipole decay in the dipole magnets. Several mechanisms which may cause an enhanced decay in the environment of the dipole magnets were proposed. W. Fietz (Department of Energy) and C. Taylor (Lawrence Berkeley Laboratory) suggested that the time dependence could arise from the current and flux redistribution which occurs as the cable strands traverse from the edge of the cable in the high field region to the edge in the low field region. Taylor also suggested that current redistribution due to the presence of solder joints could give rise to a time dependent change in the multipoles. More recently, experiments at DESY showed that the magnitude of the multipoles varied along the axis of the HERA dipoles, and the period of this variation is identical to the strand pitch length in the cable.[5] This result suggests that currents of different magnitude are flowing in different strands of the cable. Several mechanisms have been proposed to explain this phenomenon, including nonuniform resistance due to cold welds in the strands. This note describes the results of several experiments which attempt to simulate some of these conditions and to observe the resulting magnetization change as a function of time.

Experiment

A number of techniques have been used to observe the time dependence of the magnetization in superconductors. They include vibrating-sample magnetometry (VSM),[6] superconducting-quantum-interference-device (SQUID) magnetometry,[7] and Hall-probe magnetometry.[8] A Hall-probe magnetometer was chosen for these experiments because we wanted to measure a full cross section SSC cable, 10 mm wide and several centimeters long, and this could not be done with conventional SQUID or VSM equipment. Furthermore, we wanted to make measurements in a field gradient.

The experimental arrangement for the Hall-probe magnetometer has been described in Ref. 8 and is shown in Fig. 1, where the sample is placed in a uniform transverse field. To simulate the condition of the cable in a dipole magnet, the background field was cycled from 0 to 6 T and back to 0, followed by a ramp to a set field, after which the background field was held constant by switching the magnet to persistent mode. A number of studies of magnetization versus time were performed, and the results are in Fig. 2–7. Magnetization as a function of time t was normalized to the value at $t = 0$, defined as the time the magnet was placed into persistent mode.

For the experiments described here, several different configurations were studied. First, the cable was measured in the "standard" configuration illustrated in Fig. 1. The data appear in Fig. 2. Next, the sample ends were extended into the high field gradient region near the top of the solenoid (Figs. 3–6). To examine the influence of solder joints, a sample was prepared with an overlap solder joint. The joint was in a fairly uniform field, but the sample tails extended out of the solenoid and were thus in a field gradient (Fig. 7).

All runs showed basically the same type of behavior, characterized by two different regimes. The first is a fast decay which is associated with eddy currents,[6] and a second, slower decay which is associated with flux creep the superconducting filaments. The decay rates were not affected by the two variables introduced in these experiments: a field gradient along the cable and a solder joint in the cable. No significant change was observed which could help explain the large multipole drift seen in the dipole magnets. The Hall-probe technique appears to be a useful technique for studying large-volume samples such as the Rutherford-type cables used in accelerator dipole magnets.

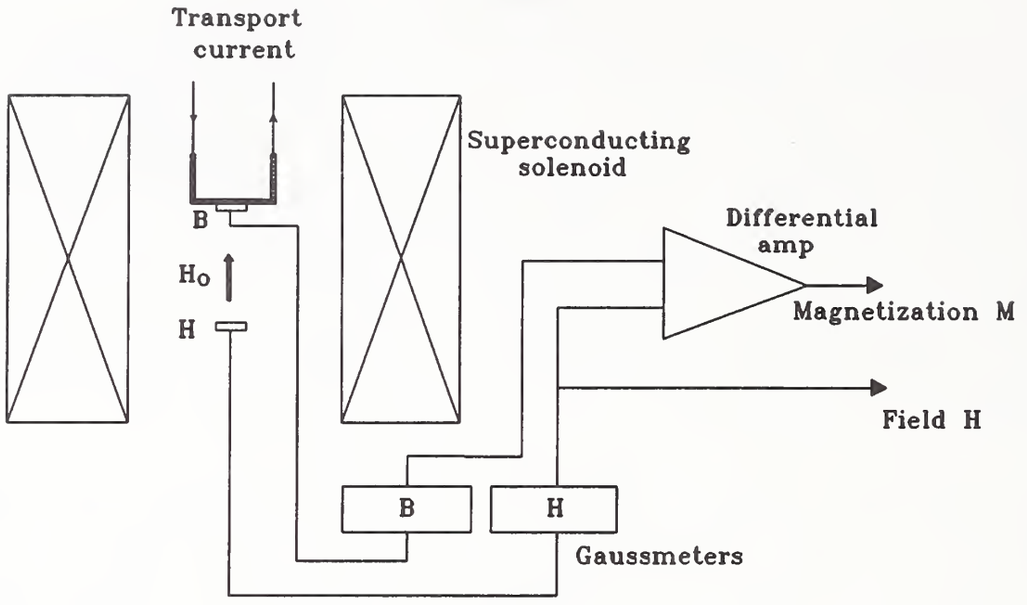

Figure 1. Schematic diagram of the Hall-probe magnetometer. The magnetic field H_0 is supplied by a superconducting solenoid. The sample is bent into a U-shape so that solder contacts can be made away from the Hall sensing area. After Ref. 8.

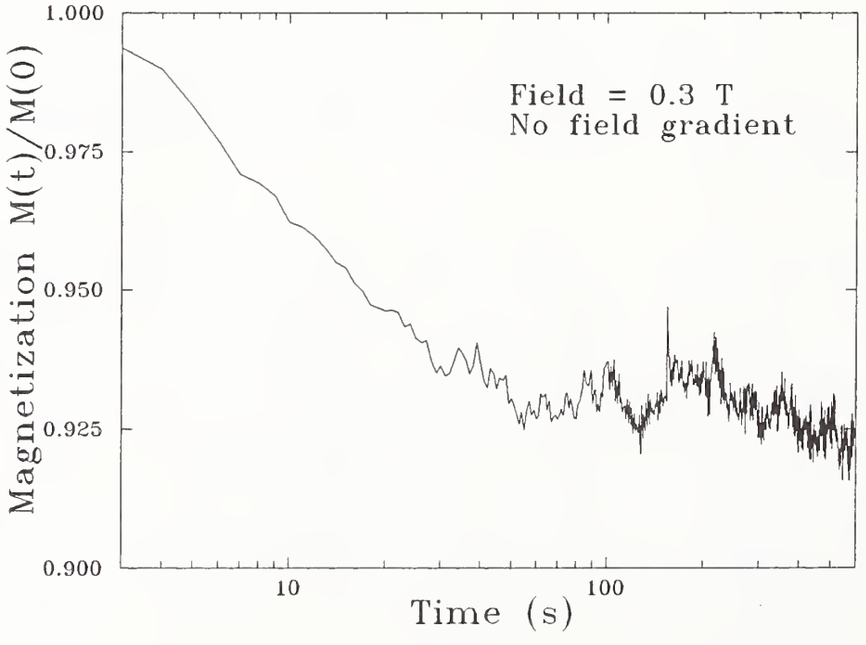

Figure 2. Normalized magnetization as a function of time. Measuring field 0.3 T. Control experiment: sample tails not in a field gradient; no solder joint.

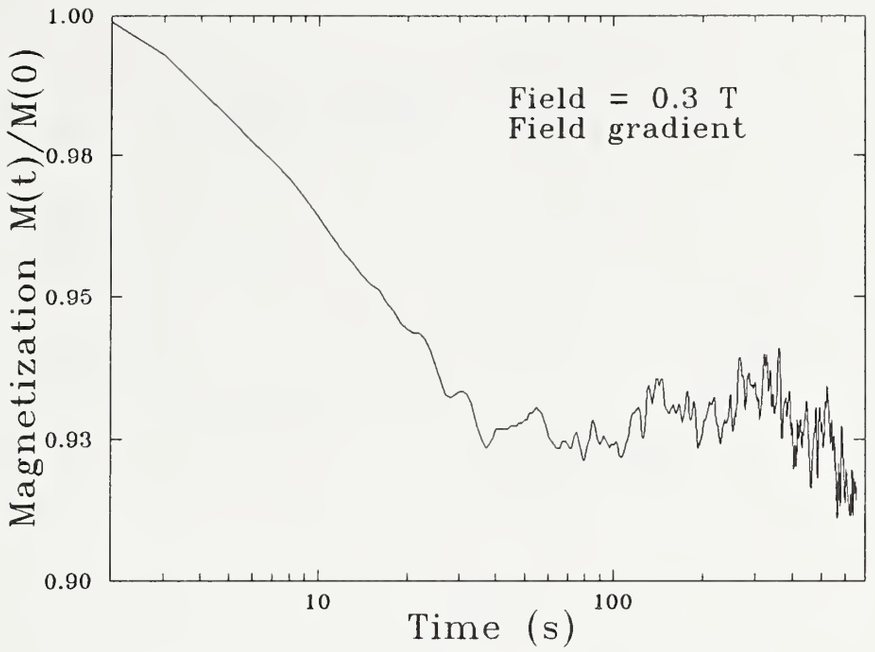

Figure 3. Normalized magnetization as a function of time. Measuring field 0.3 T, same as in Fig. 2. Sample tails extend to region of near-zero field.

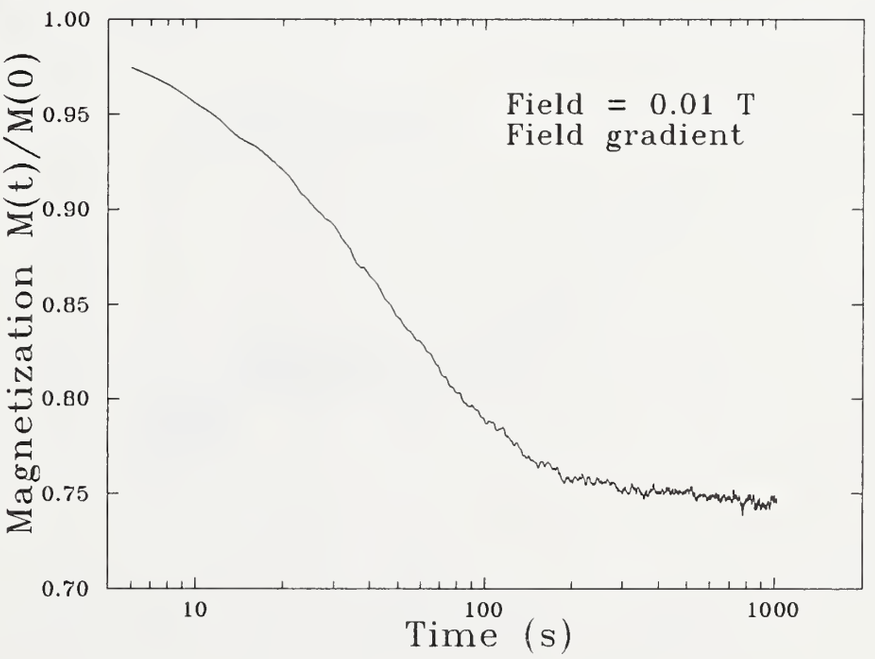

Figure 4. Normalized magnetization as a function of time. Measuring field 0.01 T, much smaller than in Fig. 3. Sample tails extend to region of near-zero field.

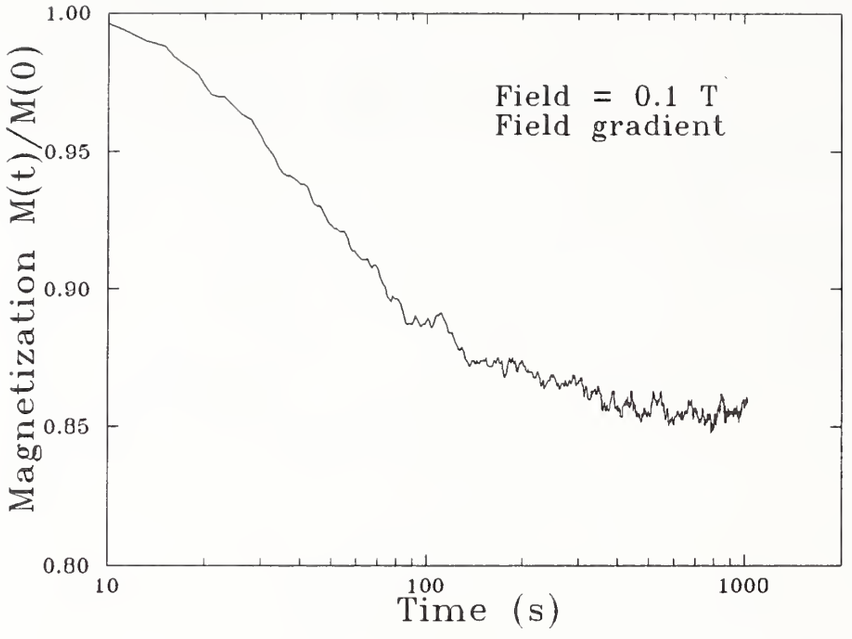

Figure 5. Normalized magnetization as a function of time. Measuring field 0.1 T, somewhat smaller than in Fig. 3. Sample tails extend to region of near-zero field.

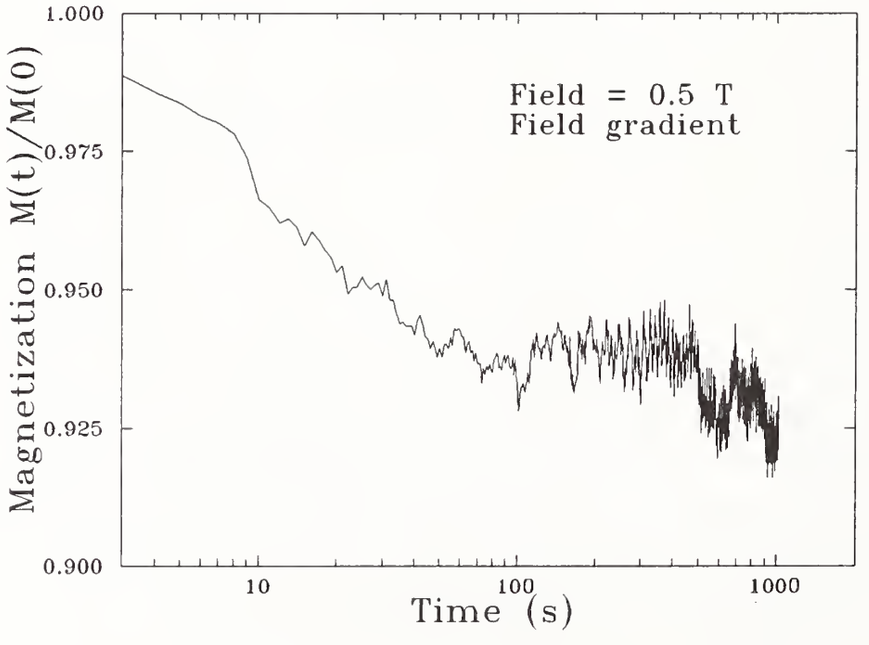

Figure 6. Normalized magnetization as a function of time. Measuring field 0.5 T, somewhat larger than in Fig. 3. Sample tails extend to region of near-zero field.

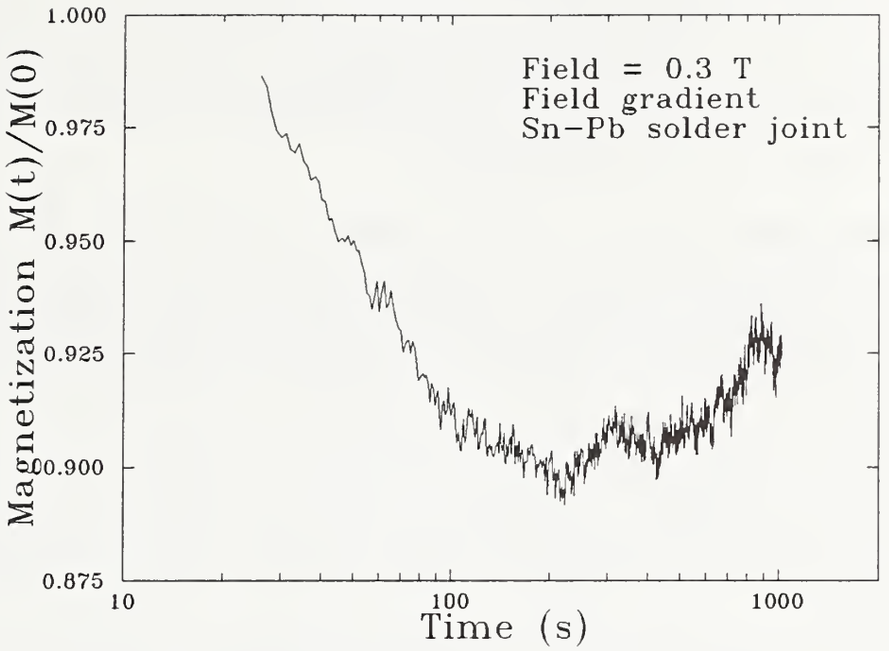

Figure 7. Normalized magnetization as a function of time. Measuring field 0.3 T. Sample tails extend to region of near-zero field, similar to Fig. 3, but sample has Sn-Pb solder joint in a region of fairly uniform field. Magnetization measured on a segment of cable far from the solder joint.

References

1. D. A. Herrup, M. J. Syphers, D. E. Johnson, R. P. Johnson, A. V. Tollestrup, R. W. Hanft, B. C. Brown, M. J. Lamm, M. Kuchnir, and A. D. McInturff, Time variations of fields in superconducting magnets and their effects on accelerators, *IEEE Trans. Magn.* **25**, 1643-1646 (1989).

2. H. Brück, Zhengkuan Jiao, D. Gall, G. Knies, J. Krzywinski, R. Meinke, H. Preissner, and P. Schmüser, Time dependence of persistent current effects in the superconducting HERA magnets, 11th Int. Conf. Magnet Tech. (MT-11), T. Sekiguchi and S. Shimamoto, eds., Elsevier Science, Essex, U.K. (1990), pp. 141-146.

3. W. S. Gilbert, R. F. Althaus, P. J. Barale, R. W. Benjegerdes, M. A. Green, M. I. Green, and R. M. Scanlan, The effect of flux creep on the magnetization field in the SSC dipole magnets, *Adv. Cryo. Eng. (Materials)* **36**, 223-230 (1990).

4. Department of Energy Topical Workshop on Magnetic Effects of Persistent Currents in Superconductors, March 5–7, 1990, Fermi National Accelerator Laboratory, Batavia, Illinois.

5. H. Brück, D. Gall, J. Krzywinski, R. Meinke, H. Preissner, A. Freter, M. Halemeyer, P. Schmüser, R. Stiening, D. ter Avest, and L. J. M. van de Klundert, Observation of a periodic pattern in the persistent-current fields of the superconducting HERA dipole magnets, DESY-HERA Report 91-01 (1991).

6. K. R. Marken, A. J. Markworth, M. D. Sumption, and E. W. Collings, Eddy-current effects in twisted and wound SSC strands, *IEEE Trans. Magn.* **27**, 1791-1795 (1991).

7. T. W. Petersen and R. B. Goldfarb, Effect of mechanical deformation on Nb-Ti filament proximity-effect coupling at the edges of SSC cables, *IEEE Trans. Magn.* **27**, 1809-1810 (1991).

8. R. W. Cross and R. B. Goldfarb, Hall probe magnetometer for SSC magnet cables: Effect of transport current on magnetization and flux creep, *IEEE Trans. Magn.* **27**, 1796-1798 (1991).

Effect of Mechanical Deformation on Nb-Ti Filament Proximity-Effect Coupling at the Edges of SSC Cables

T. W. Petersen and R. B. Goldfarb
Electromagnetic Technology Division
National Institute of Standards and Technology
Boulder, Colorado 80303

Abstract

Magnetization as a function of transverse magnetic field and time was measured for short strands extracted from the centers and edges of five Nb–Ti Rutherford cables designed for use in Superconducting Super Collider dipole magnets. The multifilamentary strands all had 6-μm diameter filaments. Edge samples, which had severe mechanical deformation, showed small magnetic coupling losses at low fields, compared to no coupling losses for undeformed center strands. Sharp strand bends at cable edges decreases the interfilament spacing to the order of the coherence length in the normal matrix material which increases the effective filament diameter and hysteresis loss at low fields. Microscopic studies of the cables' cross sections confirmed smaller interfilament separations in these samples. Flux creep measurements, represented by the time dependence of magnetization, showed little difference between edge and center samples. This indicates that the proximity-coupled matrix in edge samples is not a significant source of flux creep.

Introduction

Superconducting Super Collider (SSC) dipole magnets are required to have highly uniform fields. The magnetization of the magnets' superconducting filaments results in field nonuniformity. This effect is largest at low fields where the magnetization is highest. To reduce the magnetization of superconductor wires, multifilamentary conductors are used. According to the critical state model, for a large transverse field [1], the superconductor magnetization M depends on the filament diameter d and the critical current density J_c: $M = 2 J_c d / (3\pi)$.

Efforts to decrease the size of the filaments have succeeded in producing wires with filament diameters smaller than 1 μm. However, to maintain the critical current of the wire, the distance between adjacent filaments is also decreased with decreasing filament size. Once the separation between the filaments is on the order of the coherence length in the normal matrix material, the filaments become coupled through supercurrents in the matrix [1,2]. This increases the effective filament diameter and, as a result, the magnetization. Uncabled SSC wire shows very little coupling due to the proximity effect. However, recent work has shown a degradation of the cable's current-carrying capacity at the edges, presumably due to mechanical deformations resulting from the cabling process [3,4].

This paper examines the effect of the cabling process on the magnetic properties of SSC cables. Measurements of magnetization as a function of both time and applied field were performed on samples taken from the edges and centers of SSC cables. Filament separation was also studied by microscopic evaluation of the samples.

Contribution of the National Institute of Standards and Technology, not subject to copyright.
Manuscript received September 24, 1990.

Experimental Details

Samples for magnetization as a function of time and applied field were extracted from five different 23-strand Rutherford cables designed for use in SSC dipole magnets. Most samples had a Cu/superconductor volume ratio of 1.36 and keystone angles varying from 1.6 to 3.0 degrees. A cable was fixed in epoxy to prevent movement of the strands while a 4-mm section was cut with a diamond saw. The epoxy was removed from the sample and strand segments were extracted from the centers and the edges. Strand samples were weighed and the total volume of Nb–Ti was calculated from the mass of the strand, the densities of Cu and the Nb–Ti, and the Cu/superconductor ratio. Some specimens were cast in epoxy and polished prior to microscopic studies.

Measurements of magnetization per unit volume of Nb–Ti were made at 5 K using a SQUID magnetometer with the applied field perpendicular to the axis of the strand. Magnetization as a function of applied field was carried out for maximum fields of 2 T (1.6 MA/m). A magnetometer scan length of 4 cm was used with a field variation of 0.19%. Flux creep measurements, represented by the time dependence of the magnetization, were made after a field cycle of 0 to 2 T to 25 mT. This field cycle was chosen to maximize the proximity coupling between filaments. An external field of 25 mT corresponds to zero internal field for a demagnetizing factor of 0.5. A scan length of 2 cm was used with a field variation of less than 0.01%. Due to the finite time required to perform a magnetization measurement, it was impossible to monitor the decay of the magnetization that occurred in the first 2 min following the field change.

Results and Discussion

The magnetization of samples taken from the edges of the cables show small coupling peaks centered around zero field, whereas data for samples taken from the center of the cables show no such losses. These results are represented in Fig. 1. The results shown are representative of the five cables studied. In each case, the edge sample showed hysteresis losses not observed in the center sample. These losses are characteristic of proximity-effect coupling [2]. This suggests that the separation between some of the filaments in the edge samples is on the order of the coherence length in the Cu matrix. We attribute the change in the filament separation to mechanical deformation resulting from the cabling process.

Following the derivation of Collings [5], we estimate the coherence length in the matrix material to range between 0.21 and 0.36 μm for the samples studied. Therefore, to avoid coupling of the filaments at zero field, the spacing should be about 0.7 μm or greater. Microscopic studies of the cables' cross sections showed spacings between the filaments of approximately 1 μm for undeformed center strands. In edge samples, however, we observed smaller interfilamentary spacing, approximately 0.2 μm, for filaments in the deformed regions of the strand.

U.S. Government work not protected by U.S. Copyright.

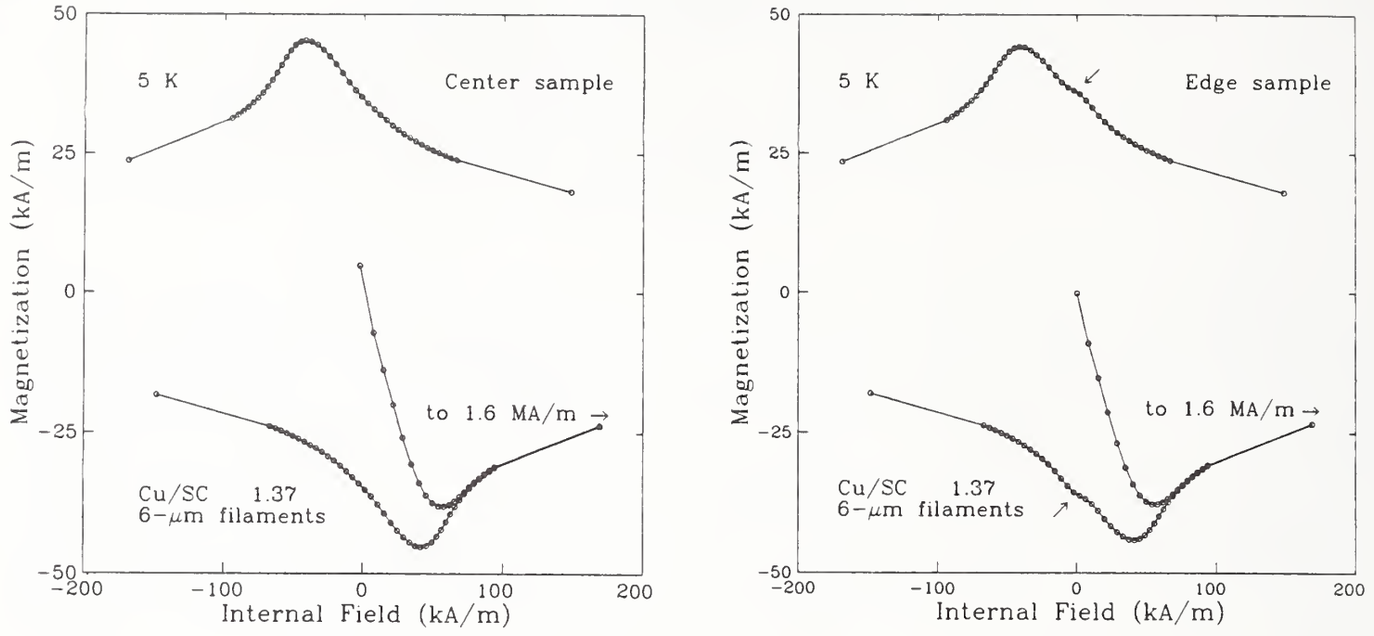

Figure 1. Magnetization as a function of internal field (corrected for demagnetizing factor) for center and edge samples. The left graph shows the low field magnetization for a center strand of SSC cable. The right graph shows an edge strand from the same cable. Note the small coupling peaks (arrows) for the edge sample near zero internal field.

Measurements of magnetization as a function of time were carried out for the two types of samples. The decay of the magnetization in the edge samples showed no appreciable difference from the center samples as can be seen in Fig. 2. The results shown are representative of the five samples measured. Additional measurements made at higher fields also did not show differences between samples. Despite the fact that some sections of magnet cable are located in regions of small field, flux creep in the proximity-coupled matrix is probably not a source of the field decay seen in SSC dipole magnets for the following reasons. (1) The fraction of proximity-coupled filaments in a cable, and the associated coupling peak in the hysteresis loop, is small. (2) The rate of decay of magnetization is the same for coupled and uncoupled samples. (3) The time constant of the magnetization decay observed in these samples is short (15–18 min) compared to the decay observed in accelerator magnets (1–2 h) [6–9].

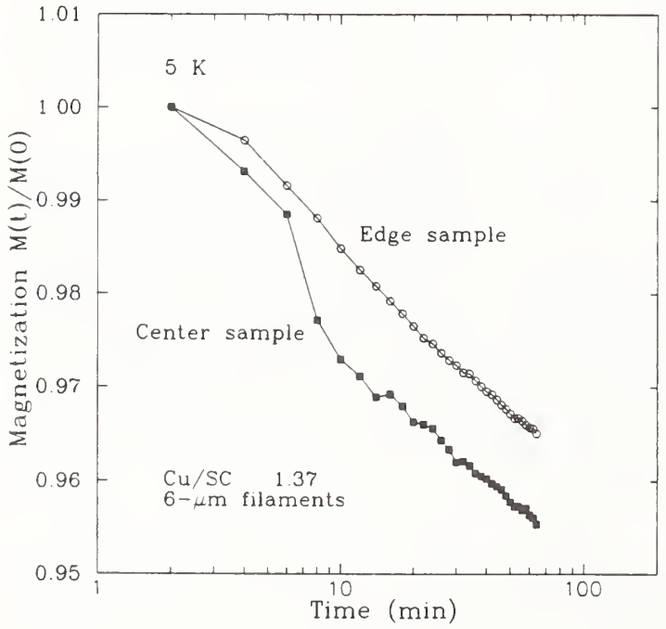

Figure 2. Normalized magnetization as a function of time for a field cycle of 0 to 2 T to 25 mT. After this field cycle the internal field is near zero, which allows proximity coupling between filaments.

Acknowledgment

This work was supported by the U.S. Department of Energy, Division of High Energy Physics.

References

[1] W. J. Carr, Jr., J. H. Murphy, and G. R. Wagner, *Adv. Cryo. Engr.* **24**, 415 (1978).
[2] V. R. Karasik, N. G. Vasil'ev, and V. G. Ershov, *Zh. Eksp. Teor. Fiz.* **59**, 790 (1970) [Sov. Phys. JETP **32**, 433 (1971)].
[3] L. F. Goodrich, S. E. Pittman, J. W. Ekin, and R. M. Scanlan, *IEEE Trans. Magn.* **23**, 1642 (1987).
[4] L. F. Goodrich and S. L. Bray, *IEEE Trans. Magn.* **25**, 1949 (1989).
[5] E. W. Collings, *Adv. Cryo. Engr. (Materials)* **34**, 867 (1987).
[6] D. A. Herrup, M. J. Syphers, D. E. Johnson, R. P. Johnson, A. V. Tollestrup, R. W. Hanft, B. C. Brown, M. J. Lamm, M. Kuchnir, and A. D. McInturff, *IEEE Trans. Magn.* **25**, 1643 (1989).
[7] R. W. Hanft, B. C. Brown, D. A. Herrup, M. J. Lamm, A. D. McInturff, and M. J. Syphers, *IEEE Trans. Magn.* **25**, 1647 (1989).
[8] M. Kuchnir and A. V. Tollestrup, *IEEE Trans. Magn.* **25**, 1839 (1989).
[9] W. S. Gilbert, R. F. Althaus, P. J. Barale, R. W. Benjegerdes, M. A. Green, M. I. Green, and R. M. Scanlan, *Adv. Cryo. Engr. (Materials)* **36**, 223 (1990).

AC LOSS MEASUREMENTS OF TWO MULTIFILAMENTARY NbTi COMPOSITE STRANDS

E. W. Collings*, K. R. Marken, Jr.*, M. D. Sumption*†,
R. B. Goldfarb**, and R. J. Loughran**

* Battelle Memorial Institute, Columbus, OH 43201
† Permanent address: Ohio University, Athens, OH 45701
** National Institute of Standards and Technology, Boulder, CO 80303

ABSTRACT

As part of an interlaboratory comparative testing program conducted in support of the Versailles Agreement on Advanced Materials and Standards (VAMAS), transverse-field DC hysteresis loss measurements were made at liquid-helium temperatures at fields of up to 3 T (30 kG) on two samples of multifilamentary NbTi composite. The strands differed widely in filament number, were comparable in filament diameter, and one of them was provided with a Cu-Ni barrier between the filaments. The results have been analyzed, and magnetically deduced critical current density values obtained (for comparison with directly measured transport data) using various standard techniques. Based on these studies, a figure-of-merit for AC loss is recommended. The Cu-matrix strand, with its interfilamentary spacing of less than 1 μm, exhibited pronounced proximity-effect-induced coupling losses; this was not observed in the mixed-matrix strand which possessed not only a Cu-Ni barrier but also an interfilamentary spacing of typically 4 μm.

INTRODUCTION

In support of the Versailles Agreement on Advanced Materials and Standards (VAMAS), DC hysteresis loss measurements were made at liquid-helium temperatures in transverse magnetic fields of up to 3 T (30 kG) on samples prepared from two types of multifilamentary NbTi composite superconductors. The strands, designated herein as Sample E (henceforth SL-E) and Sample D (henceforth SL-D), had been manufactured in Japan and in the U.S.A., respectively. SL-E is a "mixed-matrix" strand in which the filaments are surrounded first by Cu and then by a thin (15 μm) eddy-current barrier of Cu-Ni alloy. SL-D consists of closely spaced NbTi filaments separated only by Cu. Photomicrographs of the strands are presented in Figs. 1 and 2. Noticeable in the magnified cross sections are the irregular shapes of the filaments, particularly in SL-E. For this reason, accurate filament cross-sectional areas (for the purpose of J_c calculation from the results of I_c measurement) could only be obtained by an etching-and-weighing procedure. Some specifications of the strands are listed in Table 1.

HYSTERESIS-LOSS MEASUREMENT

Measurements were made at Battelle, Columbus Division (BCD) and the National Institute of Standards and Technology (NIST) using vibrating-sample magnetometry. At both places the instruments were calibrated against pure Ni standards. At BCD,

Advances in Cryogenic Engineering (Materials), Vol. 36
Edited by R. P. Reed and F. R. Fickett
Plenum Press, New York, 1990

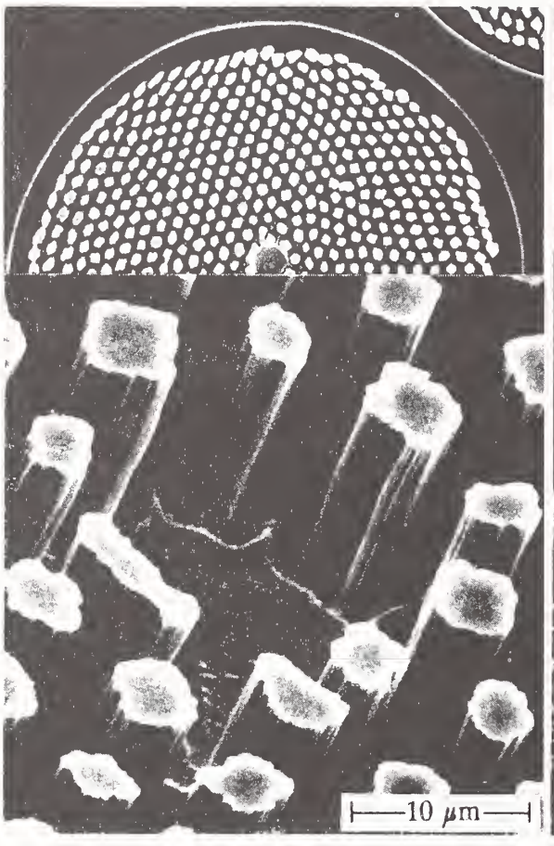

Fig. 1. Scanning electron micrograph of Sample E (SL-E).

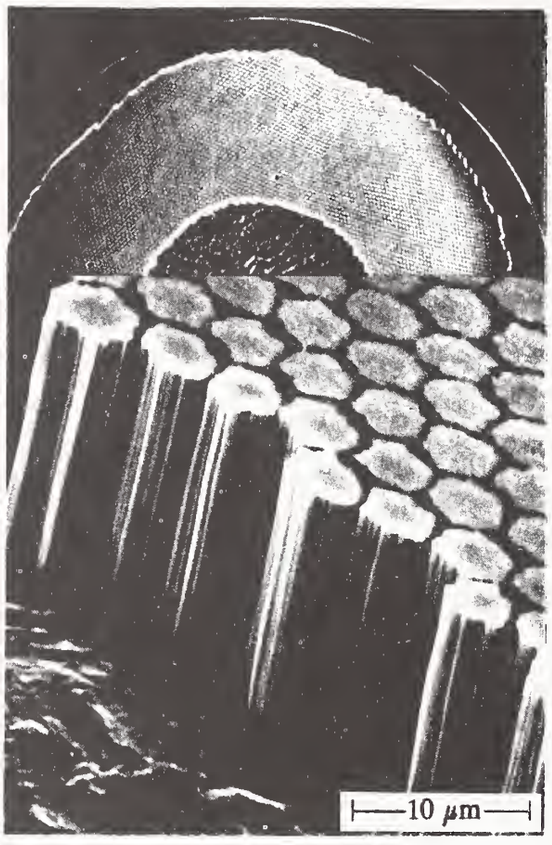

Fig. 2. Scanning electron micrograph of Sample D (SL-D).

magnetization was measured in the slowly swept field (amplitudes 0.1 to 1.6 T; sweep rates 1.7 to 28 mT/s) of an iron-core electromagnet; data were recorded automatically at a field resolution of about $1/200^{th}$ of the field-sweep amplitude. At NIST, point-by-point measurements were taken in stepped fields (up to 3 T) provided by a superconducting solenoid. The typical BCD sample consisted of an epoxy-potted 3-mm-diameter bundle of 6-mm-long pieces of strand. The typical NIST sample was formed by winding a strand or group of strands along the thread of a 5-mm-diameter nylon screw.

Table 1. Specifications of Strands under Investigation

Sample Code	Sample E (SL-E)	Sample D (SL-D)
Type	Mixed matrix	Copper matrix
Configuration	NbTi/Cu/CuNi	NbTi/Cu
Volume Ratio	21.5/44.1/34.4	42.0/58.0
Twist pitch, mm	6	13
Strand diameter, D, mm	0.35	0.742
Fil. diameter*, w, μm	5.79	4.62
Number of filaments	760	10,980
I_c at 3 tesla, A	50	675 **
J_c*** at 3 tesla, $10^5 A/cm^2$	2.50	3.67

* Measured by the etching-and-weighing technique on 304-cm (SL-E) and 149-cm (SL-D) lengths of strand. Measured density of bulk Nb-46.5Ti = 6.097 g/cm^3.
** Straight-sample measurement at NIST (manufacturer's supplied value, 653 A).
*** Based on I_c and the above-measured NbTi cross-sectional area.

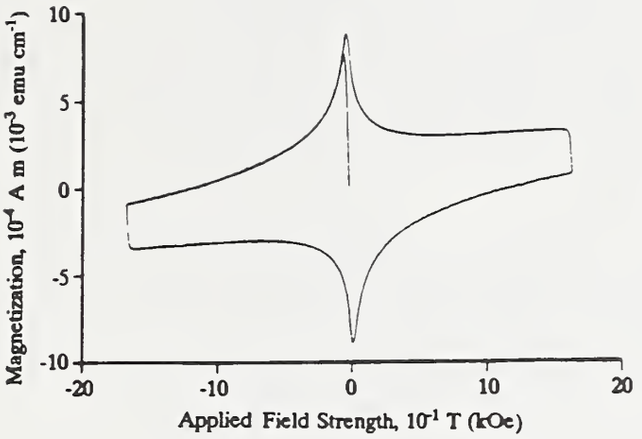

Fig. 3. Magnetization per unit length of strand at 4.2 K for SL-E -- typical BCD data.

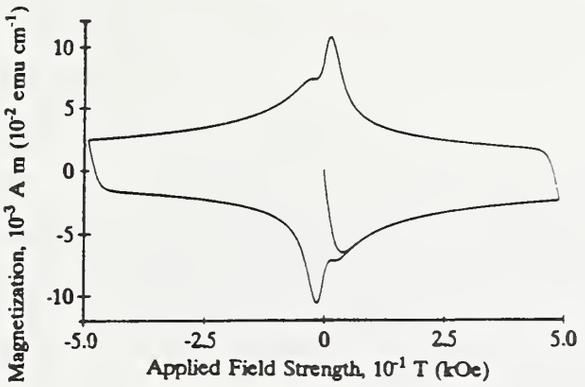

Fig. 4. Magnetization per unit length of strand at 4.2 K for SL-D -- typical BCD data.

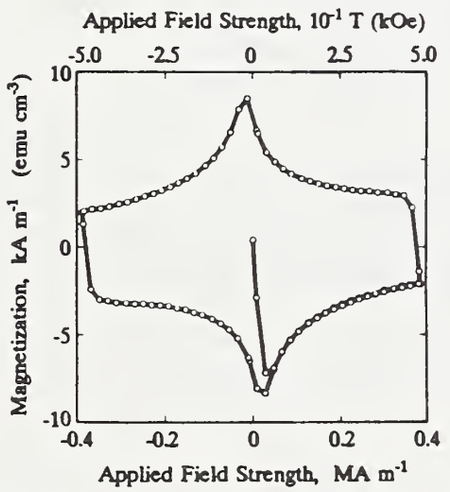

Fig. 5. Magnetization per unit volume of strand at 4 K for SL-E -- typical NIST data.

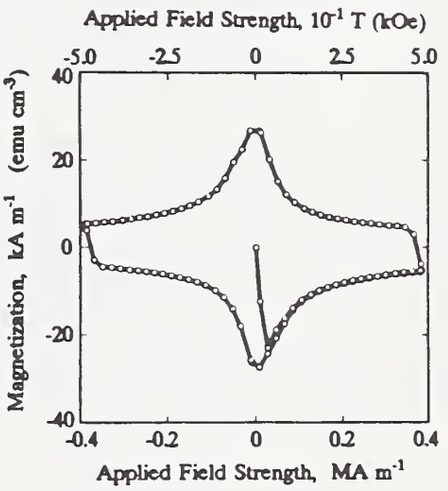

Fig. 6. Magnetization per unit volume of strand at 4 K for SL-D -- typical NIST data.

RESULTS AND DISCUSSION

Some typical hysteresis loops are presented in Figs. 3 to 6. Two features are noteworthy: (1) Fig. 3 (in which a large field-sweep amplitude has been deliberately selected) exhibits a pronounced paramagnetic slope due to the presence of the CuNi barrier material of which 34.4 vol.% is present; (2) Fig. 4 exhibits a shoulder and a peak near the origin, structure which is not resolved in Fig. 6. The shoulder is due to the NbTi filament magnetization while the sharp peak, which also dominates Fig. 6, results from coupling currents flowing in the Cu matrix (cf. Ref. 1). Coupling is not present in SL-E with its larger filament separation and resistive barrier layer.

The results of AC-loss measurements can be represented in several ways. A direct approach, and one which is useful from an applications standpoint, is to tabulate or plot the energy loss per cycle per unit length of wire, Q_ℓ, as function of the field-sweep amplitude, H_m. This is done in Fig. 7. According to the figure, there is good general agreement between the BCD and NIST data over the entire field-amplitude range, in spite of the fact that the two sets of measurements were made on samples differing widely in configuration. Furthermore, when measurements were made in both laboratories on the BCD samples, the results differed by less than 7% *.

AC-LOSS REPRESENTATIONS AND FIGURES OF MERIT

Representations of AC Loss

Depending on the purpose in mind, various "levels" of refinement can be adopted in reporting and comparing of AC-loss information. In general, the hysteretic loss of a multifilamentary strand per unit volume of superconductor per unit field-sweep amplitude may be regarded as a function, $Q(J_c, w, P, A)$, of: (i) the critical current density, J_c, of the superconductor, (ii) the diameter, w, of the filaments, (iii) P, the influence of proximity-effect coupling between the filaments, and (iv) an "addenda", A, which includes the effect of imponderables such as filament-cross-section irregularity.

Level-0. The simplest representational level, referred to here as Level-0, is Q_ℓ (Fig. 7) which derives directly from hysteresis-loss measurements on a known length, ℓ, of strand. At this level the various possible contributions to loss remain unspecified. According to Fig. 7, under the Level-0 criterion SL-D is the more lossy -- but it also possesses more filaments than SL-E and is able to carry, for this and other reasons, a larger critical current.

Level-1. A more significant indicator of hysteretic loss, especially from an engineering standpoint with a particular application in mind, would be to normalize Q_ℓ to the I_c of the strand (taken, perhaps, at some operating field of interest). In this next level of refinement hysteretic loss, gauged by Q_ℓ/I_c, responds only to differences in w and A.

Level-2. Finally, under Level-2 (to be discussed below), differences in w would also be absorbed, and the resulting criterion would be positioned to emphasise loss due to proximity-effect coupling and the addenda.

---

* At H_m = 0.97 T, the per-cycle hysteresis loss in SL-E as measured at NIST was 6.7% lower than the BCD-measured value; also at H_m = 0.97 T, the NIST-reported loss in SL-D was 1.4% higher than the BDC value.

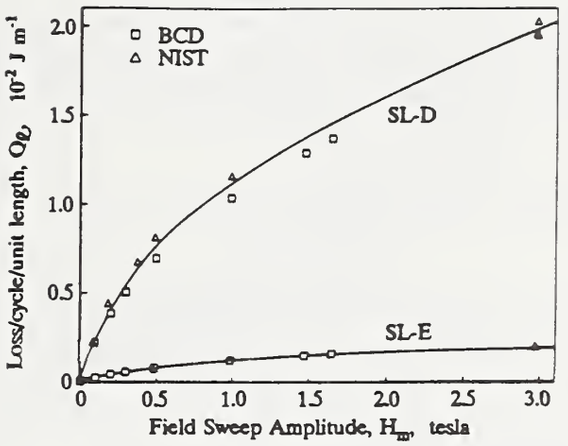

Fig. 7. The Level-0 criterion (loss per cycle per unit length of strand) applied to Sample D (SL-D) and Sample E (SL-E).

Figures of Merit for Hysteretic Loss

The Q_v/J_c (Level-1) Approach. Following the well-known critical-state model[2] as applied by Carr and co-authors (whose work is summarized in Ref. 3) to a multifilamentary composite strand in a transverse applied field, the hysteresis loss per unit volume of the superconducting component of the strand, Q_v, is given in SI units by:

$$Q_v = (8/3\pi)\, w\, J_c\, \mu_0\, H_m$$
$$(\text{or } Q_v = (0.8/3\pi)\, w\, J_c\, H_m, \text{ in practical units}) \qquad (1)$$

$$\text{i.e., } R_Q = Q_v/J_c = (8/3\pi)\, w\, \mu_0\, H_m$$
$$(\text{or } R_Q = Q_v/J_c = (0.8/3\pi)\, w\, H_m, \text{ in practical units}) \qquad (2)$$

It follows that a plot of R_Q versus H_m should, under the Bean approximation, be linear with slope proportional to w, the filament diameter. Departure of R_Q from its expected value, possibly as a result of proximity-effect coupling between the filaments, could then be expressed in terms of some effective filament diameter[4], w_{eff}. Within this framework, the following figures-of-merit (FOM) might be selected: (i) at a given H_m, the ratio w_{eff}/w; (ii) at a given H_m and H, the quotient $R_Q = Q_v/J_c(H)$. The use of $J_c(H)$ recognises that in practice J_c is not independent of field, and that for the purpose of a criterion may have to be measured at some field different from H_m. Finally, we note that in obtaining an experimental value of R_Q, it is convenient to replace Q_v/J_c by its identical equivalent, Q_ℓ/I_c, the latter being a ratio of directly measured quantities, Fig. 8.

For a pair of "ideal" multifilamentary strands, say A and B, the quotient $R_{Q,A}/R_{Q,B}$ at a given H_m should be simply w_A/w_B, the filament-diameter ratio. In the case of the present strands, direct measurements have shown that $w_E/w_D = 1.25$ (see Table 1 and its footnote *). At $H_m = 3$ tesla, this may be compared to the magnetically obtained value of $R_{Q,E}/R_{Q,D} = 1.35$. The interfilamentary coupling present in SL-D (see Fig. 4) should cause $R_{Q,E}/R_{Q,D}$ to be less than the filament-diameter ratio. That it is not, suggests that factors not yet taken into consideration are masking the ability of the R_Q criterion to properly represent the presence of coupling. One such factor could well be a difference between the field-dependences of J_c for the two strands.

The $Q_v/\Delta M_v$ (Level-2) Approach. According to the critical-state model for a cylinder of diameter w in a transverse applied field, the total height, $\Delta M_v(H)$, of the NbTi-volume-normalized hysteresis loop (measured between the shielding and trapping branches) at some field H is related to $J_c(H)$, in SI units, by[5]:

$$\Delta M_v(H) = (4/3\pi)\, J_c\, w$$
$$(\text{or } \Delta M_v(H) = (0.4/3\pi)\, J_c\, w, \text{ in practical units}) \qquad (3)$$

Bean's model was of course based on the premise that J_c was independent of field; nevertheless, even Bean[2] and many others to follow, employed Eqn. (3) to determine the field-dependence of J_c, as for example in Fig. 9. A more rigorous treatment of the critical state would be to introduce a field-dependent J_c at the outset -- as in the work of Ohmer and Heinrich[6], who constructed a critical state model (for cylinders in the field-parallel orientation) based on a modified Kim[7] equation.

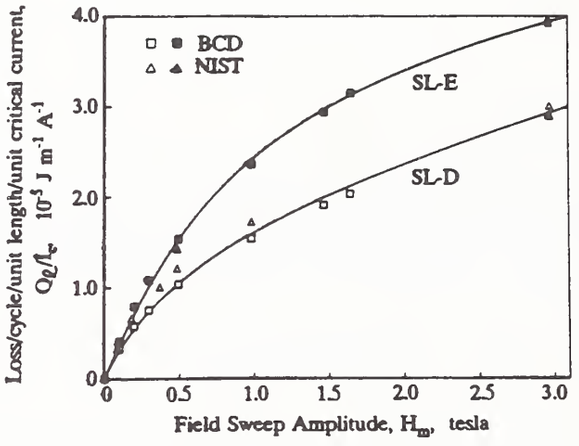

Fig. 8. The Level-1 criterion (loss per cycle per unit length per unit critical current at reference field) applied to SL-D and SL-E.

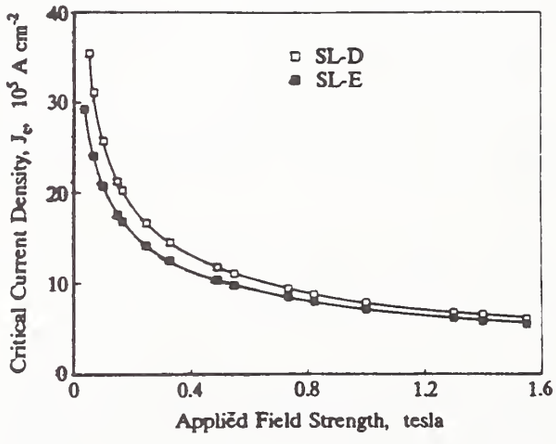

Fig. 9. Magnetization-determined J_c versus applied field strength for SL-E and SL-D.

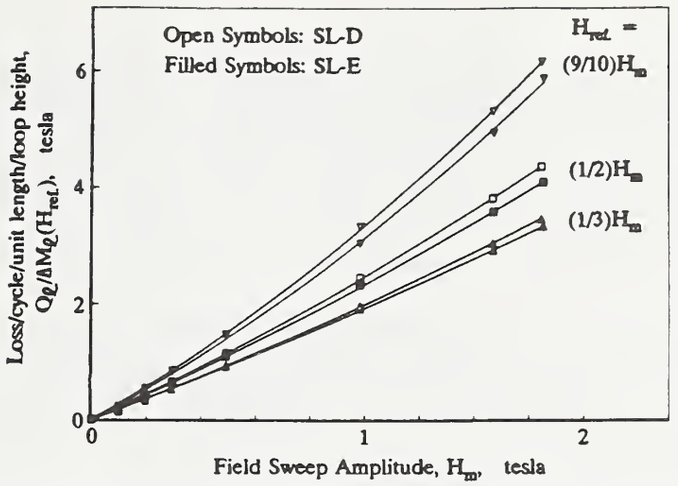

Fig. 10. The Level-2 criterion as function of M(H)-loop amplitude, H_m.

The proportionality between $\Delta M_v(H)$ and $J_c(H)$ provides an opportunity to convert R_Q into a quotient that can be derived solely from the hysteresis loop, without recourse to a separate J_c measurement. From Eqns. (1) and (3), and referring to either unit-volume or unit-length quantities, respectively:

$$R_M = Q_v/\Delta M_v(H) = Q_\ell/\Delta M_\ell(H) = 2\,\mu_0\,H_m$$
$$(\text{or } R_M = Q_v/\Delta M_v(H) = Q_\ell/\Delta M_\ell(H) = 2H_m, \text{ in practical units}) \qquad (4)$$

Under a strict Bean criterion (J_c = const.), ΔM is independent of H and R_M is linear with slope 2.0. Fig. 10 indicates the extent to which this is obeyed in practice. In formulating R_M as a new FOM it will be necessary to normalize Q_ℓ to a loop height measured at some arbitrarily selected reference field, $H_{ref.}$. In Fig. 10, R_M is plotted versus H_m for three values of $H_{ref.}$: (1/3)H_m, (1/2)H_m, and (9/10)H_m, respectively. An important advantage of R_M as an FOM lies in its independence of both J_c (as in the Level-0 criterion) and w (Level-1). Thus, R_M is expected to respond directly to the influence of proximity-effect coupling. Indeed, in Fig. 10, the curves for SL-D (which is coupled) all lie above their SL-E counterparts.

SUMMARY AND CONCLUSION

The hysteretic loss of two multifilamentary strands has been measured by vibrating-sample magnetometry. The results emphasize the importance of acquiring high-resolution data at low fields where J_c, and hence, the hysteresis-loop-height and the loss per unit field increment is greatest. Furthermore, if interfilamentary proximity-effect is present, high-resolution data are useful for resolving the coupling peak and its nearby NbTi shoulder.

Several representations of AC-loss criteria have been suggested. The simplest is Q_v or Q_ℓ (Level-0), which leaves unspecified all possible contributions to loss and which derives directly from hysteresis measurements on known amounts of superconductor. The next level of refinement takes current-carrying capacity into account, resulting in a criterion that responds to filament diameter and what might be termed "high-order" hysteretic losses such as those due to proximity-effect coupling, and perhaps filament-shape distortions and other "addenda". The final level of refinement yields a criterion that includes both I_c and w, and which emphasizes proximity-effect coupling and the addenda.

The criterion $R_Q = Q_\ell/I_c = Q_v/J_c$ (Level-1), normalizes hysteretic loss to current-carrying capacity and is thus useful from a design standpoint. Since filament diameter, w, is not absorbed into the criterion, the strand with the largest w (for given I_c) will have the largest R_Q. Next, the presence of an interfilamentary-coupling contribution to AC loss could be identified directly by introducing the concept of an effective filament diameter[4], $w_{eff} = R_Q/(8/3\pi)H_m$ (in SI units, see Eqn. (2)); the corresponding FOM (a quantity intended to increase beyond 1 in proportion to increased coupling loss) would be w_{eff}/w.

Finally, a Level-2 form of FOM that includes both J_c and w has been suggested; it is $Q_\ell/\Delta M_\ell$ (see Eqn. (4)). Under a strict Bean criterion, in which J_c is assumed independent of H, ΔM_ℓ is constant and equal to $\Delta M_\ell(H_m)$; a dimensionless $Q_\ell/[\Delta M_\ell(H_m).H_m]$ is then equal to 2.0 (see Fig. 10). But in practice J_c and hence ΔM_ℓ, decreases with H. Consequently $Q_\ell/[\Delta M_\ell(H).H_m]$ becomes equal to 2 only when ΔM_ℓ is measured at some intermediate value ($H < H_m$) of the applied field. An advantage of the Q/ΔM quotient is that it can be obtained entirely by magnetometry, ΔM_ℓ substituting for an auxiliary J_c determination. Another advantage of this approach lies in the fact (indicated in the first paragraph of this discussion) that the largest contribution to incremental hysteretic loss occurs at low fields, a region in which J_c may be out of the range of the current-transport measuring equipment.

In conclusion it is important to recognize, as a comparison of Figs. 8 and 10 indicates, the more inclusive the AC-loss criterion or FOM, the smaller is its variation from sample to sample. In general, when defining an FOM, normalization should be carried only far enough to achieve some specific objective, be it engineering or scientific in nature.

ACKNOWLEDGEMENTS

At BCD, the epoxy-potted magnetization samples were prepared by R. D. Smith. At NIST, L. F. Goodrich measured transport critical currents on SL-D, and R. L. Spomer assisted with acquiring the magnetization data. The research was sponsored by the U.S. Department of Energy, Division of High-Energy Physics.

REFERENCES

1. E. W. Collings, K. R. Marken Jr., M. D. Sumption, E. Gregory, and T. S. Kreilick, "Magnetic studies of proximity-effect coupling in a very closely spaced fine-filament NbTi/CuMn composite superconductor", paper in this conference.

2. C. P. Bean, "Magnetization of high-field superconductors", Rev. Mod. Phys. 36, 31-39 (1964).

3. E. W. Collings, Applied Superconductivity, Metallurgy, and Physics of Titanium Alloys, Vol. 1, Plenum Press, New York, 1988, p. 353.

4. S. S. Shen, "Magnetic properties of multifilamentary Nb_3Sn composites", in Filamentary A15 Superconductors, ed. by M. Suenaga and A. F. Clark, Plenum Press, New York, 1980, pp. 309-320.

5. W. J. Carr, Jr., and G. R. Wagner, "Hysteresis in a fine filament NbTi composite", Adv. Cryo. Eng. 30, 923-930 (1984).

6. M. C. Ohmer and J. P. Heinrich, "Magnetization of hysteretic superconductors for complete field penetration and critical state model with $J_c(H) = a/H$", J. Appl. Phys. 44, 1804-1809 (1973).

7. Y. B. Kim, C. F. Hempstead, and A. R. Strnad, "Magnetization and critical super-currents", Phys. Rev. 129, 528-535 (1963).

Effect of Cable and Strand Twist-Pitch Coincidence on the Critical Current of Flat, Coreless Superconductor Cables

J. W. Ekin
Electromagnetic Technology Division
National Institute of Standards and Technology
Boulder, Colorado 80303

Abstract

Data are presented which indicate that a very simple technique for enhancing the critical current in flat, coreless superconductor cables is to match the cable twist pitch with the strand twist pitch. In this manner the same group of filaments within each strand is degraded at each successive bend at the cable edges. This coincident twist method minimizes current transfer among filaments, enhances the slope of the voltage-current characteristic, consistently improves the critical current by about 10% in these tests, and is easy to apply.

Introduction

This paper presents a very simple method to enhance the transport critical current density J_c in flat, coreless superconductor cables, such as the "Rutherford" cables utilized in construction of Superconducting Super Collider (SSC) accelerator magnets. The technique recognizes and compensates for the fact that the superconductor filaments within each strand are periodically degraded where the strands are bent at the cable edges,[1,2] (see Fig. 1). The degradation in J_c is not uniform across the strand where it is bent, but affects the filaments on the outside of the bend (where the tensile strain is greatest) significantly more than the filaments on the inside of the bend.

When the degraded filaments within a strand at one bend do not match up with the *same* degraded filaments at the next bend, current transfer across the strand matrix material is required to redistribute the current among the filaments and optimize the total current that can be carried by the strand. This produces voltages within the strand as the current redistributes across the normal matrix material, degrading the overall critical current of the cable (especially when measured at sensitive electric-field detection levels).[3]

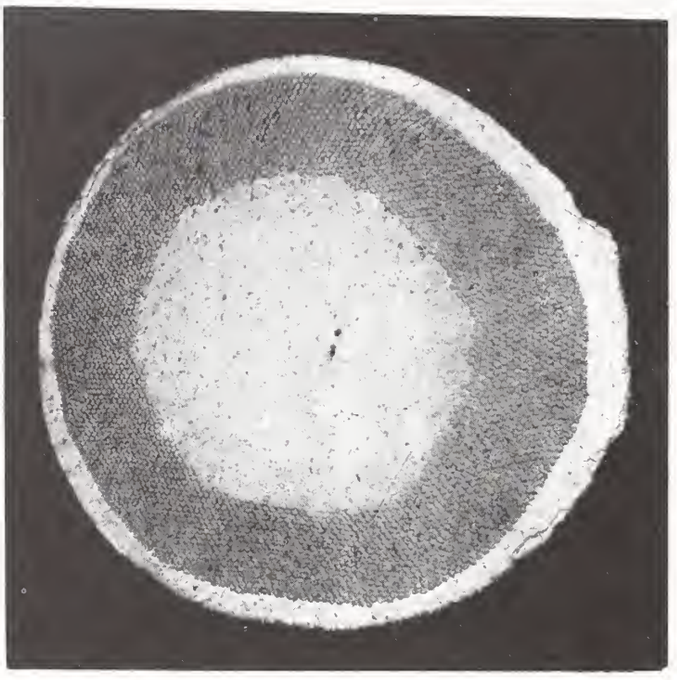

125 X

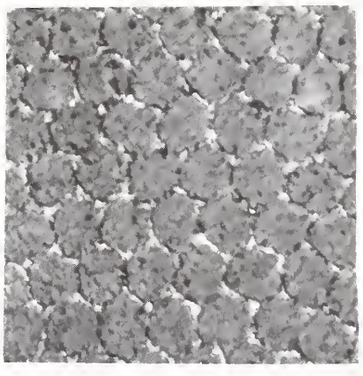

Filaments on
Outside of Bend
1250 X

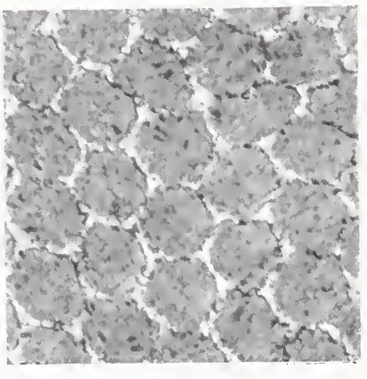

Filaments on
Inside of Bend
1250 X

Figure 1. Cross-sectional view of a bent NbTi strand, showing greater filament area reduction for the filaments on the outside of the bend (left side of the figure), than on the inside of the bend (right side of the figure).

This situation presents the opportunity for a conceptually very simple method to minimize the bend degradation in flat, coreless cables. The technique is to *match the cable twist pitch with the strand twist pitch such that the same group of filaments within each strand are degraded at each successive bend* (see Fig. 2). In this way current transfer among the filaments within the strand is minimized, current-transfer voltages are minimized and the J_c is not degraded as much by the edge bending. The technique only requires that the cabling twist pitch coincides with an *integer* multiple of the strand twist pitch.

Experiment

To test this technique, we studied a series of NbTi strands that are candidate superconductors for the construction of the SSC dipole magnets (0.65 mm diameter, filament twist pitch of 1.27 cm). The conductors were wound on flattened mandrels in such a manner that the spacing between bends at the mandrel edges occurred at either integer or half integer multiples of the strand twist pitch (see Fig. 2). The thickness of the mandrel and the finite length of strand wrapped around the mandrel edge were taken into account in calculating the width of the mandrel needed to match cable and twist pitches. That is, as shown in Fig. 2, we desired that the total edge-to-edge length of the strand's neutral axis, L, to be an integer or half integer of strand twist pitches, S. As seen in Fig. 2, this is just:

$$L = w + (\pi/2)(t + D) = R\,S\,, \tag{1}$$

where w is the mandrel width, t is the mandrel thickness, D is the strand diameter, and R is the cable/strand pitch ratio. R was set to either an integer or half integer value by varying the mandrel width, w.

The sample/mandrel assembly was then placed in the bore of a high-field solenoidal magnet such that the winding axis of the sample was concentric with the central axis of the bore of the test magnet. The voltage taps were counterwound along the superconductor in order to minimize the loop area for inductive pickup in the high field test magnet. The samples were held in place with varnish, which in most cases was sufficient to support the Lorentz forces experienced by the strand during testing. J_c data were obtained with transport current applied along the strand in both directions and the results averaged to make a first order correction for the self-field effect. Precision of the J_c measurements is about $\pm 2\%$.

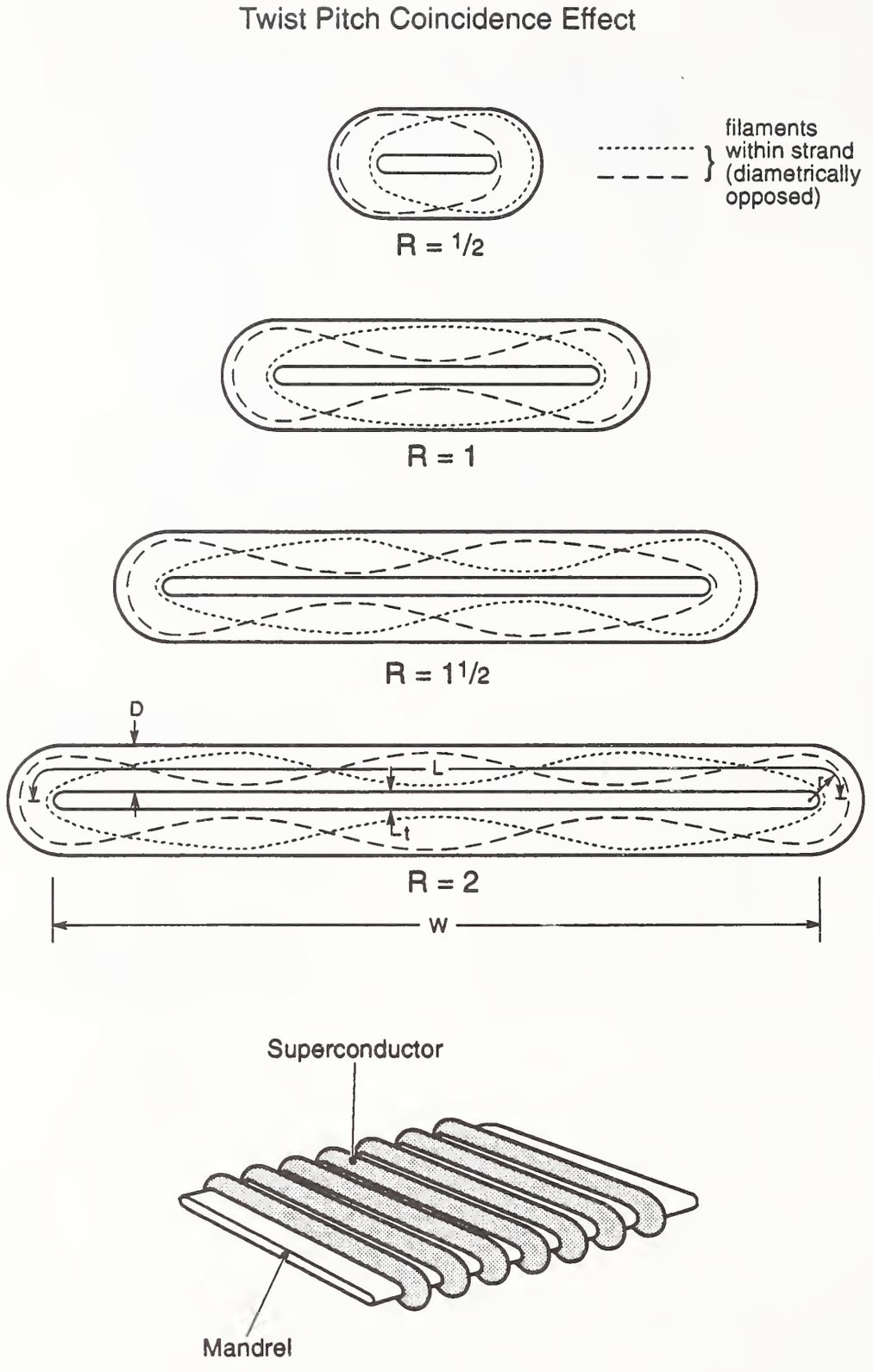

Figure 2. Test geometry, showing bend-to-bend separations that are an integer or half-integer multiple (R) of the strand twist pitch.

Results

Fig. 3 presents a logarithmic plot of a set of voltage-current ($V-I$) characteristics obtained on sample 1 when the strand bends are spaced by 1.5 and 2 strand twist pitches, S. Focusing on the data for a bend spacing of 1.5 S, we see that the slope of the $V-I$ curve is relatively low at high electric field. In contrast, for the other set of data where the bend spacing is 2 S, the slope of the $V-I$ characteristic is significantly higher at high electric fields and the critical current remains considerably higher, especially at electric fields below 10^{-7} V/cm. Furthermore, when the test is repeated at a smaller bend spacing of 1 S, the J_c and slope recover to higher values. Thus, the degradation in these quantities occurs only when the bend spacing is not an integer multiple of S.

This is seen more clearly in Fig. 4 where J_c has been determined at an electric field criterion of 10^{-7} V/cm and plotted as a function of the bend spacing (expressed as the cable/strand pitch ratio, R) imposed on the strand for magnetic fields ranging from 3 T to 8 T. Also shown in Fig. 4 are the results for several other NbTi strands having different local copper-to-superconductor area ratios (that is, the ratio in the immediate vicinity of each filament, not the overall ratio) and diffusion barrier materials. As seen in Fig. 4, the J_c for all samples periodically increases and decreases as the bend spacing alternately matches up with an integer or half-integer number of strand twist pitches. That is, an integer cable/strand twist pitch ratio consistently produced a ~10% J_c improvement in this test (corresponding to about a factor of 10 difference in voltage, as seen from Fig. 3) under widely varying conditions of magnetic field, local area ratio, and diffusion barrier material.

Similar results were obtained for the logarithmic slope of the $V-I$ curves. The slope of the $V-I$ curve can be represented by n,[3-5] defined as

$$n = d\ln V / d\ln I \, . \tag{2}$$

Plots of n versus the bend spacing are presented in Fig. 5. This figures shows that n periodically increases and decreases with the bend spacing, in direct correspondence to the variation in J_c. The highest values of the slope, n, are obtained when the bend spacing coincides with an integer number of strand twist pitches. The difference in n can be more than 60%.

Discussion

The logarithmic slope of the $V-I$ curve, n, is an index of the amount of inhomogeneity in J_c along the filaments within a strand.[6] As discussed in Ref. 6,

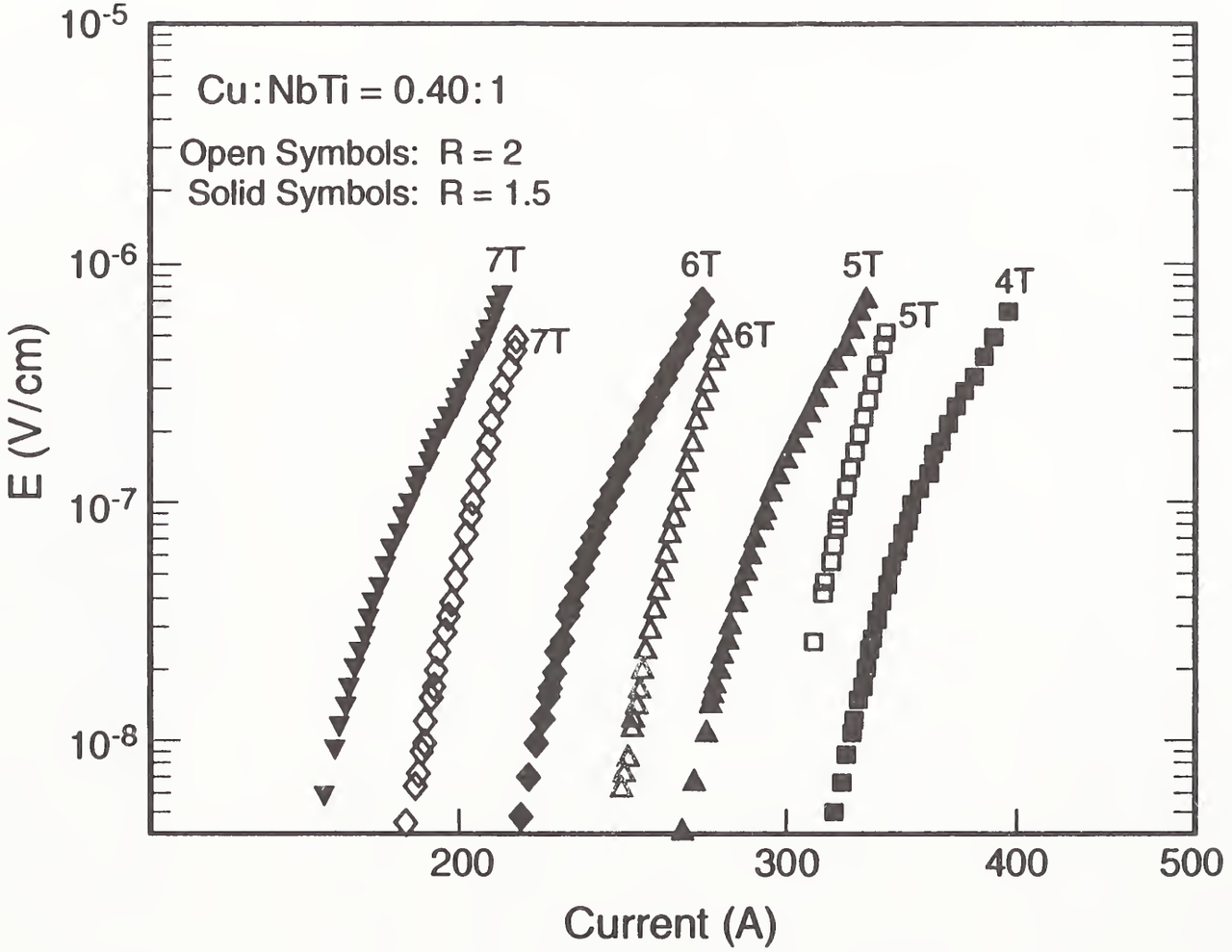

Figure 3. Logarithmic plot of the voltage-current characteristics of a NbTi strand showing significant degradation in J_c and n when bends are spaced apart by 1.5 twist pitches, in contrast to 2 twist pitches.

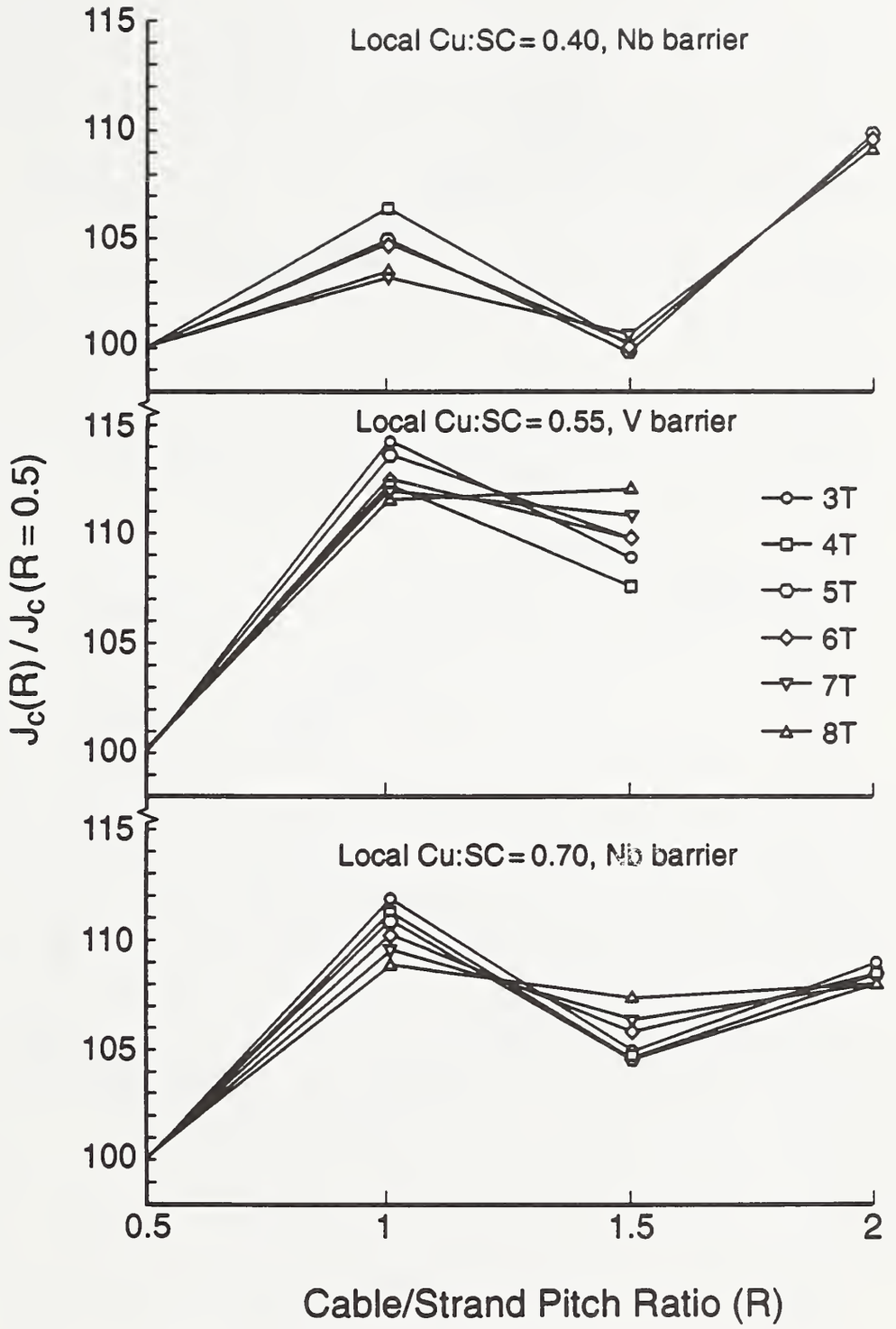

Figure 4. Critical current of three NbTi strands having different copper-to-superconductor local area ratios as a function of the cable-to-strand twist-pitch ratio, *R*. The data show a significant improvement in critical current for integer values of *R*.

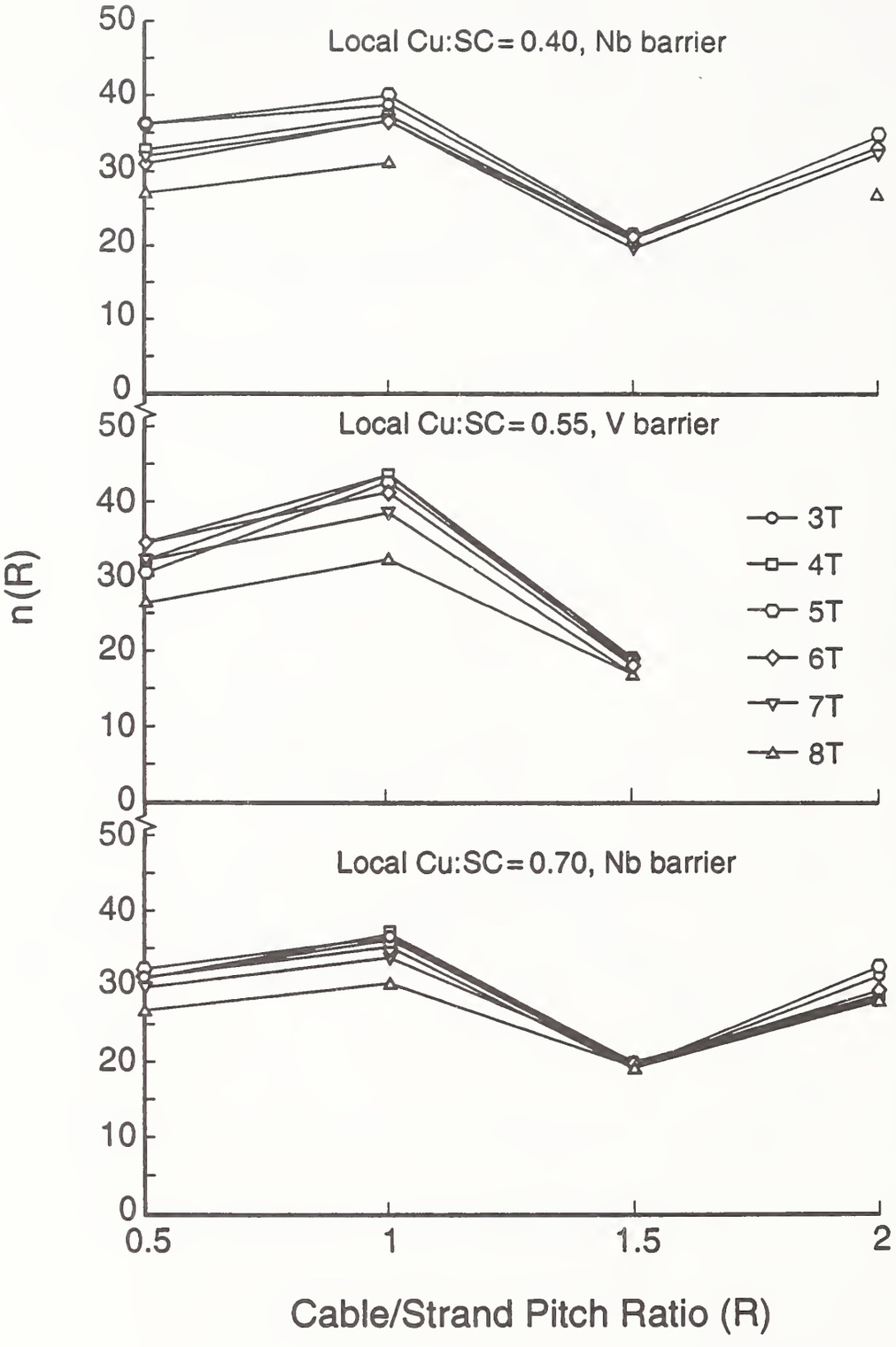

Figure 5. Logarithmic slope n of the voltage-current characteristics of the same three NbTi strands as in Fig. 4, showing a similar improvement in n for integer values of R.

however, n is affected only by inhomogeneities along a given filament, and not by differences between different filaments. The data presented here illustrate this point. For the half integer case, many filaments within the strand experience alternate high and low bend degradation at the points of bending. This forces considerable current transfer to occur among the filaments in order to redistribute the current among the filaments between bends in order to optimize the total current carried by the strand.

However, when the bend spacing is matched to the strand twist pitch, it is always the same group of filaments that are most severely degraded at each bend, and a large redistribution of current among the filaments is not needed to optimize the total current carried by the strand. Slight mismatches in the cable-to-strand twist pitch are not important, as long as the affected group of filaments changes slowly over many twist lengths so that a long length of strand is available for current to transfer from the degraded group of filaments to the less degraded group of filaments.

The strand length, x, needed to accommodate the transfer of current among the filaments is given by[3]

$$x = (0.1/n)^{1/2} (\rho_m/\rho^*)^{1/2} D \,, \tag{3}$$

where D is the strand diameter, ρ_m is the resistivity of the matrix material, and ρ^* is the resistivity criterion. Substituting values for these NbTi samples, we find that the current transfer length x becomes greater than the strand twist pitch at a strand resistivity ρ^* of about 1.4×10^{-13} Ω cm (an electric field of 10^{-8} V/cm at 6 T), which explains the degraded J_c seen *at low electric field levels* in Fig. 3 for half integer cable/strand pitch ratios. However, the transfer length x is less than a tenth the strand twist pitch at a high electric field of 10^{-6} V/cm, for example, corresponding to $\rho^* = 1.4 \times 10^{-11}$ Ω cm at 6 T. In this regime, the current can redistribute between successive bends and there is little effect, as seen in Fig. 3 *at high electric fields.* From a practical standpoint, however, strand resistivities for magnet applications should be less than 10^{-14} Ω cm, and thus this coincidence twist effect is expected to make a significant difference in such applications.

Application

These experiments were performed on strands wound around a mandrel with a very small cable twist pitch to have a significant number of bends within the small test volume of a research magnet. Equation 1, however, can be simply adapted to the practical Rutherford cable configuration where the strand progresses along the cable with a reasonable cable pitch. The strand length between bends L is then given approximately by:

$$L = [(P/2)^2 + W^2]^{1/2} = R\,S \tag{4}$$

where P is the cable twist pitch and W is the overall cable width. (If we make the reasonable assumption that the extra small amount of length at the strand's neutral axis needed to round the corner at the cable edge is approximately equal to twice the strand width, then this equation holds exactly.) As before, we desire that L be an integer number of strand twist pitches S (that is, the ratio $L/S \equiv R$ is an integer).

In the case of SSC cables, the strand twist pitch S is typically 12.7 mm and the cable pitch P is about 76 mm. The overall cable width is 12.3 mm for the inner cable and 11.7 mm for the outer cable. Substituting these values into Eq. 4 results in the coincident cable pitches given in Table 1. These data thus suggest that, instead of a cable twist pitch of 76 mm, setting the cable twist pitch to, for example, 72.1 mm for the inner cable, or 72.5 mm for the outer cable may be a simple way to improve the overall J_c in the these cables. Cables with different strand twist pitches or cable widths are readily determined using Eq. 4. Thus, this coincident twist method presents the possibility of enhancing the overall critical current simply with little additional cost, only an adjustment in twist pitch during cabling.

Table 1. Optimum Cable Twist Pitches for SSC Superconductor Cables

Cable/Strand Pitch Ratio	Inner Cable	Outer Cable
2	44.4 mm (1.75 in)	45.1 mm (1.78 in)
3	72.1 mm (2.84 in)	72.5 mm (2.86 in)
4	98.6 mm (3.88 in)	98.9 mm (3.89 in)
5	124.6 mm (4.90 in)	124.8 mm (4.91 in)

Acknowledgments

The author is grateful to G. Reinacker, N. Bergren, and C. Clickner for assistance with the measurements; N. Bergren, S. Bray, and R. Gerrans for help in preparing the cross-sectional photomicrograph; R. Goldfarb and R. Scanlan for helpful discussions. This work was supported by the U. S. Dept. of Energy, Div. of High Energy Physics, and the NIST superconductor program.

References

1. L. F. Goodrich, E. S. Pittman, J. W. Ekin, and R. M. Scanlan, Studies of NbTi strands extracted from coreless Rutherford cables, *IEEE Trans. Magn.* **23**, 1642 (1987).

2. J. W. Ekin, S. L. Bray, and N. F. Bergren, The effect of local area ratio and filament diffusion-barrier material on critical-current bend degradation of multifilamentary NbTi wires, *NISTIR 89-3912,* National Institute of Standards and Technology, Boulder, Colorado (1989).

3. J. W. Ekin, Current transfer in multifilamentary superconductors. I. Theory, *J. Appl. Phys.* **49**, 3406 (1978).

4. F. Voelker, *Particle Accelerators* **1**, 205 (1970).

5. L. F. Goodrich and F. R. Fickett, Critical current measurements: A compendium of experimental results, *Cryogenics* **22**, 225 (1982).

6. J. W. Ekin, Irregularity in Nb-Ti filament area and electric field versus current characteristics, *Cryogenics* **27**, 603 (1987).

Kim model for magnetization of type-II superconductors

D.-X. Chen[a] and R. B. Goldfarb
Electromagnetic Technology Division, National Institute of Standards and Technology,[b]
Boulder, Colorado 80303

(Received 31 January 1989; accepted for publication 18 May 1989)

We have calculated the initial magnetization curves and complete hysteresis loops for hard type-II superconductors. The critical-current density J_c is assumed to be a function of the internal magnetic field H_i according to Kim's model, $J_c(H_i) = k/(H_0 + |H_i|)$, where k and H_0 are constants. As is the case for other critical-state models, additional assumptions are that bulk supercurrent densities are equal to J_c, and that the lower critical field is zero. Our analytic solution is for an infinite orthorhombic specimen with finite rectangular cross section, $2a \times 2b$ ($a \leqslant b$), in which a uniform field H is applied parallel to the infinite axis. Assuming equal flux penetration from the sides, we reduced the two-dimensional problem to a one-dimensional calculation. The calculated curves are functions of b/a, a dimensionless parameter $p = (2ka)^{1/2}/H_0$, and the maximum applied field H_m. The field for full penetration is $H_p = H_0[(1+p^2)^{1/2} - 1]$. A related parameter is $H_m^* = H_0[(1+2p^2)^{1/2} - 1]$. Hysteresis loops were calculated for the different ranges of H_m: $H_m < H_p$, $H_p < H_m < H_m^*$, and $H_m^* < H_m$. The equations for an infinite cylindrical specimen of radius a are the same as those for a specimen with square cross section, $a = b$. In the limit $p \ll 1$ and $a = b$, our results reduce to those of the Bean model (J_c independent of H_i) for cylindrical geometry. Similarly, in the limit $p \ll 1$ and $b \to \infty$, the results are the same as those for a slab in the Bean model. For $H > 1.5\, H_p$, or $H > 0$ when $p \ll 1$, the width of the hysteresis loop ΔM may be used to deduce J_c as a function of H: $J_c(H) = \Delta M(H)/[a(1 - a/3b)]$.

I. INTRODUCTION

To derive magnetic properties of hard type-II superconductors, Bean[1,2] and London[3] introduced what has come to be known as the critical-state model.[4,5] The model assumes that penetrated supercurrents flow with a density equal to the critical-current density $J_c(H_i)$, where H_i is the local internal field. The flux vortex array is stable and there is no flux creep. The lower critical field is zero. In Bean's model, $J_c(H_i)$ was considered to be a constant independent of H_i. Since then, several different $J_c(H_i)$ functions have been proposed. Kim, Hempstead, and Strnad[4,5] assumed that

$$J_c(H_i) = k/(H_0 + |H_i|)\,, \tag{1}$$

where k and H_0 are positive constants (Kim's model). Watson[6] considered a simple linear function,

$$J_c(H_i) = A - C|H_i|\,, \tag{2}$$

where A and C are positive constants (linear model). Irie and Yamafuji[7] and Green and Hlawiczka[8] proposed a power-law model:

$$J_c(H_i) = k_1|H_i|^{-q}\,, \tag{3}$$

where k_1 and q are positive constants. Fietz *et al.*[9] and Karasik, Vasil'ev, and Ershov[10] proposed an exponential-law model:

$$J_c(H_i) = A_1 \exp(-|H_i|/C_1)\,, \tag{4}$$

in which A_1 and C_1 are positive constants.

In principle, the initial magnetization curve and hysteresis loops of superconductors can be derived for every model mentioned above. Kim *et al.*[5] obtained two sections of the high-field loop for cylinders. Hulbert[11] solved for the initial curve and high-field loop for cylinders. Fietz *et al.*[9] derived the initial curve and high-field loop for an infinite slab using the Kim model and a nonzero lower critical field. Watson[6] derived the initial curve for a cylindrical sample and calculated the loop for low fields. Irie and Yamafuji[7] derived the high-field loop for a slab. Ohmer and Heinrich[12] and Wollan and Ohmer[13] derived the initial curve and the low-, medium-, and high-field loops for a cylinder, for $H_0 = 0$ in Kim's model, and $q = 1$ in the power-law model. Karasik *et al.*[10] and Ravi Kumar and Chaddah[14] gave analytic solutions for the initial curves for cylinder and slab samples, respectively, using the exponential-law model. The latter also gave numerical solutions for the hysteresis loops.

In this paper we use Kim's model to analytically derive both the initial magnetization curve and the hysteresis loops for an orthorhombic sample. The equations are somewhat complicated because there are two constants in the expression for $J_c(H_i)$ and the sample shape is not simple. The loops may be of three types, depending on the value of the maximum applied field. In addition, each curve has several stages.

One of the motivations for using Kim's model for the derivation is that, of the models listed above, this one is quite general. It subsumes the linear model when $H_0 \gg H_i$, and Bean's model when both k and H_0 become infinite in such a way that k/H_0 is a constant. It becomes a power-law model for $q = 1$ if $H_0 = 0$. A practical motivation is that, by using Kim's model, we can more accurately predict the magnetic properties of superconductors for a realistic orthorhombic

[a] Permanent address: Department of Solid State Physics, Royal Institute of Technology, S100-44 Stockholm, Sweden.
[b] Formerly the National Bureau of Standards.

geometry. The physical significance of H_0 is discussed by Hulbert.[11]

The paper is organized as follows. Section II gives the general equation of magnetization for the orthorhombic geometry. Section III derives the magnetization as a function of field for different field ranges. Expressions are obtained for the initial curves and the hysteresis loops. Section IV uses the equations to generate hysteresis loops for several cases. In Sec. V, the formulas are simplified for a general orthorhombic Bean model. In Sec. VI, it is shown how $J_c(H)$ may be obtained from the width of the hysteresis loop.

II. GENERAL EXPRESSIONS FOR MAGNETIZATION

A. Orthorhombic geometry

We consider an infinitely long orthorhombic sample with cross section $2a \times 2b$ $(b \geqslant a)$. The boundaries of the sample are at $x = \pm a$ and $y = \pm b$. An external field H is applied along the z axis. The configuration of the sample and field direction are shown in Fig. 1(a). In this configuration, the magnetic quantities have only z components, and the supercurrents have only x and y components.

The critical-state model involves only macroscopic supercurrent, magnetization, flux density, and field. The lower critical field is assumed to be zero. The local internal field H_i is defined as

$$H_i = B/\mu_0 , \tag{5}$$

where B is the macroscopic local flux density and μ_0 is permeability of free space. If H is the applied field and M_i is the local magnetization, that is, the field produced by bulk supercurrents, we have

$$M_i = H_i - H . \tag{6}$$

The total magnetization M is the average of M_i over the sample cross section.

Solutions for an infinitely wide slab or an infinitely long cylinder involve only one variable of integration. We have to consider a two-dimensional problem for an orthorhombic sample. Fortunately, this two-dimensional problem can be simplified to a one-dimensional calculation. Because the sample is infinitely long and is located in a uniform H, both H_i and $J_c(H_i)$ along the sample surface must be the same on each side. Furthermore, the supercurrents penetrate the same depth into the sample from each side. The supercurrent path is the rectangular circuit shown in Fig. 1(a). For an infinitely long sample, the supercurrent density J, H_i and M_i along a given circuit are uniform and are written as functions of x: $J(x)$, $H_i(x)$, and $M_i(x)$.

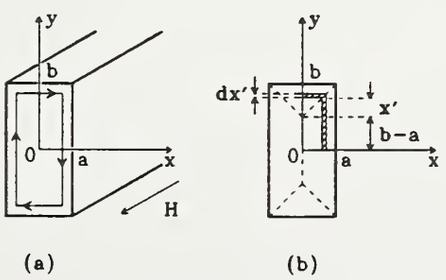

FIG. 1. (a) Sample configuration. (b) Supercurrent path.

To obtain the total magnetization M, we have to integrate $M_i(x)$ over the cross-sectional area. Because M is an average over the sample and because of symmetry, it is sufficient to take only the first quadrant $(x > 0,\ y > 0)$ into consideration. In this case the area is ab, and the differential area element is $(2x' + b - a)dx'$, as shown in Fig. 1(b). Thus,

$$M = \frac{1}{ab} \int_0^a (2x' + b - a) M_i(x')\, dx' . \tag{7}$$

In this equation we use primes to denote the variable of integration. In the remainder of the paper, the primes are omitted in the integrations.

B. Extension to cylinders and other geometries

In the limit $b/a = 1$, Eq. (7) for the average magnetization applies to a specimen with square cross section:

$$M = \frac{2}{a^2} \int_0^a x M_i(x)\, dx . \tag{7a}$$

The same expression applies to an infinite cylindrical specimen of radius a, where the area is πa^2 and the differential area element is $2\pi x\, dx$. Consequently, when b is set equal to a, the $M(H)$ curves derived below are for either square specimens, with cross section $2a \times 2a$, or cylindrical specimens, with radius a.[15]

The principle of equal supercurrent penetration from each side allows us to extend these arguments to samples with cross sections in the shape of triangles and polygons. The only requirement is that all sides are tangent to a circle of radius a. A technologically useful example is a regular hexagon.

III. DERIVATION OF $M(H)$ FROM $J(x)$

A. General expression for $J(x)$

To obtain M we have to first derive the supercurrent density $J(x)$. Using Ampere's law and Eq. (1), we have

$$\frac{dH_i}{dx} = -\operatorname{sgn}(J) J_c(H_i) = \frac{-\operatorname{sgn}(J)k}{H_0 + \operatorname{sgn}(H_i) H_i} , \tag{8}$$

where sgn is the sign function, equal to ± 1. From Eq. (8),

$$\int [H_0 + \operatorname{sgn}(H_i) H_i]\, dH_i = -\int \operatorname{sgn}(J) k\, dx . \tag{9}$$

After integration, the solution for the quadratic in H_i, in a region where H_i and J do not change their signs, is

$$H_i = -\operatorname{sgn}(H_i) H_0 \pm [H_0^2 - \operatorname{sgn}(JH_i) 2k(x + c)]^{1/2} , \tag{10}$$

where c is an integration constant to be determined by the boundary conditions. Multiplying Eq. (10) by $\operatorname{sgn}(H_i)$, we obtain

$$H_0 + \operatorname{sgn}(H_i) H_i = \pm \operatorname{sgn}(H_i) [H_0^2 - \operatorname{sgn}(JH_i) 2k(x + c)]^{1/2} \tag{11}$$

We set $\pm \operatorname{sgn}(H_i) = 1$ on the right-hand side because, from Eq. (1), the left-hand side is always positive. Using Eqs. (1) and (11) we obtain

$$J(x) = \operatorname{sgn}(J) J_c(H_i) = \operatorname{sgn}(J) k / [H_0 + \operatorname{sgn}(H_i) H_i]$$
$$= \operatorname{sgn}(J) k / [H_0^2 - \operatorname{sgn}(J H_i) 2k(x + c)]^{1/2} . \quad (12)$$

This is the general expression for $J(x)$.

B. Initial $M(H)$ curve and full-penetration field

1. Current densities and local fields

We start from the initial state, $H = M = 0$, and increase H in the z direction. According to Lenz's law, the supercurrent J (of negative sign) will penetrate from the surface ($x = a$) inward. If the supercurrent penetrates until $x = x_0$, H_i in the sample will be H at $x = a$, decrease to 0 at $x = x_0$, and remain 0 for $x < x_0$. Figures 2(a) and 2(b) show the $J(x)$ and $H_i(x)$ functions, represented schematically by straight-line segments. If H increases further, x_0 decreases. When $x_0 = 0$, the sample is completely penetrated [Figs. 2(c) and 2(d)]. The corresponding field is called the full-penetration field H_p. In the complete penetration state, $J(x)$ and $H_i(x)$ have similar forms, shown in Figs. 2(e) and 2(f).

For the initial magnetization curve, where the field is first applied to the sample, we will denote $J(x)$ as $J_0(x)$. We derive the supercurrent density $J_0(x)$ for $x_0 < x < a$. The boundary condition is

$$J_0(a) = -J_c(H) . \quad (13)$$

Substituting Eqs. (1) and (12) into Eq. (13), we have

$$[H_0^2 + 2k(a + c)]^{1/2} = H_0 + H , \quad (14)$$

from which

$$2kc = (H_0 + H)^2 - H_0^2 - 2ka . \quad (15)$$

Substituting Eq. (15) into Eq. (12), we obtain

$$J_0(x) = -k / [(H_0 + H)^2 - 2k(a - x)]^{1/2} \quad (x_0 < x < a) . \quad (16)$$

We consider the magnetization for two stages: $0 < H < H_p$ (stage I) and $H_p < H$ (stage II).

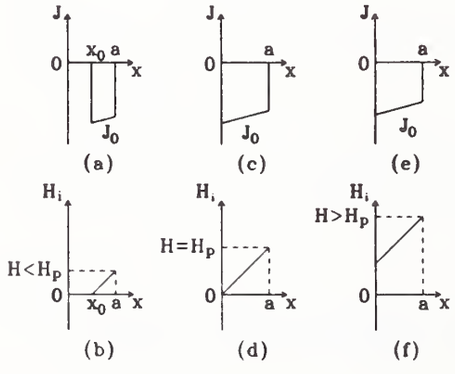

FIG. 2. Schematic supercurrent density J and local internal field H_i as functions of x for the initial magnetizing process. For purposes of illustration, J and H_i are sketched as straight line segments.

2. Stage I ($0 < H < H_p$)

In this range, x_0 decreases from a to 0, and

$$H_i(x) = 0 \quad (0 < x < x_0) , \quad (17a)$$

$$H_i(x) = H + \int_x^a J_0(x)\, dx \quad (x_0 < x < a) . \quad (17b)$$

From Eqs. (17a), (17b), and (6) we obtain

$$M_i(x) = -H \quad (0 < x < x_0) , \quad (18a)$$

$$M_i(x) = \int_x^a J_0(x)\, dx \quad (x_0 < x < a) . \quad (18b)$$

From Eqs. (17b) and (16), x_0 is determined:

$$x_0 = a - [(H_0 + H)^2 - H_0^2]/2k , \quad (19)$$

using the boundary condition

$$H_i(x_0) = 0 . \quad (20)$$

Substituting Eqs. (18a), (18b), and (16) into Eq. (7), and using Eq. (19), we obtain the final result:

$$M(H) = -Hx_0(b - a + x_0)/ab$$
$$- S_1(b + x_0)(a - x_0)/ab$$
$$+ (S_1^3 - H_0^3)Q_1 + 2H_0^3(a - x_0)/5kab$$
$$(0 < H < H_p) , \quad (21)$$

where

$$S_1 = H_0 + H , \quad (22a)$$

$$Q_1 = [5k(a + b) - 2S_1^2]/15abk^2 . \quad (22b)$$

For the case $a = b$, applicable to cylinders of radius a, Eq. (21) reduces to Hulbert's Eq. (10d), with appropriate symbol substitutions of H for B.[11] In the limit $b \to \infty$, for infinite slabs of thickness $2a$, Eq. (21) reduces to the solution of Fietz *et al.*, Eq. (b) in Table I of Ref. 9.

3. Full-penetration field H_p

When x_0 in Eq. (19) becomes 0, the sample is completely penetrated [Figs. 2(c) and 2(d)]. Setting $x_0 = 0$ so that, by definition, $H = H_p$ in Eq. (19), we obtain

$$H_p = (H_0^2 + 2ka)^{1/2} - H_0 . \quad (23)$$

4. Stage II ($H_p < H$)

In this range [Figs. 2(e) and 2(f)], Eqs. (7), (16), (17b), and (18b) are still valid with x_0 replaced by 0. The final result is

$$M(H) = -S_1 + (S_1^3 - R_1^3)Q_1 + 2R_1^3/5kb$$
$$(H_p < H < H_m) , \quad (24)$$

where

$$R_1 = (S_1^2 - 2ka)^{1/2} \quad (25)$$

C. Hysteresis loops for the low-H_m case ($H_m < H_p$)

To obtain hysteresis loops we have to derive reverse $M(H)$ curves from a given maximum field H_m on the initial curve. The reverse $M(H)$ curve starts from (H_m, M_m) and ends at $(-H_m, -M_m)$, forming the descending branch of the hysteresis loop. The ascending branch will then be

$-M(-H)$. The equations governing the shape of the hysteresis loops depend on H_m. The first case is for $H_m < H_p$, where the specimen is never fully penetrated. The second case is for $H_m^* < H_m$, when the reverse supercurrent penetrates to the center of the specimen before H is cycled back to zero. (The expression for H_m^* is derived in Sec. III D 2.) The third case is intermediate, $H_p < H_m < H_m^*$.

1. Current densities and local fields

The low-H_m reverse $M(H)$ curve starts from a point on stage I of the initial curve, $H_m < H_p$. Figures 3(a)–3(j) show the $J(x)$ and $H_i(x)$ functions developing with decreasing H. Figures 3(a) and 3(b), similar to Figs. 2(a) and 2(b), correspond to the starting point with $H = H_m$ and a negative supercurrent penetrating to x_m. When H decreases from H_m, the induced supercurrent with positive J will penetrate from the sample surface to $x = x_1$, and the corresponding $J(x)$ and $H_i(x)$ are shown in Figs. 3(c) and 3(d). At this point, $J(x)$ for $x_m < x < x_1$ [denoted as $J_m(x)$] remains the same as the $J_0(x)$ for the initial magnetization when $H = H_m$. $J(x)$ is $J_1(x)$ for $x_1 < x < a$. This arrangement is maintained until $H = 0$, as shown in Fig. 3(e) and 3(f). Further decreasing H to a negative value complicates the situation. As shown in Figs. 3(g) and 3(h), the expression for $J(x)$ has to be divided into three parts: $J_m(x)$, $J_2(x)$, and $J_3(x)$, and the corresponding H_i changes sign at $x = x_3$. This situation lasts until $H = -H_m$, when both J_m and J_2 are removed. Figures 3(i) and 3(j) show $J(x)$ and $H_i(x)$ for $H = -H_m$; they are opposite to the case shown in Figs. 3(a) and 3(b).

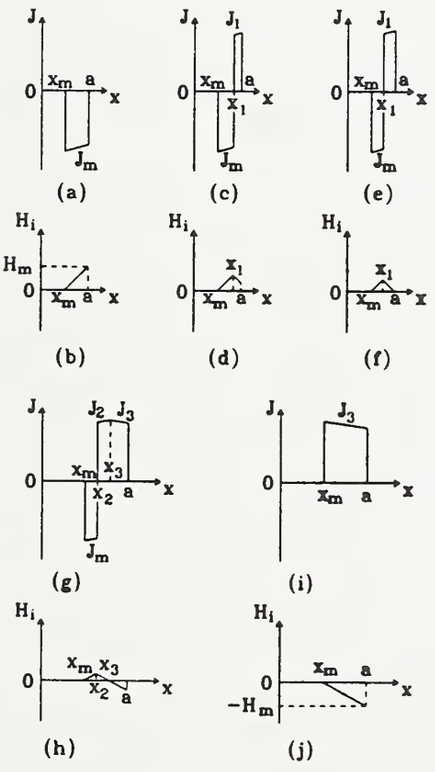

FIG. 3. Schematic supercurrent density and local internal field as functions of x for the reverse magnetizing process from $H_m < H_p$.

We give the expressions for $J_m(x)$, $J_1(x)$, $J_2(x)$, and $J_3(x)$. Because $J_m(x) = J_0(x)$ when $H = H_m$, we obtain from Eq. (16):

$$J_m(x) = -k/[(H_0 + H_m)^2 - 2k(a-x)]^{1/2} \quad (x_m < x < x_1) . \tag{26}$$

The boundary condition for $J_1(x)$ is

$$J_1(a) = J_c(H) . \tag{27}$$

Substituting Eqs. (1) and (12) into Eq. (27) we have

$$[H_0^2 - 2k(a+c)]^{1/2} = H_0 + H , \tag{28}$$

from which

$$2kc = -(H_0 + H)^2 + H_0^2 - 2ka . \tag{29}$$

Substituting Eq. (29) into Eq. (11) we obtain

$$J_1(x) = k/[(H_0 + H)^2 + 2k(a-x)]^{1/2} \quad (x_1 < x < a) . \tag{30}$$

The boundary conditions for $J_2(x)$ and $J_3(x)$ are

$$J_2(x_3) = J_c(0) \tag{31a}$$

and

$$J_3(a) = J_c(H) . \tag{31b}$$

By a similar derivation, we obtain

$$J_2(x) = k/[H_0^2 + 2k(x_3 - x)]^{1/2} \quad (x_2 < x < x_3) \tag{32a}$$

and

$$J_3(x) = k/[(H_0 - H)^2 - 2k(a-x)]^{1/2} \quad (x_3 < x < a) . \tag{32b}$$

The magnetization process can be divided into two stages. Stage I corresponds to $0 < H < H_m$, and stage II corresponds to $-H_m < H < 0$.

2. Stage I ($0 < H < H_m$)

In stage I, $H_i(x)$ is

$$H_i(x) = 0 \quad (0 < x < x_m) , \tag{33a}$$

$$H_i(x) = H_m + \int_x^a J_m(x)\,dx \quad (x_m < x < x_1) , \tag{33b}$$

$$H_i(x) = H + \int_x^a J_1(x)\,dx \quad (x_1 < x < a) . \tag{33c}$$

From Eqs. (33a), (33b), and (33c) and Eq. (6), $M_i(x)$ is obtained as

$$M_i(x) = -H \quad (0 < x < x_m) , \tag{34a}$$

$$M_i(x) = H_m - H + \int_x^a J_m(x)dx \quad (x_m < x < x_1) , \tag{34b}$$

$$M_i(x) = \int_x^a J_1(x)\,dx \quad (x_1 < x < a) . \tag{34c}$$

x_m can be determined by replacing H in Eq. (19) with H_m:

$$x_m = a - [(H_0 + H_m)^2 - H_0^2]/2k . \tag{35a}$$

Using the continuity of H_i at $x = x_1$, and from Eqs. (33b) and (33c), we obtain

$$x_1 = a - [(H_0 + H_m)^2 - (H_0 + H)^2]/4k . \quad (35b)$$

Substituting Eqs. (34a), (34b), (34c), (26), and (30) into Eq. (7), and using x_m and x_1 defined by Eqs. (35a) and (35b) we obtain the final result:

$$\begin{aligned} M(H) = & -Hx_m(b-a+x_m)/ab \\ & - S_1[ab + (a-b)x_m - x_m^2]/ab \\ & - (S_1^3 - R_2^3)Q_2 + (R_2^3 - H_0^3)Q_3 \\ & + 2[(x_1 - a)R_2^3 + (x_1 - x_m)H_0^3]/5kab \\ & (0 < H < H_m) , \end{aligned} \quad (36)$$

where

$$S_2 = H_0 + H_m , \quad (37a)$$

$$R_2 = [S_1^2 + 2k(a - x_1)]^{1/2} \quad (37b)$$

$$Q_2 = [5k(a+b) + 2S_1^2]/15abk^2 , \quad (37c)$$

$$Q_3 = [10k(a+b) + 3S_1^2 - 7S_2^2]/30abk^2 \quad (37d)$$

3. Stage II ($-H_m < H < 0$)

In stage II, $H_i(x)$ and $M_i(x)$ are

$$H_i(x) = 0 \quad (0 < x < x_m) , \quad (38a)$$

$$H_i(x) = H_m + \int_x^a J_m(x)\,dx \quad (x_m < x < x_2) , \quad (38b)$$

$$H_i(x) = H + \int_x^{x_1} J_2(x)dx + \int_{x_1}^a J_3(x)dx \quad (x_2 < x < x_3) , \quad (38c)$$

$$H_i(x) = H + \int_x^a J_3(x)dx \quad (x_3 < x < a) , \quad (38d)$$

and

$$M_i(x) = -H \quad (0 < x < x_m) , \quad (39a)$$

$$M_i(x) = H_m - H + \int_x^a J_m(x)dx \quad (x_m < x < x_2) , \quad (39b)$$

$$M_i(x) = \int_x^{x_1} J_2(x)dx + \int_{x_1}^a J_3(x)dx \quad (x_2 < x < x_3) , \quad (39c)$$

$$M_i(x) = \int_x^a J_3(x)dx \quad (x_3 < x < a) . \quad (39d)$$

x_m is given in Eq. (35a), and x_3 and x_2 can be derived using the continuity conditions at $x = x_3$ and x_2 from Eqs. (38d), (38c), and (38b):

$$x_3 = a - [(H_0 - H)^2 - H_0^2]/2k , \quad (40a)$$

$$x_2 = a - [(H_0 - H)^2 + (H_0 + H_m)^2 - 2H_0^2]/4k . \quad (40b)$$

The final result is obtained in the standard way used above:

$$\begin{aligned} M(H) = & \\ & - Hx_m(b-a+x_m)/ab + S_3(a-x_3)(b+x_3)/ab \\ & - S_1(x_3 - x_2)[2(b-a+x_2) + x_3 + x_m]/ab \\ & - (S_3^3 - H_0^3)Q_4 + (R_3^3 - H_0^3)(Q_5 + Q_6) \\ & + 2[(x_3 - a)H_0^3 - (x_3 - x_2)(R_3^3 - H_0^3)]/5kab \\ & (-H_m < H < 0) , \end{aligned} \quad (41)$$

where

$$S_3 = H_0 - H , \quad (42a)$$

$$R_3 = [H_0^2 + 2k(x_3 - x_2)]^{1/2} , \quad (42b)$$

$$Q_4 = [5k(a+b) - 2S_3^2]/15abk^2 , \quad (42c)$$

$$Q_5 = [5k(a+b) - 5S_3^2 + 7H_0^2]/15abk^2 , \quad (42d)$$

$$Q_6 = [10k(a+b) - 3S_3^2 - 7S_2^2 + 6H_0^2]/30abk^2 . \quad (42e)$$

D. Hysteresis loops for the high-H_m case ($H_m^* < H_m$)

1. Current densities and local fields

For $H_m > H_p$ we have to consider two cases. In the high-H_m case, the reverse supercurrent completely penetrates to the sample center before H has decreased to 0. This corresponds to $H_m > H_m^* = (H_0^2 + 4ka)^{1/2} - H_0$ as shown below. The second case is for medium H_m, where the reverse supercurrent is not completely penetrated when $H = 0$. This will be discussed in Sec. III E.

$J(x)$ and $H_i(x)$ for the high-H_m case are shown in Figs. 4(a)–4(n). Figures 4(a) and 4(b) correspond to the starting point when $H = H_m$ and the sample is completely penetrated by negative supercurrent with density $J_m(x)$. Decreasing H from H_m induces a positive supercurrent with density $J_1(x)$. As can be seen in Figs. 4(c) and 4(d), the reverse positive supercurrent penetrates to $x = x_1$, at which point $H = H_{prh}$, the full reverse penetration field for the high-H_m case, defined below. This is stage I.

Stage II starts when x_1 becomes 0, shown in Figs. 4(e) and 4(f), and ends when H reaches 0, shown in Figs. 4(g) and 4(h). After that comes stage III, in which the local internal fields at the center and the surface of the sample have different signs, corresponding to different functions for $J_2(x)$ and $J_3(x)$, bounded by $x = x_3$, where $H_i = 0$. This situation is shown in Figs. 4(i) and 4(j). Further decreasing H results in the situation of Figs. 4(k) and 4(l), when the whole sample has negative H_i, and the magnetization process enters stage IV. In stage IV, $J(x)$ keeps the form of $J_3(x)$ until $H = -H_m$, when the process ends. The final $J(x)$ and $H_i(x)$ are shown in Figs. 4(m) and 4(n).

The expressions for $J_m(x)$, $J_1(x)$, $J_2(x)$, and $J_3(x)$ have already been given in Eqs. (26), (30), (32a), and (32b), and we need only change the regions of x, referring to the figures as described above.

2. Stage I ($H_{prh} < H < H_m$)

In stage I, $H_i(x)$ and $M_i(x)$ are

$$H_i(x) = H_m + \int_x^a J_m(x)dx \quad (0 < x < x_1) , \quad (43a)$$

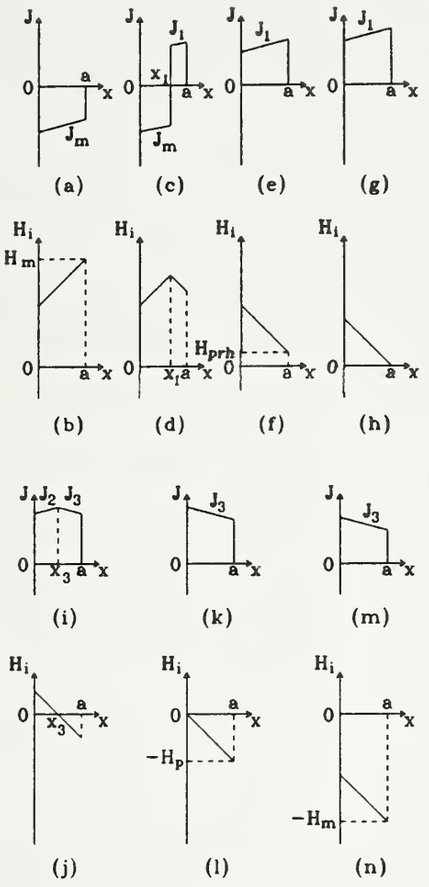

FIG. 4. Same as Fig. 3, from $H_m > H_m^*$.

$$H_i(x) = H + \int_x^a J_1(x)dx \quad (x_1 < x < a)\,, \tag{43b}$$

and

$$M_i(x) = H_m - H + \int_x^a J_m(x)dx \quad (0 < x < x_1)\,, \tag{44a}$$

$$M_i(x) = \int_x^a J_1(x)dx \quad (x_1 < x < a)\,. \tag{44b}$$

x_1 is given in Eq. (35b), and the final result is

$$M(H) = -S_1 - (S_1^3 - R_2^3)Q_2 + (R_2^3 - R_4^3)Q_3 + 2[(x_1 - a)R_2^3 + x_1 R_4^3]/5kab \quad (H_{prh} < H < H_m)\,, \tag{45}$$

in which

$$R_4 = (S_2^2 - 2ka)^{1/2}\,, \tag{46}$$

and H_{prh} is the reverse full-penetration field for the high-H_m case. It can be determined by taking $x_1 = 0$ in Eq. (35b):

$$H_{prh} = [(H_0 + H_m)^2 - 4ka]^{1/2} - H_0\,. \tag{47}$$

The boundary between the high- and medium-H_m case can also be determined from Eq. (35b) by taking $x_1 = 0$ and $H = 0$:

$$H_m^* = (H_0^2 + 4ka)^{1/2} - H_0\,. \tag{48}$$

In the limit $b \to \infty$, Eq. (45) reduces to Eq. (d) in Table I, Ref. 9, with the typographic correction "...{($\sqrt{2}/2$)[... + $2B_0^2$]$^{3/2}$...}."

3. Stage II ($0 < H < H_{prh}$)

In stage II, the $H_i(x)$ and $M_i(x)$ are

$$H_i(x) = H + \int_x^a J_1(x)dx \quad (0 < x < a)\,, \tag{49}$$

$$M_i(x) = \int_x^a J_1(x)dx \quad (0 < x < a)\,. \tag{50}$$

x_1 is given in Eq. (35b), and the final result is

$$M(H) = -S_1 - (S_1^3 - R_5^3)Q_2 - 2R_5^3/5kb \quad (0 < H < H_{prh})\,, \tag{51}$$

where

$$R_5 = (S_1^2 + 2ka)^{1/2}\,. \tag{52}$$

For the case $a = b$, applicable to cylinders of radius a, Eq. (51) reduces to Kim's solution for $M(H)$ in the first quadrant, Eq. (14) in Ref. 5, and to Hulbert's solution, Eq. (10b) in Ref. 11. In the limit $b \to \infty$, for infinite slabs of thickness $2a$, Eq. (51) reduces to the solution of Fietz *et al.*, Eq. (e) in Table I of Ref. 9.

4. Stage III ($-H_p < H < 0$)

In stage III, the $H_i(x)$ and $M_i(x)$ are

$$H_i(x) = H + \int_x^{x_3} J_2(x)dx + \int_{x_3}^a J_3(x)dx \quad (0 < x < x_3)\,, \tag{53a}$$

$$H_i(x) = H + \int_x^a J_3(x)dx \quad (x_3 < x < a)\,, \tag{53b}$$

and

$$M_i(x) = \int_x^{x_3} J_2(x)dx + \int_{x_3}^a J_3(x)dx \quad (0 < x < x_3)\,, \tag{54a}$$

$$M_i(x) = \int_x^a J_3(x)dx \quad (x_3 < x < a)\,. \tag{54b}$$

x_3 is given in Eq. (40a), and the final result is

$$M(H) = S_3(a - x_3)(b + x_3)/ab - S_1 x_3(b - a + x_3)/ab - (S_3^3 - H_0^3)Q_4 - (H_0^3 - R_6^3)Q_5 - 2[(a - x_3)H_0^3 + x_3 R_6^3]/5kab \quad (-H_p < H < 0)\,, \tag{55}$$

where

$$R_6 = (H_0^2 + 2kx_3)^{1/2}\,. \tag{56}$$

The lower H boundary in this stage is $-H_p$, as can be seen by taking $x_3 = 0$ in Eq. (40a). For the case $a = b$, applicable to cylinders of radius a, Eq. (55) reduces to Hulbert's Eq. (10c), with appropriate symbol substitutions of H for B.[11] In the limit $b \to \infty$, Eq. (55) reduces to Eq. (g) in Table I, Ref. 9, with the typographic correction

"$-(\mathbf{B_0}+\mathbf{H_a}) + ...\{[... - (B_0 - H_0)^2 + ...]^{3/2} - ...\} + ...$."

5. Stage IV ($-H_m < H < -H_p$)

In stage IV, the $H_i(x)$ and $M_i(x)$ are

$$H_i(x) = H + \int_x^a J_3(x)dx \quad (0 < x < a)\,, \tag{57}$$

$$M_i(x) = \int_x^a J_3(x)dx \quad (0 < x < a)\,, \tag{58}$$

and the final result is

$$M(H) = S_3 - (S_3^3 - R_7^3)Q_4 - 2R_7^3/5kb \quad (-H_m < H < -H_p)\,, \tag{59}$$

where

$$R_7 = (S_3^2 - 2ka)^{1/2} \tag{60}$$

To generate the complete hysteresis loop, stages I–IV are reflected about the origin onto the third and fourth quadrants, as indicated at the beginning of Sec. III C. For example, Eq. (59) in the second quadrant becomes

$$M(H) = -S_1 + (S_1^3 - R_1^3)Q_1 + 2R_1^3/5kb \quad (H_p < H < H_m) \tag{59a}$$

in the fourth quadrant, in which H and $M(H)$ are replaced by $-H$ and $-M(H)$. Equation (59a) is the same as Eq. (24) for stage II of the initial curve. For the case $a = b$, applicable to cylinders of radius a, Eq. (59a) reduces to Kim's solution for $M(H)$ in the fourth quadrant, Eq. (14) in Ref. 5, and to Hulbert's solution, Eq. (10a) in Ref. 11. In the limit $b \to \infty$, for infinite slabs of thickness $2a$, Eq. (59a) reduces to the solution of Fietz *et al.*, Eq. (c) in Table I of Ref. 9.

E. Hysteresis loops for the medium-H_m case ($H_p < H_m < H_m^*$)

1. Current densities and local fields

For the medium-H_m case, the reverse magnetization process is shown in Figs. 5(a)–5(n). The difference between Figs. 5(a)–5(n) and Figs. 4(a)–4(n) is only for stage II. At the end of stage I [Figs. 5(e) and 5(f)], $H = 0$, but x_1 is still greater than 0. Therefore, in stage II, when $H < 0$, $J(x)$ has to be divided into three parts: $J_m(x)$, $J_2(x)$, and $J_3(x)$, shown in Figs. 5(g) and 5(h). The next stage starts from the point where $x_2 = 0$, as shown in Figs. 5(i) and 5(j). The expressions for $J(x)$ are the same as in the high-H_m case.

2. Stage I ($0 < H < H_m$)

This stage is the same as for the high-H_m case except for the field interval, which is from H_m to 0 here.

3. Stage II ($H_{prm} < H < 0$)

In stage II, $H_i(x)$ and $M(x)$ are

$$H_i(x) = H_m + \int_x^a J_m(x)dx \quad (0 < x < x_2)\,, \tag{61a}$$

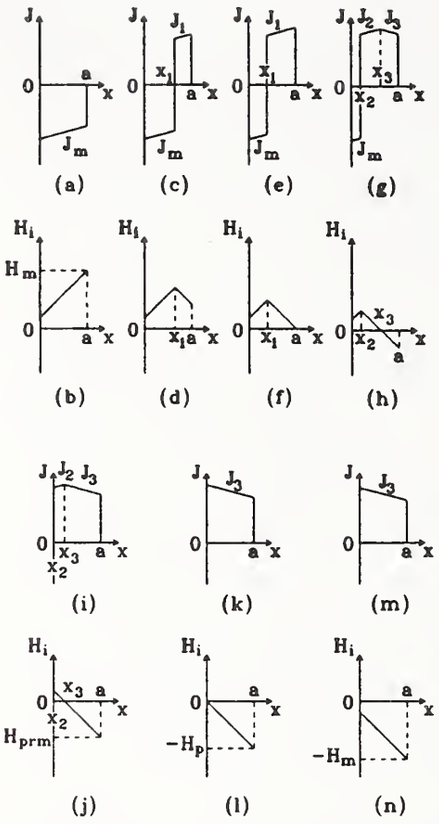

FIG. 5. Same as Fig. 3, from H_m between H_p and H_m^*.

$$H_i(x) = H + \int_x^{x_1} J_2(x)dx + \int_{x_1}^a J_3(x)dx \quad (x_2 < x < x_3)\,, \tag{61b}$$

$$H_i(x) = H + \int_x^a J_3(x)dx \quad (x_3 < x < a)\,, \tag{61c}$$

and

$$M_i(x) = H_m - H + \int_x^a J_m(x)dx \quad (0 < x < x_2)\,, \tag{62a}$$

$$M_i(x) = \int_x^{x_1} J_2(x)dx + \int_{x_1}^a J_3(x)dx \quad (x_2 < x < x_3)\,, \tag{62b}$$

$$M_i(x) = \int_x^a J_3(x)dx \quad (x_3 < x < a)\,. \tag{62c}$$

x_2 and x_3 are given in Eqs. (40b) and (40a), and the final result is

$$M(H) = S_3(a - x_3)(b + x_3)/ab - S_1[x_3^2 + (b - a)x_3]/ab - (S_3^3 - H_0^3)Q_4 - (H_0^3 - R_3^3)Q_5 + (R_3^3 - R_4^3)Q_6 - 2[(a - x_3)H_0^3 + (x_3 - x_2)R_3^3 - x_2R_4^3]/5kab \quad (H_{prm} < H < 0)\,, \tag{63}$$

where H_{prm} is the reverse full-penetration field for the medium-H_m case, which can be determined by taking $x_2 = 0$ in Eq. (40b):

$$H_{prm} = H_0 - [4ka + 2H_0^2 - (H_0 + H_m)^2]^{1/2} . \quad (64)$$

4. Stage III ($-H_p < H < H_{prm}$)

This stage is the same as the high-H_m case except for the interval of H, which is here from H_{prm} to $-H_p$.

5. Stage IV ($-H_m < H < -H_p$)

This stage is the same as the high-H_m case.

IV. COMPUTED $M(H)$ CURVES

We have analytically verified, for each case in Sec. III, that the stages are continuous at their end points. To illustrate the formulas in Sec. III, we give some computed $M(H)$ curves. To reduce the number of variables, we define a new parameter, similar to one used by Kim[5]:

$$p = (2ka)^{1/2}/H_0 . \quad (65)$$

Equations (23) and (48) can be rewritten as

$$H_p = H_0[(1 + p^2)^{1/2} - 1] , \quad (66)$$

$$H_m^* = H_0[(1 + 2p^2)^{1/2} - 1] . \quad (67)$$

The shapes of the $M(H)$ curves are now determined by p and b/a. Figures 6(a)–6(e) give the initial and hysteresis $M(H)$ curves for $b/a = 1$ and $p = 0.3$, 1, 3, 10, and 1000. For each case, five $M(H)$ loops are drawn for $H_m = H_p/2$, H_p, $(H_p + H_m^*)/2$, H_m^*, and $4H_p$. The curves in Figs. 7(a) and 7(b) give the initial and hysteresis $M(H)$ curves for $p = 1$, $H_m = H_m^*$ and $4H_p$, and $b/a = 1$ (smallest), 1.5, 2, 5, and 100 (largest). For all the curves, M and H are normalized to H_p.

We can observe from Figs. 6(a)–6(e) that the $M(H)$ curves derived from Kim's model have a wide variety. The curves shown in Fig. 6(a) are very similar to those derived from Bean's model.[2] If p were smaller than 0.1, there would be virtually no difference between Kim's and Bean's models. Figure 6(e) for $p = 1000$ is almost the same as for the limiting case $p \to \infty$, where Kim's model reduces to $J_c(H_i) = k/H_i$.

The initial curves have minima except when $p = 0$. We can see from Figs. 6(a)–6(e) that, with increasing p, the field where the minimum is located decreases from H_p to $0.56\,H_p$, and the minimum M decreases from $-0.33\,H_p$ to $-0.36\,H_p$. The initial slopes of the initial curves are -1. For $p = 1000$, the initial curve is linear within 1% up to $0.09\,H_p$, despite the assumption of zero lower critical field in the derivation. This linear region does not come from a Meissner state, but is simply a reflection of a large J_c at low H_i.

The initial reverse slopes at the corners of the hysteresis loops in Figs. 6(a)–6(e) are also -1. This is a consequence of shielding by surface supercurrent at the beginning of stage I. Because J_c is lower, this 1% linear region is smaller.

The second and the fourth loops correspond to the two boundaries between the low-, medium-, and high-H_m cases. We can see from Figs. 6(a)–6(e) that, for the medium- and high-H_m cases, the initial and the hysteresis curves merge

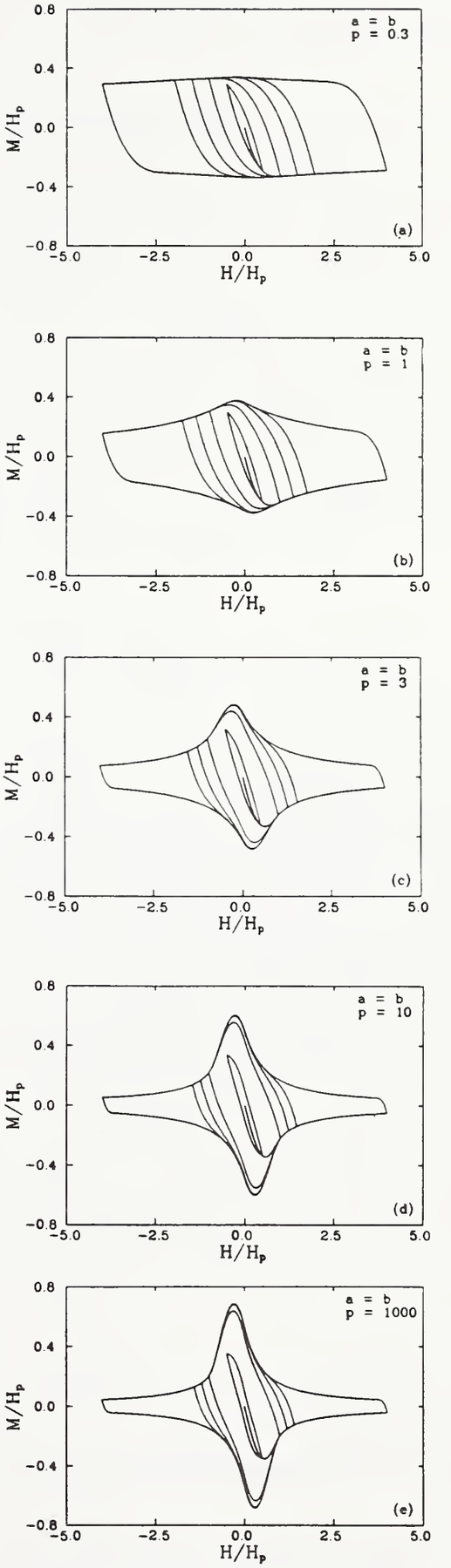

FIG. 6. Theoretical M-H curves, scaled by H_p, for a sample with $b/a = 1$, for $p =$ (a) 0.3, (b) 1, (c) 3, (d) 10, and (e) 1000. In each figure, loops are shown for $H_m/H_p = 0.5$ (smallest), 1, $\frac{1}{2} + H_m^*/2H_p$, H_m^*/H_p, and 4 (largest).

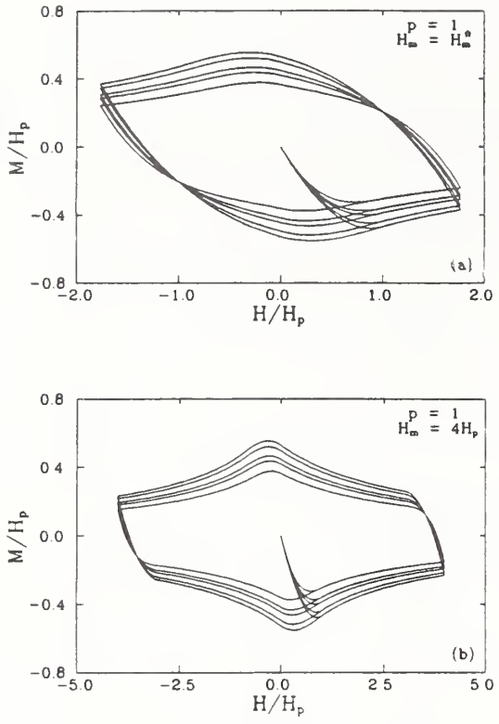

FIG. 7. Theoretical M-H curves, scaled by H_p, for $p=1$ and (a) $H_m = H_m^*$, (b) $H_m = 4H_p$. In each figure, curves are shown for samples with aspect ratio $b/a = 1$ (smallest), 1.5, 2, 5, and 100 (largest).

when $H \geqslant H_p$. The middle parts, around $H=0$, are the same for all the loops in the high-H_m case.

With increasing b/a, the width of the normalized hysteresis loop increases asymptotically, as seen in Figs. 7(a) and 7(b). One interesting feature in Figs. 7(a) and 7(b) is that, for each figure, the loops with the same p and H_m cross at two points. This crossover effect is general for $H_m > H_p$. For $H_m = H_m^*$ the crossing points are at $H = \pm H_p$, but for higher H_m the points are at higher fields. For a set of samples with the same a and different b, when $H = H_m$, $H_i(0)$ should be the same for all the samples, because H_i is a function only of x. When H is reduced from this H_m to a value H_{cro} that equals this $H_i(0)$, x_1 will become $a/2$. Changing the variable in Eq. (7) such that $\xi = x - a/2$, we have

$$M_{cro} = \frac{1}{ab}\int_{-a/2}^{+a/2} (2\xi + b) M_i(\xi)\, d\xi \,. \tag{68}$$

Because $M_i(\xi)$ is an even function of ξ, Eq. (68) can be written as

$$M_{cro} = \frac{1}{a}\int_{-a/2}^{+a/2} M_i(\xi)\, d\xi \,, \tag{69}$$

independent of b. Since both H_{cro} and M_{cro} are independent of b for constant a, the point (H_{cro}, M_{cro}) must be a crossing point, as illustrated in Figs. 7(a) and 7(b).

V. $M(H)$ FORMULAS FOR ORTHOHOMBIC SAMPLES IN THE BEAN LIMIT

Bean derived the $M(H)$ formulas for cylindrical and infinite-slab samples for J_c independent of H_i. In this paper, we have obtained the $M(H)$ formulas for the orthorhombic geometry using Kim's model for J_c, Eq. (1). In this section, we reduce the orthorhombic Kim formulas to general orthorhombic Bean formulas. Finally, we reduce these to the simple cylinder and slab forms.

A. Bean's model for orthorhombic samples

Bean's model can be written as

$$J_c(H_i) = J_c \,, \tag{70}$$

where J_c is constant. To modify Kim's model, Eq. (1), for the Bean limit, let

$$k \to \infty \,, \tag{71a}$$

$$H_0 \to \infty \,, \tag{71b}$$

$$k/H_0 = J_c \,. \tag{71c}$$

All the formulas for Kim's model can be reduced to the corresponding ones for Bean's model. For some cases, namely Eqs. (74), (75b), (77a), and (77b) below, it was necessary to use binomial expansions before taking the limits in Eqs. (71a), (71b), and (71c). For the terms raised to the power 3/2 in Eqs. (24), (45), and (51), expansions has to be carried to third order.

The general expression for the supercurrent density can be obtained from Eq. (12):

$$J(x) = \mathrm{sgn}(J) J_c \,. \tag{72}$$

For each specific case we have

$$J_0 = J_m = -J_c \tag{73a}$$

and

$$J_1 = J_2 = J_3 = J_c \,. \tag{73b}$$

We do not have to identify J_1, J_2, and J_3 because we do not need to separate $J(x)$ into several sections, since J_c is constant. For the same reason, for every $M(H)$ curve, only one or two stages have to be considered, and for the reverse curves, only two cases have to be considered.

The full-penetration field can be obtained from Eq. (23) as

$$H_p = J_c a \,. \tag{74}$$

The initial $M(H)$ curve can be derived from Eqs. (21) and (24) as

$$M(H) = -H + (H^2/2J_c)(1/a + 1/b) - H^3/(3J_c^2 ab) \qquad (0 < H < H_p) \,, \tag{75a}$$

$$M(H) = -J_c a(\tfrac{1}{2} - a/6b) \quad (H_p < H) \,. \tag{75b}$$

Equations (75a) and (75b) may be found in Ref. 15. The reverse curve for the low-H_m $(0 < H_m < H_p)$ case can be derived from Eq. (36) as

$$M(H) = -H + [(H_m^2 + 2HH_m - H^2)/4J_c](1/a + 1/b) - (3H_m^3 + 3H_m^2 H - 3H_m H^2 + H^3)/(12J_c^2 ab) \qquad (-H_m < H < H_m) \,. \tag{76}$$

The reverse curve for the high-H_m $(H_p < H_m)$ case can be derived from Eqs. (45) and (51) as

$$M(H) = -J_c a(\tfrac{1}{2} - a/6b) + H_m - H - [(H_m - H)^2/4J_c](1/a + 1/b) + (H_m - H)^3/(12J_c^2 ab) \quad (H_m - 2H_p < H < H_m) , \tag{77a}$$

$$M(H) = J_c a(\tfrac{1}{2} - a/6b) \quad (-H_m < H < H_m - 2H_p) . \tag{77b}$$

B. Reduction to simple geometries

For the infinite slab, $b/a \to \infty$, the above equations for $M(H)$ become, for the initial curve,

$$M(H) = -H + H^2/2J_c a \quad (0 < H < H_p) , \tag{78a}$$

$$M(H) = -J_c a/2 \quad (H_p < H) ; \tag{78b}$$

for the low-H_m ($H_m < H_p$) curve,

$$M(H) = -H + (H_m^2 + 2HH_m - H^2)/4J_c a \quad (-H_m < H < H_m) ; \tag{79}$$

and for the high-H_m ($H_p < H_m$) curve,

$$M(H) = -J_c a/2 + H_m - H - (H_m - H)^2/4J_c a \quad (H_m - 2H_p < H < H_m) , \tag{80a}$$

$$M(H) = J_c a/2 \quad (-H_m < H < H_m - 2H_p) . \tag{80b}$$

For the cylinder, $b/a = 1$, the corresponding equations are, for the initial cruve,

$$M(H) = -H + H^2/J_c a - H^3/3(J_c a)^2 \quad (0 < H < H_p) , \tag{81a}$$

$$M(H) = -J_c a/3 \quad (H_p < H) ; \tag{81b}$$

for the low-H_m ($H_m < H_p$) curve,

$$M(H) = -H + (H_m^2 + 2HH_m - H^2)/2J_c a - (3H_m^3 + 3H_m^2 H - 3H_m H^2 + H^3)/12(J_c a)^2 \quad (-H_m < H < H_m) ; \tag{82}$$

and for the high-H_m ($H_p < H_m$) curve,

$$M(H) = -J_c a/3 + H_m - H - (H_m - H)^2/2J_c a + (H_m - H)^3/12(J_c a)^2 \quad (H_m - 2H_p < H < H_m) , \tag{83a}$$

$$M(H) = J_c a/3 \quad (-H_m < H < H_m - 2H_p) . \tag{83b}$$

Equations (78a), (78b), (79), (81a), (81b), and (82) for slabs and cylinders are the same as Eqs. (2), (3), and (5) in Ref. 2. Bean did not treat the high-H_m case, only the initial curves and the low-H_m case.

C. Hysteresis loss

Although this paper deals with magnetization curves rather than hysteresis loss W, it is straightforward to calculate energy loss per unit volume per field cycle for orthorhombic samples in the Bean limit. Generally,

$$W = \mu_0 \oint H\, dM \approx \mu_0 \oint M\, dH . \tag{84a}$$

For the complete low-H_m loop, from Eq. (76),

$$W = 2\mu_0 H_m^3 [J_c(a + b) - H_m]/(3J_c^2 ab) . \tag{84b}$$

For the complete high-H_m loop, from Eqs. (77a) and (77b),

$$W = 2\mu_0 J_c a[J_c a(a - 2b) + H_m(3b - a)]/3b . \tag{84c}$$

VI. DETERMINATION OF $J_c(H)$ FROM THE WIDTH OF THE HYSTERESIS LOOP

In this section we discuss two topics. First, we examine the necessary conditions for using Bean's model to determine J_c from hysteresis loop measurements assuming that $J_c(H_i)$ actually follows Eq. (1). Second, we offer a modification of the conventional cylinder and slab formulas for J_c determination for the general orthorhombic Bean model.

A. Prerequisites for Bean formulation

The traditional way to determine critical-current density of superconductors from magnetic measurements is based on Bean's model, where J_c is considered constant. To determine $J_c(H)$, a hysteresis loop is obtained, and the width of the hysteresis loop at a given field, $\Delta M(H)$, is measured. Bean's model[2] gives

$$J_c(H) = 3\Delta M(H)/2a \tag{85a}$$

for cylinders of radius a, and

$$J_c(H) = \Delta M(H)/a \tag{85b}$$

for slabs of thickness $2a$. Note that a field-dependent J_c is contrary to the assumption used to derive the Bean equations.

There are two requirements for using Eqs. (85a) and (85b) for J_c determination if $J_c(H_i)$ is assumed to actually follow Kim's model. (1) The magnetization on ascending and descending branches of the hysteresis loop at a given H must correspond to fully penetrated states. (2) The maximum deviation of $J_c(H_i)$ in the sample from $J_c(H_i = H)$ must be small. H is the uniform applied field, and H_i is the local internal field. The notation $J_c(H_i = H)$ means $J_c(H_i)$ for $H_i = H$ These conditions will be expressed in terms of recommended values of H_m, H, and p.

1. Fully penetrated states

For fully penetrated states, shielding currents circulate in only one sense throughout the volume of the specimen for the upper branch of the hysteresis loop and in the opposite sense for the lower branch. The condition of full penetration for both branches of the hysteresis loop is satisfied for the high-H_m case (Sec. III D) when

$$H_m \geqslant H_m^* \tag{86}$$

and

$$H \leqslant H_{prh} . \tag{87}$$

If $H_m = H_m^*$, then $H_{prh} = 0$, and the condition is satisfied only for $H = 0$. To obtain a useful H interval, Eq. (86) is restricted to

$$H_m \gg H_m^* . \tag{86a}$$

As examples, we obtain $J(H)$, using Eq. (85a), from the major hysteresis loops in Figs. 6(a)–6(e) (for which $H_m \gg H_m^*$). The symbols in Figs. 8(a)–8(e) give the $J_c(H)$

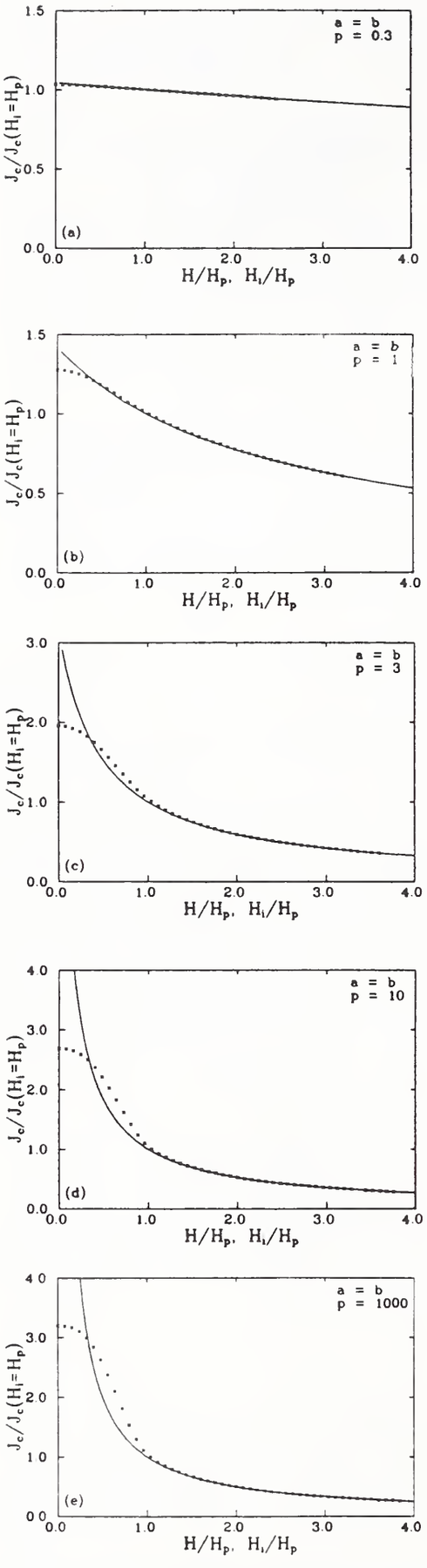

FIG. 8. Comparison of $J_c(H)$ [symbols, obtained from the major loops in Figs. 6(a)–6(e) using Eq. (85a)] with $J_c(H_i)$ [smooth curve, obtained from Eq. (1) which was also used to compute the loops in Fig. 6]. H and H_i are normalized to H_p. $J_c(H)$ and $J_c(H_i)$ are normalized to $J_c(H_i = H_p)$.

thus obtained for $p = 0.3$, 1, 3, 10, and 1000. For comparison, the smooth curves in Figs. 8(a)–8(e) give $J_c(H_i)$ derived from Eq. (1). The H scales are normalized to H_p, and the J_c scales are normalized to $J_c(H_i = H_p)$. We can see from these figures that $J_c(H)$ and $J_c(H_i)$ overlap in a certain H interval, somewhat different for each case. The upper limit of this correspondence interval is H_{prh}, Eq. (47), even for hysteresis loops where $H_m \gg 4H_p$.

2. Uniform $J_c(H_i)$

Referring again to Figs. 8(a)–8(e), the lower limit of overlap is about $1.5\,H_p$ for most cases. For the case $p \ll 1$, Fig. 8(a), this limit is much smaller. The reason for the extended overlap range is that $J_c(H_i)$ is rather uniform for small p, so that $J_c(H) \approx J_c(H_i = H)$.

We consider stages II and IV of the hysteresis loop (Sec. III D). From Eqs. (51) and (59a), we obtain $\Delta M(H)$. Dropping the higher-order terms and substituting into Eqs. (85a) and (85b), we obtain

$$J_c(H) = J_c(H_i = H)\{1 + s[\delta H_i(H)]^2\}\,, \tag{88}$$

where

$$\delta H_i(H) = \Delta H_i(H)/(H_0 + H)\,, \tag{88a}$$

$$\Delta H_i(H) = aJ_c(H_i = H)\,, \tag{88b}$$

and where $s = 1/4$ for $b/a \to \infty$ (infinite slab), and $s = 1/20$ for $b/a = 1$ (cylinder).

The field change relative to $(H_0 + H)$ in the sample is given by Eq. (88a). $\Delta H_i(H)$ defined by Eq. (88b) is the first-order difference between $H_i(0)$ and $H_i(a)$. From Eq. (88), $J_c(H)$ derived from $\Delta M(H)$ is always greater than $J_c(H_i = H)$. The difference between $J_c(H)$ and $J_c(H_i = H)$ is determined by $\delta H_i(H)$, decreasing with decreasing a and $J_c(H_i)$ and increasing H_0 and H. From the factor s, the error in $J_c(H)$ is much smaller for a cylinder than for a slab with the same a.

When $H \approx 0$, we have to consider stages II and III of the loop. The requirements for small errors are the same as for larger H except that $J_c(H)$ is always less than $J_c(H_i = H)$. When $p \ll 1$, H_0 is very large, and the error in $J_c(H)$ is very small, even at $H = 0$.

B. Formula for orthorhombic samples

$\Delta M(H)$ in Eqs. (85a) and (85b) is the vertical width of the hysteresis loop. In Sec. IV, we showed that the vertical width of the hysteresis loop increases with increasing b/a. If we use Eq. (85b) to calculate $J(H)$ for the samples with the same a but different b, different J_c will be obtained even for the same superconductor material. Thus, we derive a formula for orthorhombic samples using Bean's model. In the penetrated state, using Eq. (18b) with $x_0 = 0$ and $J(x) = -J_c$, we obtain

$$M_i(x) = -J_c(a - x)\,. \tag{89}$$

Substituting Eq. (89) into Eq. (7), or simply subtracting Eqs. (77b) and (75b), we have

$$\Delta M = J_c a(1 - a/3b)\,. \tag{90}$$

Rearranging, we obtain the general formula

$$J_c(H) = \Delta M(H)/[a(1 - a/3b)] . \quad (91)$$

It reduces to Eq. (85a) when $b/a = 1$, and Eq. (85b) when $b/a \to \infty$. Equation (85a) applies to polygons as well as cylinders, following the argument of Sec. II B. Equation (91) has also been derived by Clem.[16]

VII. CONCLUSION

Since the original work of Bean and London, the critical-state model has been used by many researchers to describe the magnetic response of hard type-II superconductors. The model has provided a simple, intuitive framework in which data could be analyzed, despite the need for approximations when applying the model to samples of finite dimensions. The refinements by Kim *et al.* were an effort to incorporate the field dependence of critical-current density. The results were magnetization curves that more closely resembled experimental data, particularly at low fields. Several other authors have attempted, with some success, to extend the critical-state model for various applications.

In this paper we have developed some useful equations for the analysis of magnetization of type-II superconductors within the construct of the critical-state theory. Using Kim's model for critical-current density, Eq. (1), we have analytically derived magnetization equations for the general case of an infinite superconductor with rectangular cross section. Different equations apply to the various parts of the magnetic hysteresis loop. Section III D gave the equations for the most useful case of large maximum applied field. Examples of the possible variety of magnetization curves were given in the figures. If we take different dimensional limits, the solutions apply to infinite slabs, cylinders, and rods with polygonal cross sections.

The general Kim solution can be reduced to a general Bean model for rectangular cross section by reducing the Kim equation for critical-current density (Sec. V A). In the appropriate dimensional limits, these equations become the well known Bean solutions for slabs and cylinders (Sec. V B). A simple formula was derived to relate the width of a measured hysteresis loop to the critical-current density as a function of applied field, for orthorhombic samples in the Bean limit (Sec. VI B).

ACKNOWLEDGMENTS

We thank J. Nogués for help with computer programming, W. L. Bahn for drawing Figs. 1–5, and J. S. Muñoz, R. Puzniak, V. Skumryev, and K. V. Rao for helpful discussions. We thank M. A. R. LeBlanc for valuable comments and making us aware of Ref. 11. MACSYMA, a symbolic manipulation program produced by Symbolics, Inc., was used to compare the cylinder and slab limits of our equations with the results in Refs. 5, 9, and 11, and to verify the continuity of the stages in Sec. III. This work was supported by the Swedish Board for Technical Development, STU, and the U.S. Department of Energy, Division of High Energy Physics.

[1] C. P. Bean, Phys. Rev. Lett. **8**, 250 (1962).
[2] C. P. Bean, Rev. Mod. Phys. **36**, 31 (1964).
[3] H. London, Phys. Lett. **6**, 162 (1963).
[4] Y. B. Kim, C. F. Hempstead, and A. R. Strnad, Phys. Rev. Lett. **9**, 306 (1962).
[5] Y. B. Kim, C. F. Hempstead, and A. R. Strnad, Phys. Rev. **129**, 528 (1963).
[6] J. H. P. Watson, J. Appl. Phys. **39**, 3406 (1968).
[7] F. Irie and K. Yamafuji, J. Phys. Soc. Jpn. **23**, 255 (1967).
[8] I. M. Green and P. Hlawiczka, Proc. IEE **114**, 1329 (1967).
[9] W. A. Fietz, M. R. Beasley, J. Silcox, and W. W. Webb, Phys. Rev. **136**, A335 (1964).
[10] V. R. Karasik, N. G. Vasil'ev, and V. G. Ershov, Sov. Phys. JETP **32**, 433 (1971) [Zh. Eksp. Teor. Fiz. **59**, 790 (1970)].
[11] J. A. Hulbert, Brit. J. Appl. Phys. **16**, 1657 (1965).
[12] M. C. Ohmer and J. P. Heinrich, J. Appl. Phys. **44**, 1804 (1973).
[13] J. J. Wollan and M. C. Ohmer, Cryogenics **16**, 271 (1976).
[14] G. Ravi Kumar and P. Chaddah, Phys. Rev. B **39**, 4704 (1989).
[15] A. M. Campbell and J. E. Evetts, Adv. Phys. **21**, 199 (1972).
[16] J. R. Clem, cited in: A. Umezawa, G. W. Crabtree, J. Z. Liu, H. W. Weber, W. K. Kwok, L. H. Nunez, T. J. Moran, C. H. Sowers, and H. Claus, Phys. Rev. B **36**, 7151 (1987).

☆ U.S. GOVERNMENT PRINTING OFFICE: 1991—576-422/45,153 REGION NO. 8

UNITS FOR MAGNETIC PROPERTIES

Quantity	Symbol	Gaussian & cgs emu [a]	Conversion factor, C [b]	SI & rationalized mks [c]
Magnetic flux density, magnetic induction	B	gauss (G) [d]	10^{-4}	tesla (T), Wb/m^2
Magnetic flux	Φ	maxwell (Mx), $G \cdot cm^2$	10^{-8}	weber (Wb), volt second (V·s)
Magnetic potential difference, magnetomotive force	U, F	gilbert (Gb)	$10/4\pi$	ampere (A)
Magnetic field strength, magnetizing force	H	oersted (Oe),[e] Gb/cm	$10^3/4\pi$	A/m [f]
(Volume) magnetization [g]	M	emu/cm^3 [h]	10^3	A/m
(Volume) magnetization	$4\pi M$	G	$10^3/4\pi$	A/m
Magnetic polarization, intensity of magnetization	J, I	emu/cm^3	$4\pi \times 10^{-4}$	T, Wb/m^2 [i]
(Mass) magnetization	σ, M	emu/g	1 $4\pi \times 10^{-7}$	$A \cdot m^2/kg$ Wb·m/kg
Magnetic moment	m	emu, erg/G	10^{-3}	$A \cdot m^2$, joule per tesla (J/T)
Magnetic dipole moment	j	emu, erg/G	$4\pi \times 10^{-10}$	Wb·m [i]
(Volume) susceptibility	χ, κ	dimensionless, emu/cm^3	4π $(4\pi)^2 \times 10^{-7}$	dimensionless henry per meter (H/m), Wb/(A·m)
(Mass) susceptibility	χ_ρ, κ_ρ	cm^3/g, emu/g	$4\pi \times 10^{-3}$ $(4\pi)^2 \times 10^{-10}$	m^3/kg $H \cdot m^2/kg$
(Molar) susceptibility	χ_{mol}, κ_{mol}	cm^3/mol, emu/mol	$4\pi \times 10^{-6}$ $(4\pi)^2 \times 10^{-13}$	m^3/mol $H \cdot m^2/mol$
Permeability	μ	dimensionless	$4\pi \times 10^{-7}$	H/m, Wb/(A·m)
Relative permeability [j]	μ_r	not defined		dimensionless
(Volume) energy density, energy product [k]	W	erg/cm^3	10^{-1}	J/m^3
Demagnetization factor	D, N	dimensionless	$1/4\pi$	dimensionless

a. Gaussian units and cgs emu are the same for magnetic properties. The defining relation is $B = H + 4\pi M$.

b. Multiply a number in Gaussian units by C to convert it to SI (e.g., $1\ G \times 10^{-4}\ T/G = 10^{-4}\ T$).

c. SI (*Système International d'Unités*) has been adopted by the National Bureau of Standards. Where two conversion factors are given, the upper one is recognized under, or consistent with, SI and is based on the definition $B = \mu_0(H + M)$, where $\mu_0 = 4\pi \times 10^{-7}$ H/m. The lower one is not recognized under SI and is based on the definition $B = \mu_0 H + J$, where the symbol I is often used in place of J.

d. 1 gauss $= 10^5$ gamma (γ).

e. Both oersted and gauss are expressed as $cm^{-1/2} \cdot g^{1/2} \cdot s^{-1}$ in terms of base units.

f. A/m was often expressed as "ampere-turn per meter" when used for magnetic field strength.

g. Magnetic moment per unit volume.

h. The designation "emu" is not a unit.

i. Recognized under SI, even though based on the definition $B = \mu_0 H + J$. See footnote *c*.

j. $\mu_r = \mu/\mu_0 = 1 + \chi$, all in SI. μ_r is equal to Gaussian μ.

k. $B \cdot H$ and $\mu_0 M \cdot H$ have SI units J/m^3; $M \cdot H$ and $B \cdot H/4\pi$ have Gaussian units erg/cm^3.

R. B. Goldfarb and F. R. Fickett, U.S. Department of Commerce, National Bureau of Standards, Boulder, Colorado 80303, March 1985
NBS Special Publication 696 For sale by the Superintendent of Documents, U.S. Government Printing Office, Washington, DC 20402

BL-114A
(5-90)

U.S. DEPARTMENT OF COMMERCE
NATIONAL INSTITUTE OF STANDARDS AND TECHNOLOGY

BIBLIOGRAPHIC DATA SHEET

1. PUBLICATION OR REPORT NUMBER
NISTIR 3975

2. PERFORMING ORGANIZATION REPORT NUMBER

3. PUBLICATION DATE
August 1991

4. TITLE AND SUBTITLE

Magnetic Measurements for High Energy Physics Applications

5. AUTHOR(S)

R. B. Goldfarb, Editor

6. PERFORMING ORGANIZATION (IF JOINT OR OTHER THAN NIST, SEE INSTRUCTIONS)

U.S. DEPARTMENT OF COMMERCE
NATIONAL INSTITUTE OF STANDARDS AND TECHNOLOGY
BOULDER, COLORADO 80303-3328

7. CONTRACT/GRANT NUMBER
DE-AI05-85-ER40240

8. TYPE OF REPORT AND PERIOD COVERED
Final Report, 6/15/88 – 6/14/91

9. SPONSORING ORGANIZATION NAME AND COMPLETE ADDRESS (STREET, CITY, STATE, ZIP)

U.S. Department of Energy
Division of High Energy Physics
Washington, DC 20545

10. SUPPLEMENTARY NOTES

11. ABSTRACT (A 200-WORD OR LESS FACTUAL SUMMARY OF MOST SIGNIFICANT INFORMATION. IF DOCUMENT INCLUDES A SIGNIFICANT BIBLIOGRAPHY OR LITERATURE SURVEY, MENTION IT HERE.)

This report is a collection of papers describing magnetic measurements on multifilamentary Nb-Ti superconductor wires and cables as a function of magnetic field and time at liquid-helium temperatures. The papers deal with ac losses and interfilament coupling by proximity effect and eddy currents. Flux creep was investigated under different experimental conditions. A Hall-probe magnetometer, which was used to measure magnetization and flux creep in the presence of a transport current, is described. A method for increasing the critical current of superconducting cable by controlling twist pitch is demonstrated. A critical-state model for the magnetization of superconductors was developed for samples with field-dependent critical current density and rectangular cross section.

12. KEY WORDS (6 TO 12 ENTRIES; ALPHABETICAL ORDER; CAPITALIZE ONLY PROPER NAMES; AND SEPARATE KEY WORDS BY SEMICOLONS)

ac losses; critical current; critical state; eddy currents; flux creep; Hall sensors; hysteresis; magnetization; magnetometry; multipole fields; niobium-titanium; proximity effect; Superconducting Super Collider; superconductors.

13. AVAILABILITY

X	UNLIMITED
	FOR OFFICIAL DISTRIBUTION. DO NOT RELEASE TO NATIONAL TECHNICAL INFORMATION SERVICE (NTIS).
	ORDER FROM SUPERINTENDENT OF DOCUMENTS, U.S. GOVERNMENT PRINTING OFFICE, WASHINGTON, DC 20402.
X	ORDER FROM NATIONAL TECHNICAL INFORMATION SERVICE (NTIS), SPRINGFIELD, VA 22161.

14. NUMBER OF PRINTED PAGES
72

15. PRICE

ELECTRONIC FORM